Université du Québec
Institut national de la recherche scientifique
Centre Énergie Matériaux Télécommunications

A V-Band High Gain Antenna System Integrated with a Six-Port Receiver for Backhaul Applications

Par

Elham Erfani

Thèse présentée pour l'obtention du grade de
Philosophiae doctor (Ph.D.)
en Télécommunications

Jury d'évaluation

Président du jury et examinateur interne:	Tarek Djerafi INRS-EMT
Examinateur externe	Abdel Razik Sebak Université Concordia
Examinateur exnterne	Chan-Wang Park Université du Québec à Rimouski
Directeur de recherche	Serioja Tatu INRS-EMT

dedicace

To my dear father and mother

To my dear spouse Mahmoud and our lovely daughter Nika

Remerciements

Tout d'abord, je voudrais exprimer toute ma gratitude à mon superviseur, Prof. Serioja Ovidiu Tatu, qui m'a donné la chance de joindre son équipe de l'INRS. Il a eu confiance en moi et m'a permis de choisir le thème de recherche et d'étendre mes connaissances en passant plus d'une année dans l'Université de Waterloo. Je lui serai toujours reconnaissante pour son soutien, non seulement pour ses sages conseils, mais aussi pour le fait de considérer son équipe comme sa famille.

Mes remerciements les plus sincères vont aux membres du jury de thèse, pour le temps passé à lire cette thèse et pour leurs remarques et leurs suggestions pertinentes.

Je voudrais aussi remercier à mes collègues du Centre Matériaux Télécommunications (EMT) pour leur aide généreuse, surtout à Dr. Emilia Moldovan.

Mais, en tout premier lieu, ma sincère gratitude à ma famille, pour son encouragement et son soutien permanent pendant ma vie. Je suis profondément reconnaissante à mon père et à ma mère, pour tout leur soutien inoubliable pendant toute ma carrière. Mes sincères remerciements à mes chères sœurs.

Enfin, mais non le moindre, je voudrais remercier mon cher époux, Dr. Mahmoud Niroo-Jazi, pour ses conseils techniques et pour son soutien. Sans son aide, je n'aurais pu faire face aux difficultés liées à mes études doctorales et à l'éloignement de ma famille.

Résumé

La prolifération récente des services de données et la demande exponentiellement croissante pour le transfert de données mobiles ont conduit à l'émergence de la 5^{th} génération (5G) de réseaux cellulaires, destinée à traiter la multitude de problèmes liés au débit et de données élevées et à sa capacité. Grâce au grand nombre de fréquences inutilisées disponibles dans le spectre de fréquences d'ondes millimétriques (mm-wave), cette bande a été considérée comme un candidat prometteur pour les futures communications mobiles 5G. Cependant, la propagation radio à ces fréquences fait l'objet de pertes élevées, dues à l'absorption atmosphérique, à la pluie et au feuillage. Par conséquent, pour compenser la perte de propagation et le blocage de la liaison, l'utilisation d'une antenne hautement directionnelle à large bande, à faisceau balayé, s'avère nécessaire.

Dans cette thèse, on présente un nouveau récepteur frontal à ondes millimétriques, composé d'un système d'antennes à gain élevé, intégrant un récepteur six-port bon marché, pour les réseaux d'amenée en ondes millimétriques. Comme principale contribution de ce travail, on fait un examen minutieux de l'application des matériaux artificiels émergents dans la conception d'un nouveau système d'antennes dénommées antennes à réseau d'émission (TA) ou à lentille planaire (PDL), afin de focaliser de manière efficace les signaux RF reçus/émis dans la/les direction(s) désirée(s); on propose une structure appropriée pour les applications en ondes millimétriques et on fait une étude analytique et expérimentale sur les performances de l'antenne. Dans cette perspective, tout d'abord, on étudie et on développe une antenne TA basée sur des métamatériaux à un indice de réfraction à gradient (GRIN), afin d'analyser sa faisabilité pour les applications en ondes millimétriques, avec les moyens de fabrication disponibles. On conclut que, en raison des exigences liées aux tolérances de fabrication, pour la construction d'une antenne TA, on devrait alternativement utiliser des matériaux de surface sélective en fréquence (FSS). Pour répondre aux exigences de l'antenne TA, on a conçu une cellule unitaire FSS insensible à la polarisation qui assure une réponse en phase de transmission linéaire, ayant une plage de variation de 270 ° et une perte d'insertion inférieure à -3 *dB*, sur une bande de fréquence désirée de 58 *GHz* à 64 *dB*. En outre, pour activer l'antenne TA proposée, on présente un nouveau module de réseaux d'antennes planaires « patch » 2×4 avec de connexions à ouverture couplée intercalées avec une structure à surface souple. La structure à surface souple est utilisée pour améliorer les performances du réseau en termes d'efficacité (gain), de largeur de bande et du niveau des lobes latéraux. Cette lentille discrète montre un gain maximal de 30.92 *dB* avec une efficacité d'ouverture de 38.4.

Comme convertisseur abaisseur de fréquence direct, l'on a conçu un circuit six-port composé de quelques éléments passifs et l'on en a fait une caractérisation complète, afin d'obtenir des ports d'entrée/de sortie adaptés, une isolation inférieure à -20 *dB*, et une bonne réponse en amplitude de transmission et en phase, sur toute la largeur de bande désirée. En outre, afin de récupérer les données de bande de base, on propose un détecteur de puissance équilibré, ayant une grande largeur de bande, de plus de 10 *GHz*. Par l'utilisation de la technologie d'interconnexion avec câblage

filaire (bonding wire), l'antenne fabriquée avec la technologie PCB est intégrée à l'amplificateur à faible bruit (LNA) et au récepteur à six-ports développé avec la technologie MHMIC. L'architecture du récepteur frontal intégré est testée pour différents types de constellations et de distances entre le récepteur et l'émetteur. Les résultats obtenus ont montré qu'on peut considérer la configuration proposée comme une solution innovatrice pour les communications sans fil par ondes millimétriques.

Abstract

Recently, the data service proliferation and explosively increased needs on mobile data traffic have emerged the 5^{th} generation (5G) of cellular networks that are expected to address the plethora of high data rate and capacity. Because of the abundant amount of unused frequencies available in millimeter-wave (mm-wave) frequency regime, this band has been considered as a prominent candidate for future 5G mobile communication. However, radio propagation at these frequencies suffer from high losses due to atmospheric absorption, rain, and foliage. Therefore, the use of a wideband high directive antenna with beam scanning is necessary to overcome the propagation loss and link blockage.

In this thesis, a new millimeter wave (mm-wave) front-end receiver composed of a high gain antenna system integrated with a low-cost six-port receiver is demonstrated for mm-wave backhaul networks. As the main contribution of this work, the application of emerging artificial materials in designing a new antenna system, so-called transmit-array (TA) or planar discrete lens (PDL)antennas to effectively focus the received/transmit RF-signals in the desired direction(s) is thoroughly investigated, the appropriate structure for mm-wave applications is proposed, and the antenna performances are analytically and experimentally studied. In this perspective, a TA based on gradient-refractive-index metamaterials (GRIN) is firstly studied and developed to investigate their feasibility for mm-wave applications based on the available fabrication facilities. It is concluded that because of fabrication tolerance requirements, frequency selective surface (FSS) materials should alternatively be used to construct a TA. To meet the requirements of the TA antenna, a polarization-insensitive FSS unit-cell offering a linear transmission phase response with a variation range of 270° and insertion loss less than -3 dB over a desired bandwidth of 58-64 GHz is designed. Furthermore, to excite the proposed TA, a new planar array module composed of 2×4 aperture-coupled-patches interleaved with a soft-surface structure is presented. Soft-surface structure is used to improve the array performances in terms of efficiency (gain), bandwidth, and side-lobe level. This discrete lens shows a peak gain of 30.92 dB with 38.4 aperture efficiency.

As a direct down-convertor, a six-port circuit composed of some passive elements is designed and fully characterized to obtain matched input/output ports, isolation less than -20 dB, and a good transmission amplitude and phase responses over the desired bandwidth. In addition, to recover the baseband data, a balanced power detector with a reflection coefficient bandwidth of more than 10 GHz is proposed. By applying the bonding wire interconnection technology, the antenna fabricated with PCB technology is integrated with LNA and six-port receiver built in MHMIC technology. The integrated front-end receiver architecture is tested for different types of constellation and various distances between receiver and transmitter. Achieved results demonstrated that the proposed configuration can be considered as an innovative solution for long-distance millimeter-waves wireless communications.

Table des matières

Liste des figures

Liste des tableaux

Liste Des Abbréviations

ACP	Aperture Coupled Patch
ACPA	Aperture Coupled Patch Antennas
ADS	Advanced Design System
AIP	Antenna In Package
AM	Antenna Module
AMC	Artificial Magnetic Conductor
AOC	Antenna On Chip
AP	Antenna Package
APs	Access Points
ATSA	Antipodal Exponential Taper Slot Antenna
BER	Bit Error Rate
BGA	Ball Grid Array
BPF	Band Pass Filters
BSs	Base Stations
CST	Computer Simulation Technology
DC	Direct Current
DRA	Dielectric Resonator Antenna
DSP	Digital Signal Processor
EACPA	Eared Aperture Coupled Patch Antenna
EBG	Electromagnetic bandgape
EC	Equivalent Circuit
FSS	Frequency Selective Surface
FW	Full Wave
GCPW	Grounded Coplanar Waveguide

GRIN	Gradient Refractive Index
HDRA	Hybrid Dielectric Resonator Antenna
HFSS	High Frequency Structure Simulator
HIS	High Impedance Surfaces
HMFE	Half Maxwell Fish Eye
IEEE	the Institute of Electrical and Electronics Engineers
IF	Intermediate Frequency
INRS	Institut National de la Recherche Scientifique
KCR	Koch-shaped Cut-wire Resonator
LGA	Land Grid Array
LIM	Low Index Metamaterial
LNA	Low Noise Amplifier
MBSs	Macro Base Stations
MIMO	Multiple Input Multiple Output
MHMIC	Miniature Hybrid Microwave Integrated Circuits
MMIC	Microwave Monolithic Integrated Circuit
MMW	Millimeter Wave
NF	Noise Figure
NIM	Negative Index Metamaterial
NLOS	Non Line of Sight
OFDM	Orthognal Frequency Division Multiplexing
PCB	Print Circuit Board
PDL	Planar Discrete Lens
QAM	Quadrature Amplitude Modulation
QPSK	Quadrature Phase-Shift Keying
RA	Reflectarray
RF	Radio Frequency
RR	Rectangular Ring
RX	Receiver
SA	Semi Analytically
SHC	Sample and Hold Circuit
SIW	Substrate Integrated Waveguide

SL	Strip Line
SLL	Side Lobe Level
SNR	Signal to Noise Ratio
TA	Transmitarray
TE	Transverse Electric
TM	Transverse Magnetic
TRL	Thru, Reflect, Line
TX	Transmitter
UC	Unit Cell
VCO	Voltage Control Oscillator
VNA	Vector Network Analyser
ZIM	Zero Index Metamaterial

Chapitre 0

Introduction

Jusqu'à présent, au niveau mondial, la quatrième génération (4G) des systèmes de communication cellulaire a été adoptée et fortement utilisée, dès la première génération, couvrant les systèmes analogiques de base conçus pour la communication vocale, jusqu'à la quatrième génération (4G), soutenant les applications vidéo à faible latence et les applications multimédia de haute qualité. L'augmentation exponentielle du trafic de données mobiles, entraînée par le flux vidéo et l'utilisation massive des téléphones intelligents et des tablettes, pose des défis sans précédent pour les fournisseurs de services sans fil en raison d'un manque de capacités dû au spectre limité de fréquences disponibles en dessous de 6 GHz [1]. La densification des réseaux, les techniques avancées d'efficacité spectrale, telles que le multiplexage par répartition orthogonale en fréquence (OFDM), et l'extension de la bande de fréquence (jusqu'à 100 MHz) par l'agrégation des porteuses afin de combiner de différents éléments porteurs, sont quelques méthodes essentielles de répondre aux exigences liées à la capacité des réseaux mobiles 4G actuels [1]-[4]. Même si la mise en œuvre conjointe de ce mécanisme peut théoriquement donner des débits de données supérieurs à 1 Giga-bit-par-seconde (Gb/s) pour les utilisateurs stationnaires, l'adoption d'une bande plus large est essentielle pour assurer des débits des plusieurs Gb/s pour tous les utilisateurs de la zone de couverture. En conséquence, les fournisseurs de services doivent être prêts à soutenir le volume important de données jusqu'en 2020, en cherchant une capacité plus grande, par l'utilisation d'un nouveau spectre sans fil, au-delà des standards 4G actuels.

Il a été prouvé que la grande part du spectre insuffisamment utilisé, dans la gamme 30-300 GHz, désigné par les ondes millimétriques (ondes mm), est adéquate pour répondre aux défis posés par

les données mobiles, en fournissant un accès radio à large bande et un réseau d'amenée dans les futurs réseaux sans fil (5G) [2]-[10]. Dans cette grande largeur de bande de fréquence disponible, les travaux majeurs de recherche et expérimentaux visent ce que l'on appelle la bande Ka (27-40 GHz), la bande V (57-64 GHz), et la bande E (71-76 GHz et 81-86 GHz), en vue de prouver leur potentiel pour les applications 5G. A cause de leur taux d'absorption atmosphérique plus faible, il a été proposé d'utiliser les bandes Ka et E pour les communications extérieures à longue portée (plusieurs kilomètres), tandis que la bande V semble appropriée pour les communications sans fil à courte portée (intérieures) et à mi- portée (extérieures, jusqu'à 1 mille). La bande V, en particulier, offre plus d'avantages du fait qu'elle est sans licence, en offrant une plus grande sécurité des interférences (elle est adéquate pour les petites cellules) et en permettant une efficacité spectrale, par le schéma de réutilisation des fréquences. En outre, avec l'émergence du nouveau standard IEEE 802.11ay, qui offre une bande plus large (6 canaux), ainsi que des techniques d'agrégation de canaux, on s'attend, dans les années à venir, à une utilisation massive de cette bande pour le réseau d'amenée, pour l'accès sans fil à large bande, et pour les appareils électroniques grand public [10]-[12]. On estime que les systèmes 5G devraient offrir en pratique un débit uniforme de données de minimum 1 Gb/s partout, pour tous les utilisateurs et que les appareils fonctionnant dans cette largeur de bande sans licence pourront assurer un accès sans fil aux données élevé et un flux vidéo pour les communications à mi portée, respectivement, et à courte portée [13] et [14].

Dans cette perspective, quelques groupes majeurs de recherche et quelques des meilleurs four nisseurs de services, y compris Ericsson, Intel, Nokia, Samsung Electronics, et NEC Corporations ont présenté leurs recherches et leurs produits préliminaires [13]-[15]. Essentiellement, ils doivent faire face à deux problèmes liés à l'utilisation des communications intérieures/extérieures en ondes millimétriques; il s'agit de l'atténuation élevée de propagation et du blocage de la voie de communication, par des obstacles pour les utilisateurs mobiles. Il est bien connu que, pour une certaine taille d'ouverture, la directivité d'antenne augmente avec la fréquence. Alternativement, cela signifie que, avec des ondes de longueur d'onde plus courtes, l'on peut grouper plus d'éléments rayonnants dans un petit espace et l'on peut concevoir des antennes à gain élevé, à des fréquences en ondes millimétriques, pour compenser la perte de propagation d'un lien de communication sans fil [15] et [17]. Afin de résoudre le problème au niveau du blocage et d'atteindre un rapport signal-bruit (SNR) élevé, pour avoir des services de plus grande qualité, l'on utilise d'habitude des antennes multifaisceaux et à balayage électronique [18]-[20]. Vraiment, il a été démontré que, sans se préoc-

cuper de la grande absorption et de l'établissement des connections hors portée optique (NLOS), l'utilisation de la technologie des ondes millimétriques est la seule solution pour les futurs systèmes de communication à haut débit de données. Les principaux objectifs de cette recherche sont d'explorer les nouveaux concepts de systèmes efficaces d'antennes en ondes millimétriques à gain élevé et de développer un récepteur bon marché pour les applications pour petites cellules, qui peuvent faire face aux défis ci-dessus. Ce chapitre explique les principales motivations, applications, et les objectifs de cette recherche.

0.1 Pourquoi les ondes millimétriques sont-elles la solution

Le théorème de Shannon définit la limite supérieure du débit de données d'un canal de communications, réalisable sans erreur, connue comme la capacité du canal, C en bps. Cette capacité maximale du débit de données est liée à la bande de fréquence du canal, B, et au rapport signal-bruit, SNR, comme illustré par l'équation (1).

$$C = B \log_2(1 + SNR) \tag{1}$$

Dans cette équation, le rapport signal-bruit reçu est le rapport entre la puissance P_r du signal reçu et le bruit du récepteur P_n, et l'on exprime comme suit:

$$SNR = \frac{P_r}{P_n} = \frac{P_r}{KTBF} \tag{2}$$

où, K est la constante de Boltzmann ($1.38.10-^{23} J/K$) et T, la température ambiante absolue de 290K ($N_0 = KTF$ désigne la densité spectrale de puissance du bruit), et F est le facteur de bruit du système. Dans le cas des systèmes de communication radio, la largeur de bande est une fraction de la porteuse radiofréquence (RF) f_c, à savoir, $B = \alpha.f_c$, où α est généralement de moins de quelques pourcents. La couverture de ces systèmes est définie ou contrôlée par un rapport SNR minimal

exigé. Il ressort clairement de cette équation qu'une modalité d'augmenter le débit de données de communication est d'utiliser une bande plus large.

Des équations (1) et (2), l'on peut déduire intuitivement que si la puissance reçue est proportionnelle à la fréquence de la porteuse du signal RF, dans toute la zone de couverture, alors le rapport SNR du système devient constant. Cela indique que le débit de données réalisable C est une fonction linéaire de la fréquence de la porteuse f_c. Par conséquent, si $B = \alpha.f_c$, plus la fréquence est élevée, plus le débit de données réalisable est plus haut. C'est pour cela que le spectre des ondes millimétriques joue un rôle essentiel dans l'augmentation de la capacité de milliers fois, par rapport aux technologies actuelles [21].

0.2 Pourquoi les petites cellules sont-elles nécessaires

La distance de couverture d'un système radio est liée aux paramètres d'accès. L'équation de Friis décrit sa version simplifiée pour la propagation en espace libre sous un ciel clair, tel qu'indiqué par :

$$P_r = (\frac{c}{4Rf_c\pi})^2.G_t.G_r.P_t.\frac{1}{L} \tag{3}$$

Dans cette équation, le terme $(\frac{c}{4Rf_c\pi})^2$ désigne la perte de propagation en espace libre, P_t est la puissance transmise, L représente les pertes supplémentaires du système, G_t et G_r désignent les gains des antennes d'émission et, respectivement, de réception, R représente la distance entre l'émetteur et le récepteur, et c, la vitesse de la lumière. La couverture maximale d'un système de communication sans fil R_m peut être définie comme la distance pour le rapport SNR minimal requis pour détecter les signaux avec le taux d'erreur sur les bits (BER) désiré pour le schéma de modulation utilisé. En substituant l'équation (2) à l'équation (3), l'on calcule la couverture maximale par :

$$R_m^2 = (\frac{c}{4f_c\pi})^2.G_t.G_r.L.\frac{P_t}{P_r} = (\frac{c}{4f_c\pi})^2.\frac{G_t.G_r.P_t}{SNR.N_0.B.L} \tag{4}$$

L'équation (4) montre que la couverture est réduite par un taux de $R_m \sim f_c^{\frac{-3}{2}}$ pour les propagations LOS en espace libre, lorsque la fréquence est augmentée. Puisque le gain du réseau d'antennes planaires ou l'antenne à ouverture que l'on utilise dans l'émetteur est une fonction au carré de la fréquence, la relation entre la réduction de la couverture et la fréquence est décrite par $R_m \sim f_c^{\frac{-1}{2}}$ (on peut montrer que pour le réseau linéaire, la relation entre la gamme et la fréquence peut être exprimée par $R_m \sim f_c^{-1}$). Cela prouve que les antennes à gain élevé sont nécessaires pour les communications extérieures, afin d'atteindre une distance de communication plus grande et un meilleur débit de données.

Pour donner plus de précisions sur les exigences de gain, sur la couverture et sur la capacité maximale du canal, l'on fait ici une analyse de budget de liaison pour une connexion extérieure typique de 60 *GHz*. Dans cette étude, l'on utilise un modèle de canal développé à partir des campagnes de mesure, où la perte d'espace libre est décrite par l'équation (5), pour les canaux de propagation intérieure et extérieure, en visibilité directe (LOS) et sans visibilité directe (NLOS) [2], [12], [17], [21], and [22].

$$PL(\ dB) = 32.4 + 20\log_{10}(f_{GHz}) + 10n\log_{10}(R_m) \tag{5}$$

où, n représente l'exposant de la perte de propagation, qui, selon les mesures, pourrait s'approcher de 2 (perte d'espace libre) pour une transmission LOS ($n = 2.2$ est une valeur beaucoup plus conservatrice pour les applications en ondes millimétriques) ou jusqu'à $n = 4$ pour les scénarios à plusieurs trajets. Cette équation ne comprend pas d'autres facteurs de perte, tels que les atténuations dues aux conditions atmosphériques et aux précipitations et les pertes de polarisation. La réduction de la couverture devient grave lorsque l'analyse de budget de liaison inclue aussi d'autres facteurs de perte. On peut trouver une description détaillée de la modélisation des canaux et de la perte de propagation pour les liaisons à ondes millimétriques en [22]. En incluant l'équation (5) dans l'équation (4) et en la récrivant, le rapport SNR d'un système extérieur de communication en propagation LOS, sans effets d'ombrage et sans effets des précipitations, peut être exprimé par:

$$SNR(\,dB) = P_t + G_t + G_r - PL - L - 10\log_{10}(N_0 B) \tag{6}$$

Afin d'analyser ce problème, l'on fait une étude de cas pour une liaison typique à 60 GHz, ayant les paramètres décrits au Tableau 1. L'affaiblissement dû à la pluie pour les zones à faibles précipitations (8 mm/h) et à fortes précipitations (65 mm/h), ayant une disponibilité du signal de 99,99% sont 3,5 dB/Km, respectivement 21 dB/Km. L'affaiblissement par l'oxygène dépend de la distance et a été représenté par 16 dB/Km dans cette étude [23].

La figure 1 montre les capacités maximales réalisables, comme le montre l'équation (1) pour les zones à faibles et à fortes précipitations, lorsque les gains totaux de l'antenne (récepteur et émetteur) changent. Les graphiques montrent que la capacité du système est réduite, par l'augmentation de la distance. En outre, en étant l'une des principales sources de la perte de propagation, la pluie diminue fortement le débit de données maximum et réduit la portée de couverture. Cela indique qu'on a besoin d'antennes directives ayant des gains entre 25-35 dBi, pour avoir un débit de données d'un Gb/s sur des distances de couverture de 100-400 m. Par conséquent, pour les systèmes de communication en ondes millimétriques, il est nécessaire d'utiliser de petits réseaux cellulaires avec les antennes à gain élevé [2], [17], et [23]. Cette plage de gain est aussi conforme aux réglementations de la FCC sur la puissance émise maximale admissible. Selon la nouvelle règlementation, la puissance isotrope rayonnée efficace (EIRP) moyenne et de point pour les dispositifs à 60 GHz ayant des antennes situées à l'extérieur est de 82 dBm et de 85 dBm minus 2 dB pour chaque dB du gain de l'antenne en dessous de 51 dBi, [24], respectivement [25].

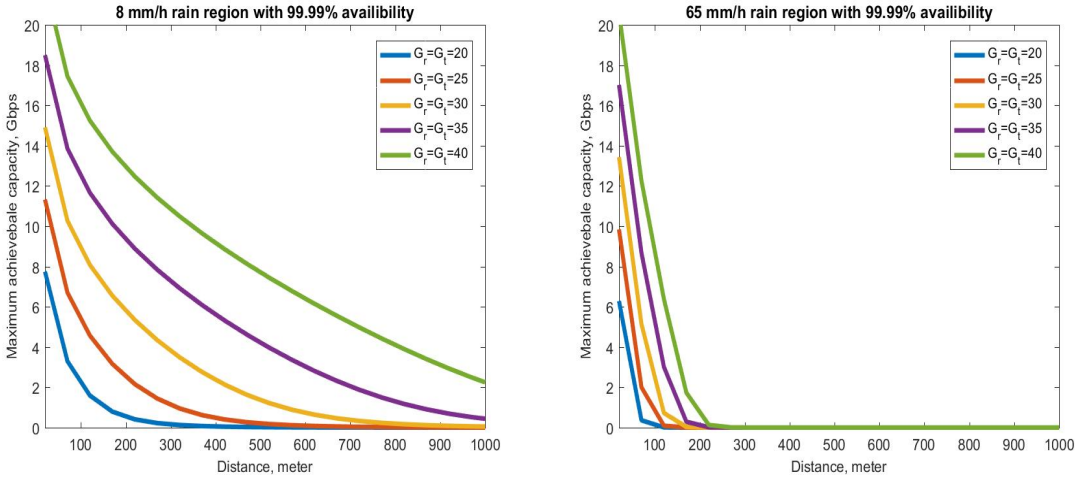

(a) Low rainfall zone (8 mm/h)

(b) High rainfall zone (65 mm/h)

Figure 1 – Débit de données maximal réalisable, selon le théorème de Shannon pour un lien ayant les paramètres définis au Tableau 1.

Tableau 1 – Paramètres utilisés dans l'analyse de liaison.

Paramètre	Valeur	La description
F_c(GHz)	60	Fréquence porteuse
B(GHz)	2.16	Bande passante du récepteur
Tx power(dBm)	10	Puissance de sortie de l'émetteur
G_t=G_r(dBi)	$10 \leq G \leq 40$	Gains du récepteur et de l'émetteur
L	20	Mise en place du système , pertes d'oxygène et de pluie
NF(dBm)	10	Bruit de système
R(m)	$0 \leq R \leq 1000$	Lien gamme
n	2.2	Perte de l'exposant

0.3 Pourquoi la formation de faisceaux et les faisceaux balayés sont-ils nécessaires?

En raison de la faible capacité de diffraction des ondes millimétriques, les communications à ces fréquences sont très sensibles au blocage par les obstacles. En fait, les liaisons dans les systèmes extérieurs sont établies par des diagrammes de rayonnement très ciblés, ce qui les rend une sorte de communication LOS. Ces liaisons peuvent être facilement compromises par tout désalignement causé par le balayage de l'antenne par le vent ou par le blocage par des objets volants. Cela est contraire aux technologies micro-ondes actuelles, qui bénéficient des avantages des grosses diffractions des environnements, comme un mécanisme de propagation dominant [18]-[20], et [22]. Par conséquent, pour les communications en ondes millimétriques, il est nécessaire d'utiliser d'antennes ayant des capacités de balayage électrique ou mécanique à faisceaux, qui peuvent ajuster les directions de leurs diagrammes de rayonnement.

0.4 Scénario de cellules 5G à ondes millimétriques, à radios multiples

Pour répondre à la demande croissante envisagée pour les services efficaces à haut débit de données destinés aux utilisateurs finals, pour la future génération de systèmes 5G de communication mobile et sans fil, on a proposé des architectures de réseaux multi-niveaux [26]. En utilisant les technologies les plus avancées pour ces réseaux, telles que les systèmes à entrées multiples / sorties multiples (MIMO), les communications à haute efficacité énergétique, les réseaux de radiocommunication cognitifs, et la communication par lumière visible, les réseaux cellulaires peuvent offrir aux utilisateurs des expériences de plusieurs gigabits par seconde [27]-[29]. Le schéma d'un réseau 5G typique à multi-niveaux est présenté à la Figure 2. Il comprend des macro cellules à longue et à moyenne portée, fonctionnant dans la sous-bande de 3 GHz (700 MHz à 2.7 GHz), de petites cellules (rayon de 10-50 m) utilisant la sous-bande de 6 GHz (2.45, 3.5, et 5.6 GHz), et de petites cellules à ondes millimétriques près de la station de base des ondes millimétriques. Dans le réseau hétérogène 5G proposé, l'ancienne technologie (2G/3G et LTE) peut garantir à l'utilisateur mobile la couverture de base à faible latence, la voix et le signal, tandis que les petites cellules à ondes millimétriques offrent aux utilisateurs une capacité maximale, si nécessaire [26] et [27].

.

Dans ce scénario de communication, les stations de base (BSs) et les systèmes de liaison à ondes millimétriques seront installés dans les zones urbaines, telles que les lampadaires, les façades des bâtiments et les tours. Chaque fois qu'un dispositif mobile requiert des échanges massifs de données, il est connecté à un réseau sous le couvert d'une petite cellule à ondes millimétriques. Macro-BSs (MBSs) aident les utilisateurs à trouver les petites cellules à ondes millimétriques et coopèrent avec les BSs à ondes millimétriques pour réaliser un transfert transparent. Afin de réaliser cette tâche, il faut tout d'abord activer l'émetteur-récepteur à ondes millimétriques du dispositif mobile pour informer les MBSs. Le réseau cellulaire micro-ondes gère le signal de commande et le trafic de service de priorité élevée, à haute qualité, tandis que les données agrégées sont portées par la section à ondes millimétriques du réseau. Dans ces petites cellules, les utilisateurs envisagés être à la proximité des points d'accès (APs) sont équipés d'antennes à faisceau de balayage, ayant un gain maximal entre 10 et 20 dBi, tandis que les liaisons terrestres devraient avoir plusieurs diagrammes directionnels.

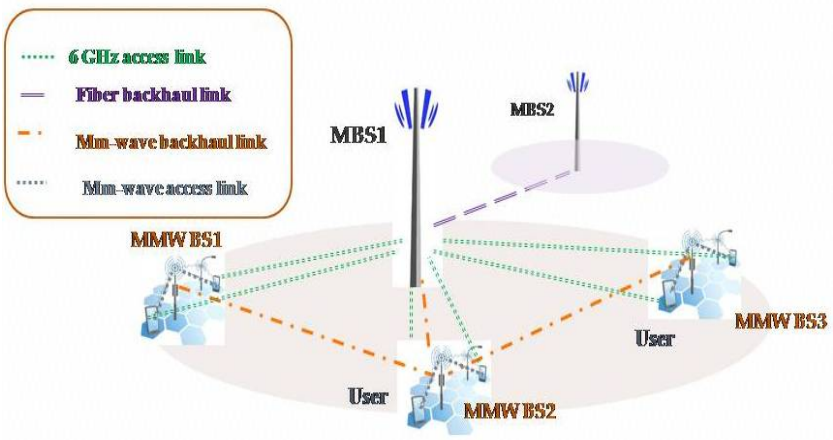

Figure 2 – Configuration d'un scénario typique de petit accès à ondes millimétriques et de réseau d'amenée.

0.5 Objectifs

Tel que discuté dans les sections antérieures, pour assurer assez de puissance rayonnée dans la direction désirée, il est nécessaire d'avoir une unité frontale (front-end) adéquate et, éventuellement, d'ajuster la direction du rayonnement pour résoudre le blocage et/ou le désalignement de la liaison radio causé par les oscillations du vent dans le réseau à petites cellules. Ces affirmations sont aussi

valables pour le récepteur de l'autre côté de la liaison. Une version simplifiée de l'unité frontale dans le mode réception est schématisée à la Figure 3. Cette unité comprend un système d'antenne à focalisation, son réseau d'alimentation et un circuit RF qui transforme les signaux reçus en une bande FI. Cette étude présente les examens effectués pour construire chaque bloc présenté à la Figure 3 et pour les intégrer ensemble afin de faire preuve d'un nouveau récepteur avec contrôle de faisceaux d'antennes pour les réseaux cellulaires en ondes millimétriques.

Cette étude vise essentiellement la section du système innovateur d'antennes proposé, qui traite les problèmes identifiés de ces réseaux de communication. Les principaux défis de cette thèse sont l'analyse des approches possibles pour la réalisation pratique de cette partie, l'architecture d'alimentation/pour la formation de faisceaux appropriée pour générer les diagrammes de gain élevé nécessaires et le moyen d'intégrer le réseau d'alimentation dans les circuits actifs/passifs à ondes millimétriques. Comme des objectifs spécifiques, l'on propose un système d'antennes à large bande, ayant un gain d'au moins 30 dBi et une bande de fréquence de fonctionnement de 57-64 GHz, que l'on peut intégrer de manière facile dans la partie de circuit RF par une technologie d'interconnexion avec câblage filaire (bonding-wire). Le système d'antennes comprend une nouvelle structure spatiale, dénommée lentille planaire (PDL) ou antenne à réseau d'émission (TA). Elle comprend un réseau d'alimentation et une ouverture de focalisation. Le réseau d'alimentation peut être un élément rayonnant unique générant un faisceau fixe, hautement directif (applications point à point) ou un réseau d'éléments rayonnants en utilisant un réseau de commutation afin de générer un système d'antennes multifaisceaux commutables hautement directif [20], [30] et [31]. Dans le cas précèdent, le faisceau peut être aussi balayé de manière mécanique, lorsqu'on peut faire des ajustements de l'ordre de $\pm 30\,^{\circ}$ [32]. Cependant, la structure à faisceaux fixes est pratiquement démontrée dans cette étude comme la validation de concept. La section du circuit RF est mise en œuvre à l'aide d'un récepteur six-port bon marché, où l'on utilise quatre détecteurs de puissance a diodes comme des convertisseurs abaisseurs. Dans ce travail de recherche, on a choisi cette architecture de récepteur grâce à ses avantages, y compris le fait qu'il est simple et qu'il ne comprend que des composants passifs, ayant une faible consommation de courant continu et qu'il convient pour être intégré avec des composants discrets. Enfin, la performance d'une liaison de communication pour les différents systèmes de modulation a été mesurée en laboratoire et les résultats ont été présentés et discutés.

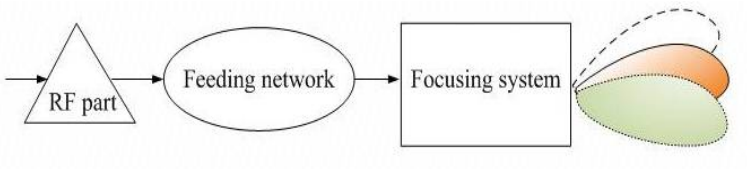

Figure 3 – Représentation schématique du frontal du récepteur à ondes millimétriques proposé.

0.6 Architectures de récepteurs

La tâche principale d'un récepteur RF est de séparer le signal reçu du bruit et d'autres signaux inutiles et d'extraire les informations désirées. Cela peut se réaliser principalement par le filtrage, l'amplification, ainsi que par la conversion de fréquence vers le bas. On peut réaliser le mélange du signal RF reçu avec l'oscillateur local dans différents types d'architectures. Dans la sous-section suivante, on examine quelques types de récepteurs, les plus communs.

0.6.1 Architecture du récepteur homodyne (Zéro-FI))

L'architecture du récepteur homodyne connu comme Zéro-FI est représentée à la Figure 4. La principale différence de ce type par rapport à d'autres architectures est que le signal RF reçu est transposé directement en bande de base par un processus de mélange à étape unique, dans lequel la fréquence angulaire du signal de l'oscillateur local est identique à celle de la porteuse RF du récepteur [33]. Par conséquent, il devient moins complexe et plus compact, en superposant le signal d'information sur son propre image. Malgré ses avantages, il pose de nombreux problèmes, y compris: 1) fuite de l'OL par le substrat vers l'antenne et l'amplificateur à faible brui (LNA); 2) tension d'offset DC : il est généré lorsqu'il y a une fuite de l'oscillateur local, amplifié et ensuite mélangé de nouveau (mélange automatique de l'oscillateur local), ce qui va provoquer des modifications des signaux et une saturation des circuits de la bande de base; 3) plus sensible à la non-linéarité uniforme du trajet RF. Malgré ces désavantages, ce type de récepteur est plus populaire, surtout dans les systèmes radio définis par logiciel, où le traitement de signal en bande résout ces problèmes [34].

0.6.2 Architecture du récepteur hétérodyne

La configuration schématique d'un récepteur hétérodyne est représentée à la Figure 5. La fréquence RF reçue est convertie à la baisse en une fréquence intermédiaire (FI) en deux étapes.

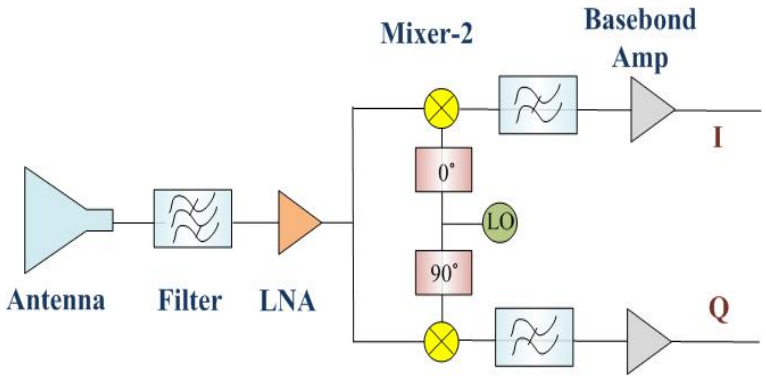

Figure 4 – Architecture d'un récepteur homodyne [34].

Premièrement, elle est mélangée par un OL avec une fréquence inégale, et ensuite elle est convertie à une fréquence FI. La deuxième étape est réalisée par un démodulateur IQ comprenant une paire de mélangeurs..

Le problème principal du récepteur hétérodyne est le rejet de la fréquence d'image. Afin de maximiser le rejet de la fréquence image, on devrait choisir une fréquence FI assez grande pour s'assurer que le signal d'image est loin du signal désiré, où il peut être éliminé de manière efficace par un filtre, entre le LNA et le mélangeur. Toutefois, l'augmentation de la fréquence FI requiert un facteur de qualité Q plus élevé dans le filtre FI. Par conséquent, ce type de récepteur fait l'objet d'un compromis entre le rejet de l'image et la sélection des canaux.

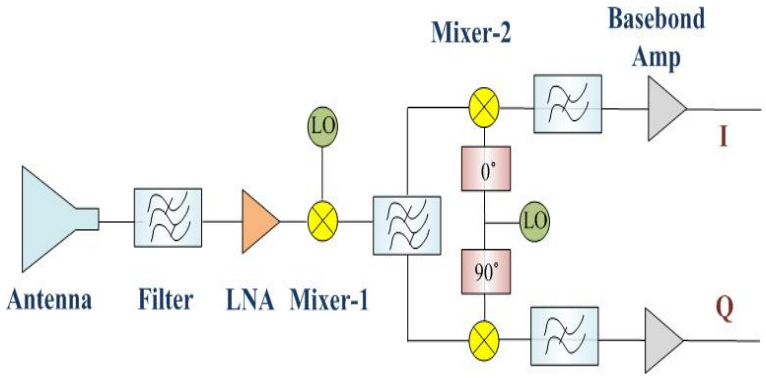

Figure 5 – Architecture d'un récepteur hétérodyne [34].

0.7 Architecture d'un récepteur à six ports

L'architecture d'un récepteur à six ports est représentée à la Figure 6. Il comprend une antenne, un amplificateur à faible bruit (LNA), un convertisseur abaisseur à six ports, des diodes de détection et le module bande de base. Dans cette perspective, la structure six-port est utilisée pour démoduler le signal reçu. Les signaux RF reçus par l'antenne d'alimentation sont amplifiés par un LNA et entrent dans le port d'entrée du convertisseur abaisseur six-port en quadrature. Le circuit six-port comprend trois coupleurs hybrides à 90 °et un diviseur de puissance de Wilkinson. Comme illustré à la Figure 6, ce circuit a deux entrées, le port de l'oscillateur local (OL) (a_5) et le port des signaux RF (a_6), et quatre sorties (b_1-b_4) connectées aux détecteurs de puissance adaptés.

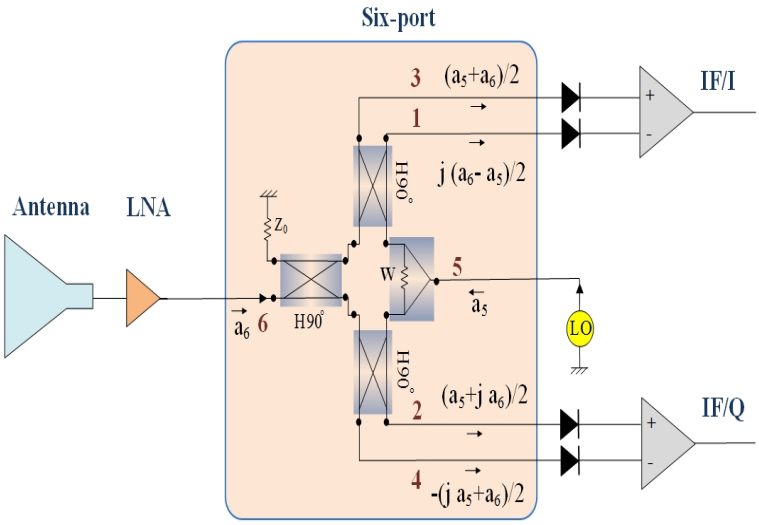

Figure 6 – Architecture d'un récepteur basé sur une structure six-port [36].

En tenant compte des paramètres S du coupleur hybride et du diviseur de puissance de Wilkinson, les signaux de sortie peuvent être exprimés par l'équation (7).

$$\begin{aligned} b_1 &= -j\frac{a_5}{2} + j\frac{a_6}{2} \\ b_2 &= \frac{a_5}{2} + j\frac{a_6}{2} \\ b_3 &= \frac{a_5}{2} + \frac{a_6}{2} \\ b_4 &= -j\frac{a_5}{2} - \frac{a_6}{2} \end{aligned} \tag{7}$$

Les signaux d'entrée d'une antenne et d'un oscillateur local peuvent être exprimés par l'équation (8).

$$\begin{aligned} a_5 &= \mid a_5 \mid exp(jw_5.t + \phi_5) \\ a_6 &= \mid a_6 \mid exp(jw_6.t + \phi_6) \end{aligned} \tag{8}$$

En supposant que les deux signaux d'entrée ont un coefficient d'amplitude de α ($\mid a_6 \mid = \alpha. \mid a_5 \mid = \alpha. \mid a \mid$), la différence de fréquence de Δw=(w_6-w_0), et la différence de phase de$\Delta\phi = (\phi_6 - \phi_5)$, alors, on a les signaux d'entrée suivants.

$$\begin{aligned} a_5 &= \mid a \mid exp(jw_0.t + \phi_5) \\ a_6 &= \alpha.a_5 exp(j\Delta w.t + \Delta\phi) \end{aligned} \tag{9}$$

En remplaçant l'équation (9) dans l'équation (7), les signaux de sortie sont

$$\begin{aligned} b_1(t) &= -j\frac{\mid a \mid}{2}.exp(jw_0.t + \phi_5).[1 + \alpha.exp(\Delta w.t + \Delta\phi(t) + \pi)] \\ b_2(t) &= \frac{\mid a \mid}{2}.exp(jw_0.t + \phi_5).[1 + \alpha.exp(\Delta w.t + \Delta\phi(t) + \pi/2)] \\ b_3(t) &= \frac{\mid a \mid}{2}.exp(jw_0.t + \phi_5).[1 + \alpha.exp(\Delta w.t + \Delta\phi(t))] \\ b_{4(t)} &= -j\frac{\mid a \mid}{2}.exp(jw_0.t + \phi_5).[1 + \alpha.exp(\Delta w.t + \Delta\phi(t) - \pi/2)] \end{aligned} \tag{10}$$

De l'équation (10), on peut conclure que les signaux de sortie de ce six-port sont des combinaisons linéaires de deux signaux d'entrée ayant de différents décalages de phase (0 °, 90 °, 180 °, et 270 °) comme illustré à la Figure 7.

Chacune des quatre sorties est injectée en un dispositif non-linéaire ayant une caractéristique quadratique de type équation (11).

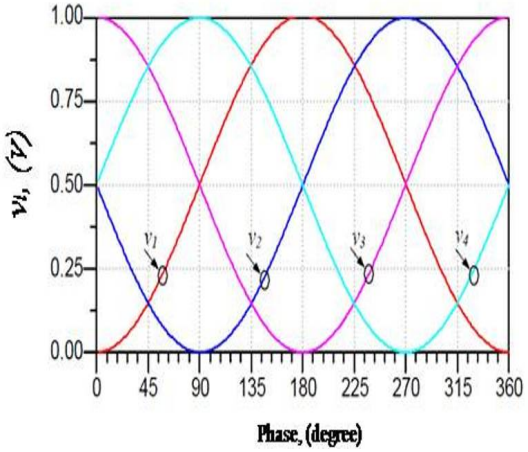

Figure 7 – Signal de sortie du six-port [36].

$$v_i = K_i.\mid b_i \mid^2, i = 1, ...4 \tag{11}$$

Si tous les détecteurs sont identiques avec $K_i = K$, la tension détectée se présente ainsi

$$\begin{aligned} v_{3,1}(t)] &= K\frac{\mid a \mid^2}{4}.[1 + a^2 \pm 2\alpha cos[\Delta wt + \Delta\phi(t)]] \\ v_{4,2}(t)] &= K\frac{\mid a \mid^2}{4}.[1 + a^2 \pm 2\alpha sin[\Delta wt + \Delta\phi(t)]] \end{aligned} \tag{12}$$

On peut obtenir les signaux I et Q par une soustraction adéquate des tensions de sortie détectées avec un amplificateur différentiel (avec A_{IF} gain) comme illustré à la équation (13).

$$\begin{aligned} v_{IF}^{I}(t) &= A_{IF}[v_3(t) - v_1(t)] = \alpha.K.a^2.A_{IF}.cos[\Delta wt + \Delta\phi(t)] \\ v_{IF}^{Q}(t) &= A_{IF}[v_4(t) - v_2(t)] = \alpha.K.a^2.A_{IF}.sin[\Delta wt + \Delta\phi(t)] \end{aligned} \tag{13}$$

Un filtre basse fréquence est appliqués afin d'atteindre les signaux de bande de base de l'équation (14).

$$\begin{aligned} I(t) &= \alpha.K.\frac{a^2}{2}.A_{IF}.A_{BB}.cos[\Delta\phi(t)] \\ Q(t) &= \alpha.K.\frac{a^2}{2}.A_{IF}.A_{BB}.sin[\Delta\phi(t)] \end{aligned} \tag{14}$$

Le signal démodulé des voies I et Q peut être représenté dans un diagramme de constellation, tel qu'exprimé par l'équation 15) [35].

$$\Gamma = I(t) + jQ(t) = \alpha.K.\frac{\mid a^2 \mid}{2}.A_{IF}.A_{BB}.exp[j\Delta\phi(t)] \tag{15}$$

Si la fréquence du signal RF et celle du signal OL sont identiques, le circuit fonctionne en un régime de conversion directe. Vraiment, le six-port fait la distinction entre la phase et l'amplitude [36].

Un circuit échantillonneur bloqueur (SHC) traite les signaux de sortie en bande de base amplifiés et une horloge synchronise les sorties en quadrature. Ces signaux sont ensuite utilisés comme entrées d'un module de traitement des signaux numériques (DSP).

Le diagramme de constellation pour la démodulation QPSK est représenté à la Figure 8, lorsque $\Gamma = B.exp[j\frac{\pi}{4}]$.

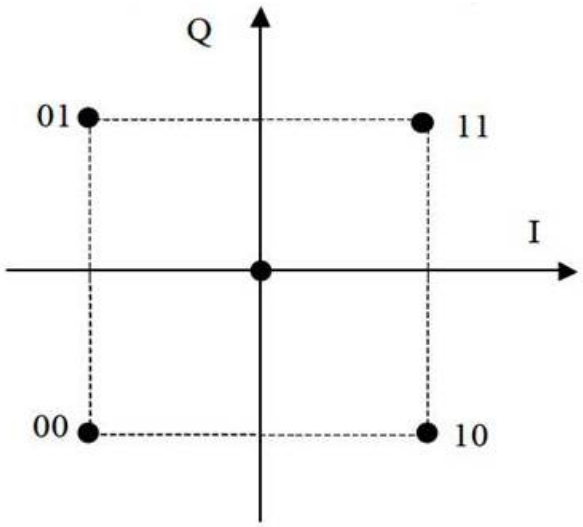

Figure 8 – Modulation QPSK [36].

Le récepteur à six-ports, grâce à ses caractéristiques intéressantes, telles que la grande largeur de bande, la diode de détection simple et bon marché, la faible consommation de puissance, et la simplicité de la mise en œuvre du circuit passif, suscite beaucoup d'attention pour les applications en ondes millimétriques. Toutefois, il a le désavantage d'un niveau de décalage en continu élevé, généré par des fuites indésirables et par les réflexions d'entrée. En outre, sa plage dynamique dépend surtout de la sensibilité de la diode de détection, qui est d'environ 40 dB, ce qui est beaucoup moins par rapport à d'autres types de récepteurs. En ce qui concerne le facteur de bruit (NF) du six-port passif, il est d'environ 7 dB, à cause de la perte, qui est un peu plus élevée par rapport à d'autres types.

0.8 Antennes à gain élevé

Pour faire face à la perte de propagation en ondes millimétriques et aux blocages auxquels se confrontent les liaisons terrestres à petites cellules de 60 GHz, l'utilisation d'une antenne à large bande et à gain élevé, ayant une capacité de balayer/commuter les faisceaux dans un secteur angulaire étroit, s'avère nécessaire. Les solutions actuelles, y compris le cornet [37], sont plutôt chères, encombrantes et lourdes, en fonction du gain requis. En outre, il n'est pas facile de diriger de manière mécanique ou électronique les diagrammes de rayonnement. L'utilisation d'un réseau d'éléments rayonnants planaires est une autre modalité de concevoir les antennes à gain élevé, surtout pour les applications à faisceaux fixes. Même si leur largeur de bande peut être améliorée en utilisant des substrats diélectriques à faible permittivité plus épais, elles ne sont pas efficaces à des fréquences d'ondes millimétriques en raison des pertes excessives de réseau [38]. En plus de ça, la réalisation des antennes planaires à large bande, à gain élevé et à faisceaux multiples (à savoir, un gain supérieur à 30 dBi) avec des réseaux passifs de formation de faisceaux tels que la matrice de Butler semble difficile en ondes millimétriques [20]. Comme méthode alternative, en [18] et [19], on a proposé, pour les réseaux cellulaires 5G, des antennes à balayage électronique de formation de faisceau hybride ayant des architectures de réseaux modulaires, afin d'obtenir des faisceaux directionnels dans la/les direction(s) désirée(s) et de soutenir de différents schémas multi-antenne, tels que les systèmes à entrées multiples/sorties multiples (MIMO) et la diversité. Dans cette perspective, pour cette bande large de fréquence de fonctionnement, il semble aussi possible de réaliser des antennes à balayage électronique et à large couverture angulaire, en utilisant une architecture en carrelage dans le but

d'obtenir un gain élevé [39]-[42]. Toutefois, cela augmente considérablement la complexité et le coût des systèmes d'antennes.

D'autres structures proposées, fonctionnant sur la base des principes à ondes de fuite [43] et des résonateurs de Fabry-Perot [44], sont intrinsèquement en bande étroite. Les techniques spatiales de formation de faisceaux, telles que les antennes à réflecteur et à lentilles diélectriques (DL) semblent être candidats pour la conception des antennes à large bande et à gain élevé [30] et [46]. On peut diriger de manière mécanique ou électronique leurs diagrammes de rayonnement, en utilisant un groupe de sources dans leurs plans focaux. Toutefois, ils sont lourds et vraiment désagréables, et leur mise en œuvre à 60 GHz nécessite une fabrication précise. Comme configurations planaires alternatives, les antennes à réseau de réflexion (RA) et à réseau d'émission (TA) (aussi dénommés lentilles diélectriques discrètes), avec leur grande efficacité et leurs hautes performances en large bande, sont des approches prometteuses pour les fréquences à ondes millimétriques [20] et [46]-[50]. Par rapport aux antennes RA alimentées au centre, les antennes TA ne font pas l'objet de blocages d'alimentation et sont moins sensibles aux défauts superficiels. En outre, elles peuvent répondre aux exigences liées aux faisceaux multiples, en utilisant un groupe de sources sans affecter les performances globales de rayonnement de l'antenne [48]. En plus, parmi les autres avantages des antennes TA par rapport aux antennes conventionnelles DL et de réflexion, on peut citer leur processus de fabrication relativement facile, leur poids léger et les possibilités de réaliser et d'amplifier les architectures.

Une configuration générale du système d'antennes TA est présentée à la Figure 9. Elle comprend une ouverture TA composée d'un réseau d'éléments déphaseurs, illuminés par une source située au niveau du point focal de l'antenne TA. Vraiment, les ondes sphériques émanant de la source sont collimatées en ajustant le retard de phase de chaque cellule (élément) unitaire de l'antenne TA. Dans le cas des antennes TA, la compensation de phase est généralement obtenue en utilisant les caractéristiques de phase des structures périodiques. Puisque la conception d'une antenne TA à ondes millimétriques est difficile au niveau des limitations de fabrication de la technologie standard de plaques à circuit imprimé peu coûteuse, une technique continue de mise en phase à 360 ° ayant des performances de faible perte s'avère nécessaire. Le déphasage est généralement obtenu en changeant les dimensions des composants de chaque cellule unitaire de l'ouverture de l'antenne TA.

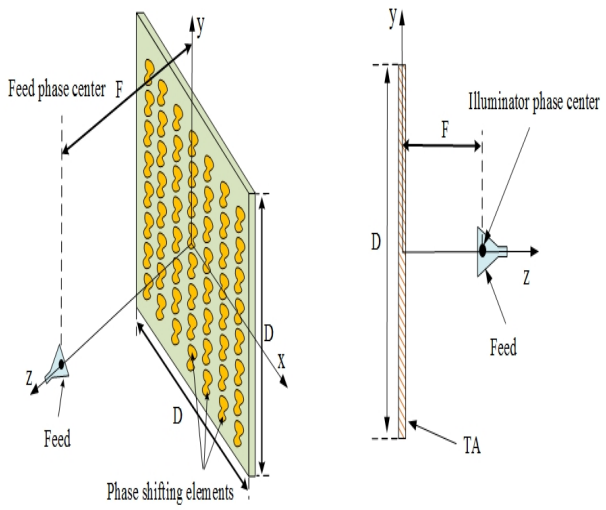

Figure 9 – Configuration d'une antenne à réseau d'émission (à lentille discrète).

Comme un autre élément essentiel pour les caractéristiques de rayonnement des antennes TA, leur source doit être aussi choisie et conçue de manière optimale pour ce qui est de la forme des faisceaux, du gain, de la polarisation croisée et du niveau des lobes latéraux. Notamment, pour les applications hautement efficaces, à faisceau ponctuel, elles sont généralement conçues pour créer un diagramme de rayonnement équilibré, ayant un faible niveau de polarisation croisée et les niveaux des lobes latéraux dans le régime de fréquence requis. Les antennes à ouverture sophistiquées, ayant un diagramme de rayonnement équilibré, à savoir un faible niveau des lobes arrière/latéraux, un faible diagramme symétrique de polarisation croisée avec des faisceaux égaux dans les plans E et H, sont utilisées comme sources pour les systèmes d'antennes focalisées à gain élevé [38]. Toutefois, elles sont trop coûteuses, encombrantes et complexes pour être fabriquées pour les applications à ondes millimétriques, inspirant les ingénieurs à chercher une autre alternative de configuration standard, qui soit rentable, légère, et qui ait de bonnes performances de rayonnement. En outre, afin d'accroître l'efficacité du système et d'en réduire les coûts, l'intégration directe de la source dans les circuits de radiofréquence doit être réalisable. Par conséquent, la conception d'une technologie planaire adéquate représente la structure la plus appropriée.

0.9 Le détecteur à diode

Tel que présenté à la section précédente, un démodulateur six-port comprend un corrélateur d'ondes six-port passif et des détecteurs à diode. Dans cette section, on explique brièvement les principes du détecteur à diode.

Essentiellement, le détecteur à diode redresse le signal RF d'entrée en un signal CC de sortie, par sa fonction de transfert I-V non-linéaire. Le dispositif non-linéaire commun est la diode de Schottky, où le courant passant par la diode est connecté à la tension RF d'entrée, comme indiqué dans l'équation (16) [51]. Dans cette équation, I_S est le courant saturé, q_o est la charge de l'électron, n, le coefficient d'idéalité, K, la constante de Boltzmann et T: la température.

$$i(t) = I_S.[exp(\frac{q_0 v_{RF}(t)}{nKT}) - 1] \tag{16}$$

En développant la fonction exponentielle, on peut montrer que la tension détectée passant par une résistance, dénommée vidéo résistance, est liée à la puissance d'entrée, à savoir $v_o(t) = \alpha.P_{in}$ où α est considéré comme un coefficient de sensibilité du détecteur.

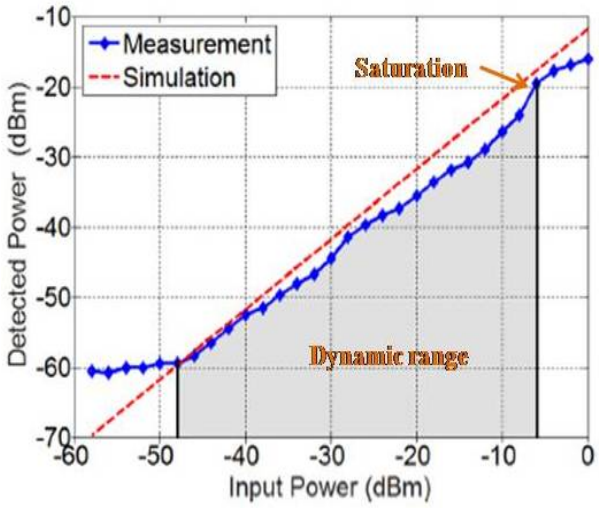

Figure 10 – Fonction de transfert simulée de la diode HSCH 9161 de Schottky en ADS.

La Figure 10 montre les zones opérationnelles d'un détecteur à diode simulé, basé sur le modèle SPICE de la diode HSCH 9161 de Schottky. La plage de la puissance d'entrée où la tension détectée a un rapport linéaire avec la puissance d'entrée s'appelle région quadratique. A des niveaux très faibles du signal d'entrée, la sortie est dominée par le bruit, tandis qu'à des niveaux très élevés, la sortie du détecteur n'est pas linéairement proportionnelle à la puissance du signal d'entrée et entre en saturation. Ainsi, pour avoir une communication fiable et pour améliorer la performance de liaison, l'augmentation de la plage dynamique de la diode du détecteur s'avère nécessaire. En outre, la conception d'un circuit d'adaptation d'entrée et d'un trajet de courant continu devrait être aussi envisagée dans notre projet. Dans cette thèse, on propose un détecteur équilibré de puissance ayant une largeur de bande du coefficient de réflexion supérieure à 10 GHz.

0.10 L'amplificateur à faible bruit

Dans notre architecture de récepteur proposée, on a utilisé, comme amplificateur à faible bruit (LNA), TGA4600 de TriQuint Semiconductor ayant un facteur de bruit (NF) de 4 dB et un gain actif de 13 dB, qui est directement connecté à l'antenne par la technique de micro câblage (wire-bonding). La photo du LNA utilisé dans le système récepteur qu'on a fabriqué est représentée à la Figure 11.

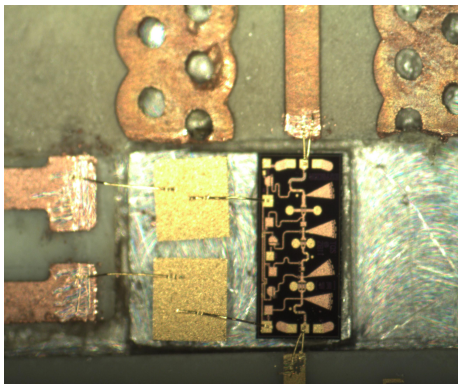

Figure 11 – Photo du LNA TGA4600 utilisé dans le récepteur proposé.

0.11 Méthodologie de recherche

Les structures émergentes les plus exotiques utilisées pour développer les antennes PDL à large bande sont conçues selon les propriétés de l'indice de réfraction à gradient (généralement appelé GRIN) des méta-matériaux [48] et [49]. Ces matériaux assurent idéalement une réponse à temporisation réelle pour les ondes électromagnétiques les traversant et ils représentent, ainsi, un bon choix pour la conception des lentilles à large bande. Par conséquent, dans la première partie de cette thèse, tel que décrit au premier chapitre, on analyse le potentiel de ces matériaux pour le développement d'une antenne PDL. Comme validation du concept, on a fabriqué un prototype à des fréquences inferieures (dans la bande de fréquence entre 7 et 12 GHz), et on a conclu que les tolérances de fabrication et de montage des technologies disponibles dans notre laboratoire ne sont pas assez précises pour redimensionner cette structure à la bande V. En plus, on a appris que la structure d'alimentation de PDL doit avoir une grande largeur de bande et qu'elle devrait illuminer de manière efficace son ouverture afin d'obtenir un faisceau hautement dirigé, ayant une faible performance au niveau du lobe latéral, tout en étant facilement intégré dans la partie RF.

Aux chapitres 2 et 3, on a conçu deux nouvelles structures différentes de rayonnement comme source pour l'antenne TA. Dans la première structure, on a conçu une antenne à résonateur diélectrique hybride, à cavité arrière (cavity-backed hybrid-dielectric-resonator antenna), intégrant des matériaux artificiels, pour illuminer l'ouverture PDL, dimensions 7.8 $cm\times$ 7.8 cm (conçue pour une directivité de 35 dB à 61 GHz). Alternativement, on profite des avantages des matériaux artificiels pour contrôler les ondes de surface de propagation/d'espace, en vue de développer une nouvelle antenne en réseau plan, ayant les propriétés de rayonnement désirées au niveau de l'antenne TA, et dont la fabrication est beaucoup plus facile par rapport au premier modèle. Les résultats obtenus montrent que lorsque les propriétés des matériaux artificiels sont utilisées d'une manière ciblée, on peut contrôler les performances de rayonnement de l'antenne en termes de gain, de largeur de bande, de niveau du lobe latéral et de forme du modèle. Par conséquent, on a choisi ce modèle comme source pour l'antenne TA.

Aux chapitres 4 et 5, on analyse la faisabilité d'un système d'antennes TA utilisant des filtres passe-bande sélectionnés en fréquences. Dans ces chapitres, il est montré qu'on peut concevoir l'antenne TA soit pour fournir un diagramme de rayonnement en forme (utile pour les communications

point-multi-point), soit un faisceau ponctuel. Celui ayant un gain de haute performance est démontré au chapitre 5, et les résultats de mesure prouvent le concept proposé.

Une architecture six-port a conversion directe est conçue et intégrée dans le système d'antennes TA. Au chapitre 6, on mesure les performances de ce récepteur pour différents schémas de modulation et on en présente les résultats. Au chapitre 7, on développe une antenne multifaisceaux à faible gain, basée sur une architecture de formation de faisceaux à matrice de Butler, en utilisant la technologie de fabrication MHMIC et on compare ses résultats de mesure aux résultats simulés. La thèse finit par quelques notes concernant les travaux futurs.

0.12 Contribution

Dans cette thèse, on présente la conception et la fabrication d'une antenne à gain élevé, intégrant un récepteur à six-ports. Les contributions scientifiques de ce projet sont incluses:

1) On a analysé la conception et la démonstration d'une lentille planaire à large bande, à gain élevé, ayant un indice de réfraction à gradient (GRIN), alimentée par une antenne slot a ouverture exponentielle (ATSA), afin d'identifier la faisabilité de cette structure pour les antennes à gain élevé, en bande V.

2) On a conçu un nouveau réseau d'antennes couples 2×4 surpassant son réseau planaire équivalent 4×4 au niveau de la largeur de bande, du gain et de la forme du modèle (améliorations de 176%, 1.6 dB, respectivement 11 dB). En outre, la complexité du réseau d'alimentation de structure en réseau a été simplifiée, en réduisant le nombre d'éléments excités. Vraiment, c'est la première structure qui valorise toutes les propriétés des matériaux artificiels pour atteindre ces performances uniques.

3) On présente une nouvelle antenne à résonateur diélectrique hybride à gain élevé (HDRA). Un résonateur diélectrique (DR) annulaire est activé par une antenne de connexion à ouverture couplée pour obtenir des résonances multiples et élargir la bande de l'antenne. En vue d'augmenter le gain de l'antenne, l'antenne HDRA est entourée par une cavité métallique. En outre, la performance de ce diagramme de rayonnement est améliorée par l'utilisation des anneaux métalliques reliés à la terre.

4) Une antenne à réseau d'émission (TA) à large bande et à gain élevé, fonctionnant à 60 *GHz*, est proposée. Pour répondre aux exigences de conception d'une antenne TA avec des performances de rayonnement insensibles à la polarisation, une cellule unitaire (UC) multicouche optimale est introduite, avec une réponse en phase de transmission linéaire, une plage de variation de 270 ° et une perte d'insertion inférieure à -3 *dB*, sur une bande de fréquence désirée de 58 GHz à 64 *GHz*.

5) La conception et l'optimisation de l'antenne TA à l'aide du logiciel électromagnétique commercial sont des tâches difficiles et elles pourraient s'avérer impossibles pour les antennes complexes de grandes dimensions (dimension >15 longueurs d'ondes). On développe un script général d'analyse Matlab rapide afin de concevoir de façon optimale l'antenne TA, en y incluant les effets des cellules unitaires TA et le diagramme de directivité. Ce programme analyse toute antenne TA à faisceau balayé, quelle que soit sa polarisation en moins de quelques secondes.

6) Conception, fabrication et caractérisation des éléments passifs de la structure six-port, y compris le coupleur hybride et le diviseur de puissance de Wilkinson, sur un substrat céramique de 10 mil, ayant une dimension de 2.54 $cm \times 2.54$ *cm*, à l'aide de la technologie MHMIC.

7) Afin d'analyser les performances du six-port proposé, un modèle de circuit six-port est simulé avec ADS, sur la base des paramètres S mesurés du coupleur hybride et du diviseur de puissance de Wilkinson et il est comparé à l'entière structure du six-port simulé en ADS Momentum.

8) Conception, fabrication et caractérisation du six-port proposé, sur un substrat céramique de 10 mil, pour obtenir une bonne isolation de 20 *dB* entre les ports RF et OL, ports d'entrée et de sortie correspondants, ayant un coefficient de réflexion inférieur à -20 *dB*.

9) Pour concevoir le détecteur de puissance, on profite des avantages de la configuration équilibrée. Premièrement, on fait une caractérisation de la diode de Schottky et, ensuite, sur la base de ses paramètres S mesurés, on en propose une configuration équilibrée, afin d'améliorer la plage dynamique de la diode de détection.

10) Afin de faciliter les mesures du récepteur proposé, à l'aide de notre équipement de laboratoire disponible, on a conçu, sur un substrat céramique de 10 mil, une transition entre la ligne micro ruban (MSL) et le guide d'ondes standard WR12.

11) Les mesures de système réalisées pour les schémas de modulation QPSK, 8PSK, 16QAM sont analysées pour une distance fixe, d (la distance entre l'émetteur et le récepteur). Les diagrammes de constellation mesurés de QPSK et 8PSK sont analysés pour les différentes plages de d.

12) On analyse une technique de formation de faisceaux en proposant une nouvelle configuration de matrice de Butler.

Bibliographie

[1] C. Dehos, J. L. González, A. D. Domenico, D. Kténas and L. Dussopt, "Mm-wave access and backhauling: the solution to the exponential data traffic increase in 5G mobile communications systems?," *IEEE Comm. Mag.*, vol. 52, no. 9, pp. 88-95, Sep. 2014.

[2] S. Yong and C. Chong, "An overview of multigigabit wireless through mm-wave technology: potentials and technical challenges," *EURASIP Journal on Wireless Comm. and Networking*, vol. 7, no. 1, pp. 50–60, Sep. 2006.

[3] P. Smulders, "Exploiting the 60 GHz band for local wireless multimedia access: prospects and future directions," *IEEE Comm. Mag.*, vol. 40, no. 1, pp. 140-147, Jan. 2002.

[4] P. Wang, Y. Li, L. Song, and B. Vucetic, “Multi-gigabit mm-wave wireless communication for 5G: from fixed access to cellular networks,” *IEEE Comm. Mag.*, vol. 53, no. 1, pp. 168-178, Jan. 2015.

[5] D. Lockie and D. Peck, "High-data-rate mm-wave radios," *IEEE Microwave Mag.*, vol. 10, no. 5, pp. 75-83, Aug. 2009.

[6] J. Wells, "Faster than fiber: The future of multi-G/s wireless," *IEEE Microwave Mag.*, vol. 10, no. 3, pp. 104-112, May 2009.

[7] T. Nitsche, C. Cordeiro, A. B. Flores, E. W. Knightly, E. Perahia and J. C. Widmer, "IEEE 802.11ad: directional 60 GHz communication for multi-Gigabit-per-second Wi-Fi [Invited Paper]," *IEEE Comm. Mag.*, vol. 52, no. 12, pp. 132-141, Dec. 2014.

[8] C. Dehos, J. L. Gonzalez, A. D. Domenico, D. Ktenas and L. Dussopt, "Mm-wave access and backhauling: the solution to the exponential data traffic increase in 5G mobile communications systems?," *IEEE Comm. Mag.*, vol. 52, no. 9, pp. 88-95, Sep. 2014.

[9] A. De Domenico, R. Gerzaguet, N. Cassiau, A. clemente, R. Derrico, c. Dehos, J. l. Gonzalez, D. Ktenas, L. Manat, V. Savin, and A. SiliGgaris, “Making 5g mm-wave communications a reality," *IEEE Wireless Comm.*, vol. 24, vol. 4, pp. 4-9, Aug. 2017.

[10] Y. Ghasempour, C. R. C. M. da Silva, C. Cordeiro and E. W. Knightly, "Next-generation 60 GHz communication for 100 Gb/s Wi-Fi," *IEEE Comm. Mag.*, vol. 55, no. 12, pp. 186-192, Dec. 2017.

[11] C. H. Doan, S. Emami, D. A. Sobel, A. M. Niknejad and R. W. Brodersen, "Design considerations for 60 GHz CMOS radios," *IEEE Comm. Mag.*, vol. 42, no. 12, pp. 132-140, Dec. 2004.

[12] T. S. Rappaport, J. N. Murdock and F. Gutierrez, "State of the art in 60-GHz integrated circuits and systems for wireless communications," *IEEE Proceedings*, vol. 99, no. 8, pp. 1390-1436, Aug. 2011.

[13] T. S. Rappaport, S. Sun, R. Mayzus, H. Zhao, Y.Azar, K. Wang, G. Wong, J. Schulz, and M. Samimi, "Mm-wave mobile communications for 5G cellular: it will work!," *IEEE Access*, vol. 1, no., pp. 335-349, 2013.

[14] J. G Andrews, S. Buzzi, W. Choi, S.V. Hanly, A. Lozano, A. C. K. Soong, J. C. Zhang, "What will 5G be?," *IEEE Journal on Selected Areas in Comm.*, , vol. 32, no. 56, pp. 1065-1082, Jun. 2014.

[15] P. Zhouyue, F. Khan, "An introduction to mm-wave mobile broadband systems," *IEEE Comm. Mag.*, vol. 49, no. 6, pp. 101-107, Jun. 2011.

[16] F. Boccardi, R. W. Heath, A. Lozano, T. L. Marzetta, P. Popovski, P., "Five disruptive technology directions for 5G," *IEEE Comm. Mag.*, vol. 52, no .2, pp.74-80, Feb. 2014.

[17] L. Verma, M. Fakharzadeh and S. Choi, "Backhaul need for speed: 60 GHz is the solution," *IEEE Wireless Comm.*, vol. 22, no. 6, pp. 114-121, Dec. 2015.

[18] W. Roh, J. Y. Seol, J. Park, B. Lee, J. Lee, Y. Kim, J. Cho, K. Cheun, and F. Aryanfar, “Mm-wave beamforming as an enabling technology for 5G cellular communications: theoretical feasibility and prototype results,” *IEEE Comm. Mag.*, vol. 52, no. 2, pp. 106-113, Feb. 2014.

[19] A. Maltsev, A. Sadri, A. Pudeyev, and I. Bolotin, "Highly directional steerable antennas: high-gain antennas supporting user mobility or beam switching for reconfigurable backhauling," *IEEE Mag. Vehicular Technology*, vol. 11, no. 1, pp. 32-39, March 2016.

[20] W. Hong et al., "Multibeam antenna technologies for 5G wireless communications," *IEEE Trans. Antennas Propag.*, vol. 65, no. 12, pp. 6231-6249, Dec. 2017.

[21] K. Sakaguchi, G. K. Tran, H. Shimodaira, S. Nanba, T. Sakurai, K. Takinami, I. Siadud, E. C. Strinati, A. Capone, I. Karls, R. Arefi, and T. Haustein, “Mm-wave evolution for 5G cellular networks,” *IEICE Trans. on Communication*, vol.98, no. 3, pp. 388-402, Mar. 2015.

[22] T. S. Rappaport, Y. Xing, G. R. MacCartney, A. F. Molisch, E. Mellios and J. Zhang, "Overview of mm-wave communications for fifth-generation (5G) Wireless Networks—With a Focus on Propagation Models," *IEEE Trans. Antennas Propag.*, vol. 65, no. 12, pp. 6213-6230, Dec. 2017.

[23] J. Kim, L. Xian, and A. Sadri, “60GHz modular antenna array link budget estimation with wiGig baseband and mm-wave specific attenuation,” *Hindawi International Journal of Antennas Propag.*, ID: 9073465, June 2017.

[24] IEEE 802.11 WG, “IEEE 802.11ad, amendment 3: enhancements for very high throughput in the 60 GHz band,” Dec. 2012.

[25] Part 15 Rules for Unlicensed Operation in the 57-64 GHz band; http://www.fcc.gov/document/part-15-rules-unlicensed-operation-57-64-ghz-band/.

[26] E. Hossain, M. Rasti, H. Tabassum and A. Abdelnasser, "Evolution toward 5G multi-tier cellular wireless networks: An interference management perspective," *IEEE Wireless Comm.*, vol. 21, no. 3, pp. 118-127, Jun. 2014.

[27] C. Wang et al., "Cellular architecture and key technologies for 5G wireless communication networks," *IEEE Comm. Mag.*, vol. 52, no. 2, pp. 122-130, Feb. 2014.

[28] K. Chandra, R. V. Prasad, B. Quang and I. G. M. M. Niemegeers, "CogCell: cognitive interplay between 60 GHz picocells and 2.4/5 GHz hotspots in the 5G era," *IEEE Comm. Mag.*, vol. 53, no. 7, pp. 118-125, Jul. 2015.

[29] T. S. Rappaport, F. Gutierrez, B-D. E, J.N. Murdock, Y. Qiao, J. I. Tamir, "Broadband mm-wave propagation measurements and models using adaptive-beam antennas for outdoor urban cellular communications," *IEEE Trans. Antennas Propag.*, vol. 61, no. 4, pp.1850-1859, Ap. 2013.

[30] L. Shafai, S. K. Sharma, and S. Rao, Handbook of reflector antennas and feed systems: volume 3- Applications of reflectors, USA, Artech House, 2013.

[31] J. Huang and J. A. Encinar, Reflectarray antennas, USA: Hobokem, New Jersye, IEEE press, John Wiley and Sons, Inc., 2007.

[32] L. Dussopt, A. Moknache, J. Saily, A. Lamminen, M. Kaunisto, J. Aurinslo, T. Bateman, and J. Francey, "A v-band switched-beam linearly polarized transmit-array antenna for wireless backhaul applications," *IEEE Trans. Antennas Propag.*, vol. 65, no. 12, pp. 6788-6793, Dec. 2017.

[33] B. Razavi, "Design considerations for direct-conversion receivers," *IEEE Trans. Circuits and Systems II: Analog and Digital Signal Processing*, vol. 44, pp. 428-435, 1997.

[34] S. Voinigescu, Handbook of high-frequency integrated circuits, Cambridge university press, 2013.

[35] S. O. Tatu, E. Moldovan, and S. Affes, " Multi-port front-end and transceivers for V-band multi-gigabit/s communication systems," *In F. Luo (Ed.), Digital Front-End in Wireless Communications and Broadcasting: Circuits and Signal Processing*, pp. 707-732, Cambridge: Cambridge University Press, 2011.

[36] S. O. Tatu, E. Moldovan, K. Wu, and R. G. Bosisio, "A new direct mm-wave six-port receiver," *IEEE Trans. Mic. Theory and Thech.*, vol. 49, pp. 2517-2522, 2001.

[37] L. Shafai, S. K. Sharma, and S. Rao, Handbook of reflector antennas and feed systems: volume 2-feed systems, USA, Artech House, 2013.

[38] David M. Pozar and Daniel H. Schaubert, Microstrip antennas: the analysis and design of microstripp antennas and arrays. USA: Wiley-IEEE Press, May 1995.

[39] S. Zihir, O. D. Gurbuz, A. Kar-Roy, S. Raman and G. M. Rebeiz, "60-GHz 64- and 256-Elements T. Sowlati et al., "A 60GHz 144-element phased-array transceiver with 51dBm maximum EIRP and ±60° beam steering for backhaul application," in IEEE International Solid -State Circuits Conference - (ISSCC), San Francisco, CA, pp. 66-68, 2018.

[40] S. Zihir, O. D. Gurbuz, A. Kar-Roy, S. Raman and G. M. Rebeiz, " 60GHz 64 and 256-element wafer-scale phased-array transmitter using full-reticle and subreticlestitching techniques," *IEEE Trans. Mic. Theory and Thech.*, vol. 64, no.12, pp. 4701-4719, Dec. 2016.

[41] B. Sadhu et al., "A 28-GHz 32-element TRX phased-array IC with concurrent dual-polarized operation and orthogonal phase and gain control for 5G communications," *IEEE Journal of Solid-State Circuits*, vol. 52, no. 12, pp. 3373-3391, Dec. 2017.

[42] K. Khalaf et al., "A 60GHz 8-way phased array front-end with TR switching and calibration-free beamsteering in 28nm CMOS," *43rd IEEE European Solid State Circuits Conference (ESSCIRC)*, Leuven, pp. 203-206, 2017.

[43] J. L. Gomez-Tornero, F. Quesada-Pereira, and A. Alvarez-Melcon, "Analysis and design of periodic leaky-wave antennas for the mm-wave band in hybrid waveguide-planar technology," *IEEE Trans. Antennas Propag.*, vol. 53, no. 9, pp. 2834-2842, Sept. 2005.

[44] R. Sauleau, P. Coquet, T. Matsui, and J. Daniel, "A new concept of focusing antennas using plane-parallel fabry-perot cavities with nonuniform mirrors," *IEEE Trans. Antennas Propag.*, vol. 51, no. 11, pp. 3171-3175, Nov. 2003.

[45] J. Thornton and K. Cheng-Huang, Modern lens antennas for communications engineering. Hoboken, NJ, USA: Wiley, 2013.

[46] J. Huang and J. A. Encinar, Reflectarray antennas, USA: Hobokem, New Jersye, IEEE press, John Wiley and Sons, Inc., 2007.

[47] L. Dussopt, A. Moknache, J. Saily, A. Lamminen, M. Kaunisto, J. Aurinslo, T. Bateman, and J. Francey, "A v-band switched-beam linearly polarized transmit-array antenna for wireless backhaul applications," *IEEE Trans. Antennas Propag.*, vol. 65, no. 12, pp. 6788-6793, Dec. 2017.

[48] M. Niroo Jazi, M. R. Chaharmir, J. Shaker and A. R. Sebak, "Broadband transmitarray antenna design using polarization-insensitive frequency selective surfaces," *IEEE Trans. Antennas Propag.*, vol. 64, no. 1, pp. 99-108, Jan. 2016.

[49] E. Erfani, M. Niroo-Jazi and S. Tatu, "A high-gain broadband gradient refractive index metasurface lens antenna," *IEEE Trans. Antennas Propag.*, vol. 64, no. 5, pp. 1968-1973, May 2016.

[50] Q. Lin and H. Wong, "A low-profile and wideband lens antenna based on high-refractive-index metasurface," *IEEE Trans. Antennas Propag.*, vol. 66, no. 11, pp. 5764-5772, Nov. 2018.

[51] M. Golio, The RF and microwave handbook: CRC press, 2000.

Première partie

Articles

Article 1

A High-Gain Broadband Gradient Refractive Index Metasurface Lens Antenna

E. Erfani, M. Niroo-Jazi, and S. O. Tatu

IEEE Transaction on Antenna and propagation, published, vol. 64, no. 5, pp. 1968-1973, 2016.

Abstract

On présente la conception et les résultats de simulation et de mesure d'une lentille planaire à large bande, à gain élevé, ayant un indice de réfraction à gradient (GRIN), alimentée par une antenne slot a ouverture exponentielle (ATSA). Comme élément constitutif de cette lentille, une nouvelle cellule unitaire en métamatériaux non-résonants, composée de triples anneaux rectangulaires bicouche est proposée, et son modèle de circuit équivalent est développé et décrit. On montre que, par l'utilisation de cet élément, on obtient des couplages capacitifs plus solides entre les couches métalliques adjacentes, se traduisant par une grande variation de l'indice de réfraction d'environ 2.5, et, par conséquent, on obtient une lentille mince, d'une épaisseur de $0.38\lambda_0$, où λ_0 est la longueur d'onde à 9.5 GHz. En plus, puisque la cellule unitaire est conçue pour résonner à des fréquences

plus élevées, sa réponse en indice de réfraction est légèrement augmentée sur une large gamme de fréquences, et cela améliore de manière considérable la largeur de bande de fonctionnement de la lentille. Les résultats de mesure obtenus prouvent une grande correspondance et un gain en largeur de bande à -3 dB de 52% (7-12 GHz), respectivement de 65% (7-13.2 GHz). En outre, cette lentille assure une grande efficacité d'ouverture de 50% (un gain de 21.2 dB) à la fréquence centrale, et les niveaux des lobes latéraux et de la polarisation croisée sont inférieurs à -20 dB, respectivement -26 dB, sur toute la bande correspondante.

Abstract

The design, simulation, and measurement results of a high gain broadband gradient refractive index (GRIN) planar lens fed by an antipodal exponential taper slot antenna (ATSA) are presented. As a constituent part of this lens, a novel non-resonant metamaterial unit cell, composed of bilayer triple rectangular rings, is proposed and its equivalent circuit model is developed and described. It is shown that, by utilizing this element, stronger capacitive couplings between adjacent metallic layers are realized resulting in a large refractive index variation of about 2.5, and hence, a thin lens with thickness of $0.38\lambda_0$, where λ_0 is wavelength at 9.5 GHz. In addition, since the unit cell is designed to resonate at higher frequencies, its refractive index response is smoothly increased over a broad frequency range and this considerably enhances the operating bandwidth of the lens. The achieved measured results demonstrate a broad matching and -3 dB gain bandwidths of 52% (7-12 GHz) and 65% (7-13.2 GHz), respectively. Furthermore, this lens offers a high aperture efficiency of 50% (21.2 dB gain) at the center frequency, and its side lobe and cross polarization levels are less than -20 dB and -26 dB across the entire matched band, respectively.

1.1 Introduction

Lens antennas have received considerable attention for microwave and millimeter wave applications since they offer the requirements of broadband and high gain performances through concentrating the radiated energy into a narrow beam-width in the desired direction. Traditionally, dielectric materials have been used as lenses, but they essentially suffer from their heavy and bulky profiles and also their machining process might be expensive [1]. As alternatives for dielectric lenses, resonant

and non-resonant sub-wavelength periodic structures such as frequency selective surfaces (FSSs) [2]-[4] and artificial materials (also named Metamaterials) [5]-[18] have been extensively employed to collimate the spherical waves into a focused beam. In particular, sub-wavelength metmaterials with peculiar properties of controlling the effective material parameters and hence manipulating propagation waves have been exploited to design various types of lenses for instance, negative index metamaterial lenses (NIM) [5], [6], zero index metamaterial lensed (ZIM) [7]-[10], and gradient index metamaterial lenses (GRIN) [11]-[18].

Indeed, lens antennas proposed in [7]-[10] have been constructed with non-planar 3D and planar 2D low/zero index metamaterial unit cells (LIMs/ ZIMs), where the near-zero permittivity and near-zero permeability effectively improve the radiation efficiency of the antennas. For instance in [7], a horn antenna is filled with miniaturized 3D ZIM elements incorporating four Koch-shaped cut wire resonator (KCR) and two-split resonator to obtain 1.6 dB gain improvement over the frequency range of 9-9.5 GHz. In ZIM lenses, although they are usually constructed with efficient elements operating in the tail of their resonances, but they still suffer from lack of bandwidth. Moreover, it appears that because of using high-Q resonant elements to exploit NIM properties, these lenses tend to be narrowband and dispersive as well.

Alternatively, a GRIN lens overcomes the drawbacks of narrow bandwidth and large transmission loss associate with other types of metamaterial lenses. Indeed, this works in non-resonant region and the refractive index response of its constructing unit cell is gradually varied throughout the lens aperture. Luneburg [16], [17] and Maxwell fisheye net lenses [16], [18] are some of these GRIN configurations with different refractive index distributions which have been proposed so far. In [16], a 3D half-spherical Luneburg lens with distribution of $n = (2 - r^2/R^2)^{0.5}$ has been designed to work at center frequency of 15 GHz with a refractive index variation of 0.8. Despite of obtaining good results, this 3D Luneburg is bulky since it has been constructed with 35 spherical shells (each shell is 2 mm). Similarly, a refractive index distribution of $n = (1 + r^2/R^2)$ have been utilized in [18] to realize a Half Maxwell fisheye (HMFE) lens with thickness of 120 mm by tailoring the physical parameters of a fractal unit cell in non-resonant region. A refractive index variation of 0.9 has been obtained to design this lens. It can be concluded that in order to achieve an efficient, high gain, and broadband thin lens antenna, a unit cell with a large gradual variation range of refractive index response is strictly required. In addition, the feed antenna also needs to be broadband and provide the required symmetric radiation pattern with low side lobe and cross polarization levels.

In this work, a new bilayer GRIN metamaterial unit cell consisting of three rectangular rings with a large refractive index variation range of around 2.5 is proposed to construct a broadband, high efficient, thin lens antenna. The transmission characteristics of this element are described and an equivalent circuit model is developed by using Advanced Design System (ADS) software to delineate its scattering mechanism. Based on the refractive index response of the proposed element and the radiation patterns of an optimized antipodal exponential taper slot antenna (ATSA), as its feed, a GRIN metamaterial lens with the aperture size of $4.56\lambda_0 \times 4.56\lambda_0 \times 0.38\lambda_0$ is fabricated and measured. The achieved results are presented demonstrating excellent performances in terms of bandwidth, efficiency, gain enhancement, and side lobe and cross polarization levels across a broad frequency range.

1.2 GRIN Metamaterial Lens Antenna Design

The configuration of GRIN metamaterial lens antenna is schematically shown in Fig. 1.1. It consists of a planar surface with dimension of D and thickness of T, which is centrally illuminated by a radiator placed at the focal distance of F far from the surface. This surface is composed of an array of small unit cells with different refractive index varying across the lens aperture. In order to achieve a high gain collimated radiation pattern, each unit is designed to compensate the differential spatial delay of the spherical wave ray emanated from the phase center of the feed and impinged on the center of that unit cell with respect to the ray passing through the center of the lens aperture [15]. The phase compensation is achieved by independently changing the geometrical dimensions of metallic pattern of unit cells across the lens aperture.

To achieve a low cost and high efficient lens antenna, both illuminator and unit cell must be deliberately designed. Therefore, in the first step, a new bilayer broad band metamaterial unit cell with a wide variation range of refractive index is designed as a constituent part of the lens. Then a planar antipodal exponential taper slot antenna (ATSA) is chosen and optimized to achieve the required criteria. Depending on the desired gain value, the aperture size of the lens D is chosen and the focal distance F is determined to match -10 dB radiation pattern beam width of the feed to the diameter of the lens aperture [3]. In fact, this results in a high efficient radiation pattern with a good side lobe level performance. Accordingly, the refractive index distribution of each unit cell across the lens aperture is calculated by

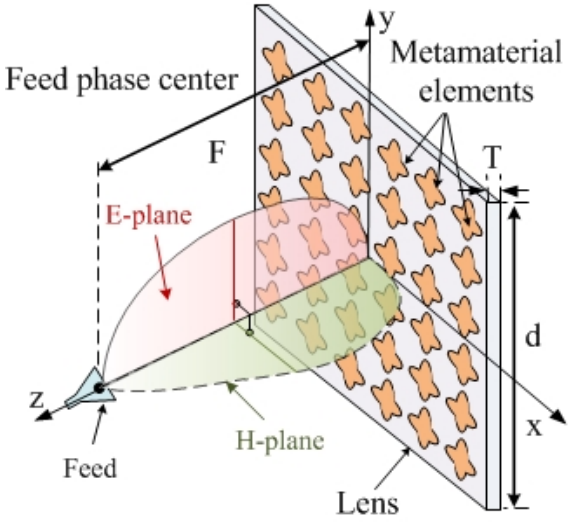

Figure 1.1 – Schematic representation of the proposed GRIN metamaterial lens.

$$N_{(m,n)} = N_0 - \frac{\left(x_{(m,n)}^2 + y_{(m,n)}^2 + F^2\right)^{0.5} - F)}{T} \tag{1.1}$$

where $x_{(m,n)}$, $y_{(m,n)}$ is the location of the unit cell in the aperture, F is the focal distance and N_0 is the maximum refractive index at the center of the aperture. It can be observed from equation (1.1) that the thickness of the lens will be decreased when a refractive index with larger variation range is requested. In the proposed unit cell, by realizing a strong capacitive coupling effect between the metal strips, the refractive index range is considerably increased and hence the thickness of lens is decreased while it operates over a broadband frequency range with low dispersion loss (negligible permeability imaginary part). The detailed design procedures and desired electromagnetic characteristics of each part of GRIN lens antenna are described in the following sub-sections.

1.2.1 Unit Cell Design

The proposed metamaterial unit cell, as shown in Fig. 1.2a, consists of three rectangular-shaped metallic strips which are symmetrically etched on both sides of a dielectric material RO4350B with ϵ_r=3.48, h_1=0.338 mm, and h_2=0.017 mm. The main goal of this unit cell is to achieve a maximum variation range of refractive index with minimum dispersion loss over a broad frequency range.

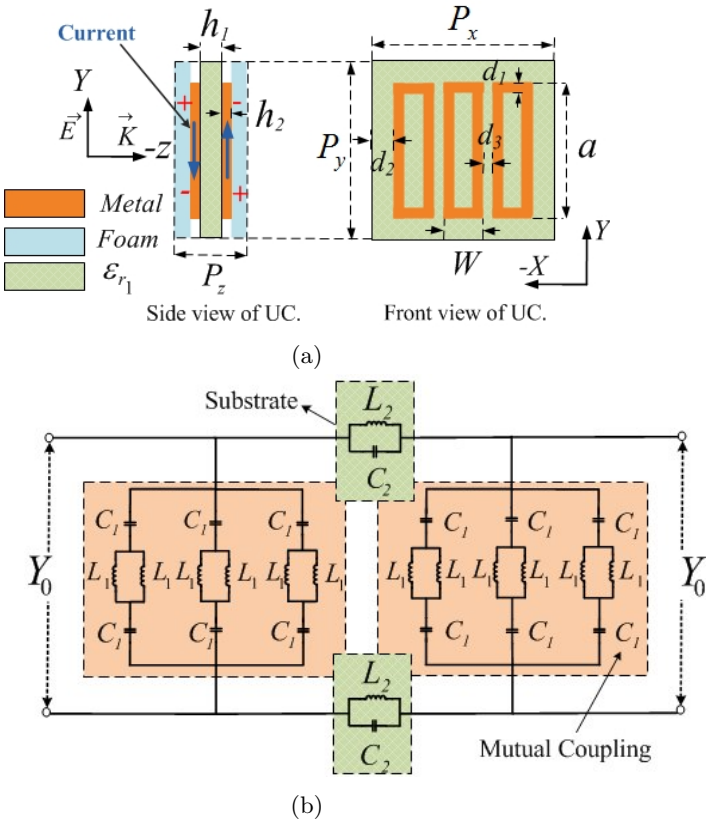

Figure 1.2 – (a)Configuration of the proposed metamaterial unit cell (UC) with dimensions P_x=P_y=4, P_z=2.4, h_1=0.338, h_2=0.017, d_1=0.2, d_2=0.25, d_3=0.16, and W=1.06 (all units are in mm), (b). Equivalent circuit model of the proposed UC. The values of parameters for L=3.6 mm are L_1=232 nH, L_2=8 nH, C_1=1.15 fF, and C_2=2.5 fF.

To characterize and investigate the scattering response of this unit cell, periodic perfect electric and magnetic boundary conditions are applied along the y and x directions of the unit cell, respectively, and it is excited with a normal incident field as shown in Fig. 1.2a. The unit cell is simulated with CST Microwave Studio. As the unit cell is excited with a linear vertically polarized electromagnetic wave propagating in the -z direction, the incident electric field induces an anti-parallel current on this bilayer metallic pattern. This produces an opposite electrical charges localized at the end of strips [19]. The induced current distributions on each vertical strip of metallic rectangular rings can be represented by an inductance L_1. The substrate thickness and coupling between opposite electrical charges in both sides of the substrate are described by employing an equivalent inductance and capacitance L_2 and C_2, respectively. In addition of this intra coupling, because of the interaction between the metallic squares of neighbor unit cells, large amounts of charges are accumulated on the horizontal strips of each square ring that can be accounted as C_1. By understanding the reaction of unit cell to the incident electromagnetic wave, an equivalent circuit model is developed

and depicted in Fig. 1.2b. In this equivalent circuit model, the effects of dielectric and conductor losses are neglected. The parameters' values of this equivalent circuit model are calculated using ADS software. The calculated transmission coefficient responses (amplitudes and phases) using the proposed equivalent circuit model, for the unit cell with dimension of L=3.6 mm as an example, are compared in Fig. 1.3 with the results obtained from full wave simulation carried out by CST software. It can be found that both results agree very well validating the proposed equivalent circuit model.

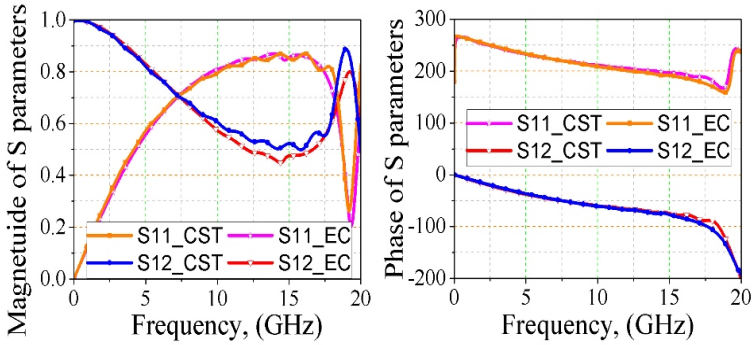

Figure 1.3 – Scattering parameters of the proposed unit cell (UC) obtained from CST and equivalent circuit (EC) model.

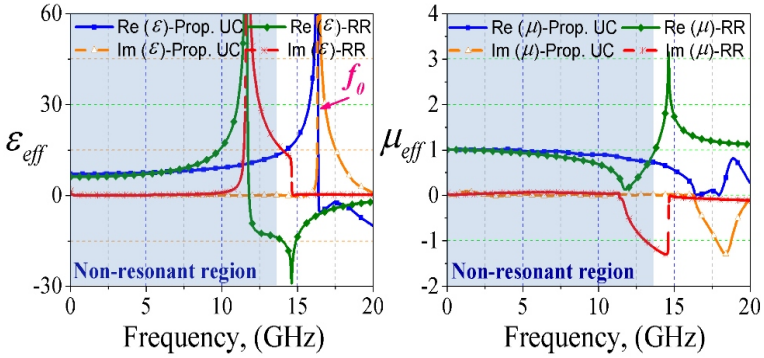

Figure 1.4 – Comparison of retrieved effective permittivity and permeability of the proposed unit cell (UC) and rectangular ring (RR) for L=3.6 mm.

By having the simulated scattering parameters and the slab width of 2.4 mm, the effective constitutive parameters of proposed unit cell are extracted through Kramers-Kronig relations [20] and are illustrated in Fig. 1.4. It can be observed that the permittivity curve undergoes an electrical resonance while the permeability exhibits anti-resonance around f_0=16.5 GHz. At frequencies lower than f_0, the real part of permittivity monotonically increases as frequency increases while the effective permeability almost remains near unity and the imaginary parts are also near zero which

indicates a weak dispersion loss. Hence, working in non-resonant region, enable us to achieve an efficient control of the effective parameters over broadband frequency range.

To illustrate the advantages of proposed unit cell, a rectangular ring (RR) element etched on one side of a unit cell with same dimensions and dielectric parameters is simulated and then its retrieved effective parameters are compared with the ones of proposed unit cell as shown in Figs. 1.4 and 1.5. The simulated curves in Fig. 1.4 demonstrate that by utilizing the triple ring unit cell, the resonant frequency f_0 shifts toward higher frequencies and hence stable effective parameters over a wide range of frequency from DC to near f_0 is realized. In addition, using two layers of triple squares on both sides of the substrate leads to a strongly capacitive coupling effect and the refractive index value is increase to up to 4.5 for L=3.9 mm. Indeed, this facilitates the design of thin broadband gradient lens antenna. As illustrated in Fig. 1.5, it can be observed that by changing the length of L from 0.1 to 3.85 mm, the refractive index varies from 1.2 to 3.7 which is sufficient for realization of a low loss gradient index lens with small thickness. This peak refractive index and its variation range are considerably larger than the ones achieved in [16] and [18]. Moreover, utilizing this unit cell as an element of the lens can also improve the cross-polarization level of the waves passing through it since it is highly polarization selective (the length horizontal strips are small and hence they do not support strong x-polarized current component).

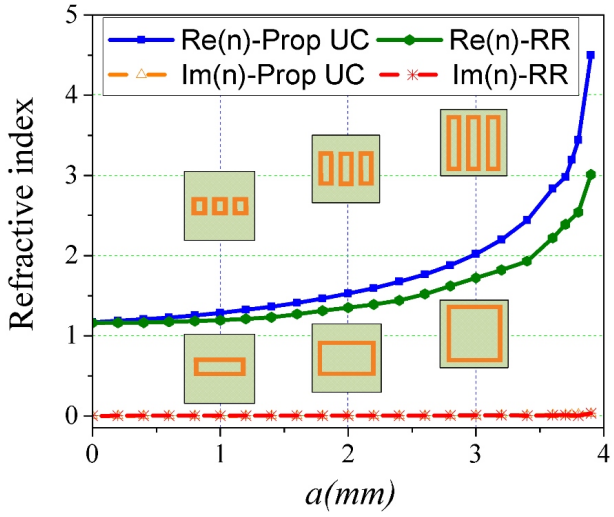

Figure 1.5 – Refractive index parameter of the proposed unit cell as a function of L compared to its RR element.

1.2.2 Feed Design

To have a broadband, high efficient lens antenna, a wideband balanced and stable radiation pattern feed with low cross polarization and side lobe levels is ideally desired. In this work, a planar ATSA with a broadband substrate integrated waveguide (SIW) feeding structure is chosen as a feed and it is optimized to obtain an almost symmetric radiation pattern for the -10 dB beam width (73 ° and 74 ° in E- and H-planes at 9.5 GHz , respectively) and cross polarization level of less than -20 dB across more than 4 GHz frequency region (47%) of -10 dB well-matched and -1 dB gain responses. To match the radiating exponential flared slot section of ATSA to a microstrip feed line, SIW and linearly tapered microstrip transition sections are used [21]. In addition, the outer edges of ATSA are corrugated to improve the shape of antenna radiation pattern and its side lobe level as shown in Fig. 1.6. All parameters are optimized for the central frequency 9.5 GHz with CST Microwave Studio.

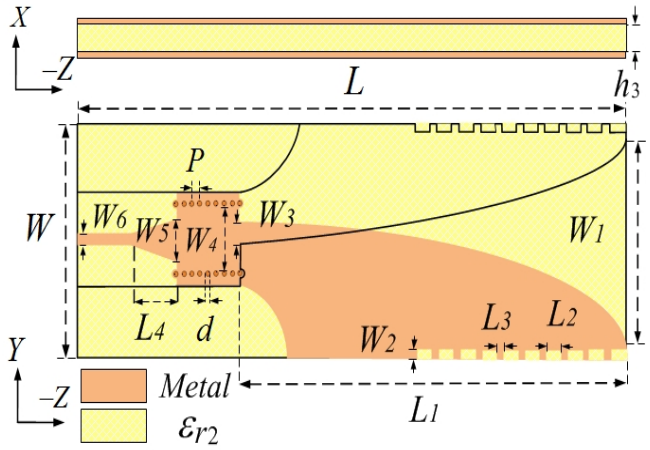

Figure 1.6 – Configuration of ATSA with SIW feeding structure. The antenna dimensions are: ϵ_{r2}=2.94, h_3=0.508, L=148.3, W=50, L_1=88.8, L_2=2.4, W_1=34.6, W_2=6.2, W_3=5.52, W_4=15.9, W_5=5.36, and P=2.2 (all units are mm).

As another crucial parameter that should be considered, it is the phase center location of the ATSA where the electromagnetic radiation spreads spherically. To avoid spatial delay compensation errors and to obtain efficient and broadband collimation in the design of lens antennas, a balanced feed with unique and stable phase center location in the E- and H-planes is ideally required. Indeed, the phase of far field pattern originated from the phase center position of the feed must be stationary within -10 dB beam width and across the desired gain bandwidth. This issue has been evaluated for the ATSA and it is shown in Fig. 1.8. These phase patterns have been calculated for the averaged E- and H-planes phase center locations ($x = 0, y = 0, z = -109.5$) at the center frequency 9.5 GHz.

It can be observed that the phase of radiation patterns in E-and H-planes, are almost uniform within -10 dB beam width across the desired operating band (averaged E- and H-planes beam width in the worst case at 8 GHz is 78 °). Indeed, because of the variation of -10 dB beam width of H-plane pattern across the frequency range, 86 ° at 8 GHz and 64 ° at 11 GHz, some errors will be introduced for the off-broadside angles close to -10 dB tapering level of H-plane phase pattern especially at 11 GHz. However, since the power level is considerably low at the edge of aperture, it cannot significantly affect the radiation pattern of the lens antenna. Moreover, by investigating the phase center locations at the lower and higher edges of the interested operating band it is revealed that the variation phase centers for both planes are less than 2 mm in the axial direction (i. e., $-z$) and hence a stable phase center location is realized. Therefore, fulfilled required radiation characteristics including, a flat phase pattern over -10 dB beam width for both planes, an almost stable phase center location in the desired bandwidth, a good matching, and stable broadband gain make ATSA a good option to feed the proposed lens.

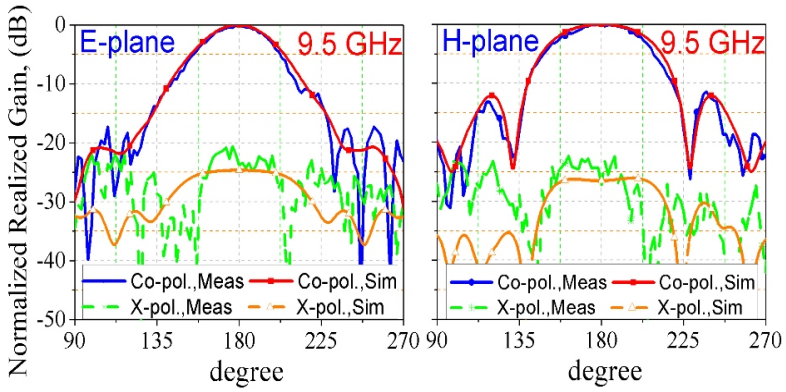

Figure 1.7 – Simulated and measured radiation pattern of ATSA.

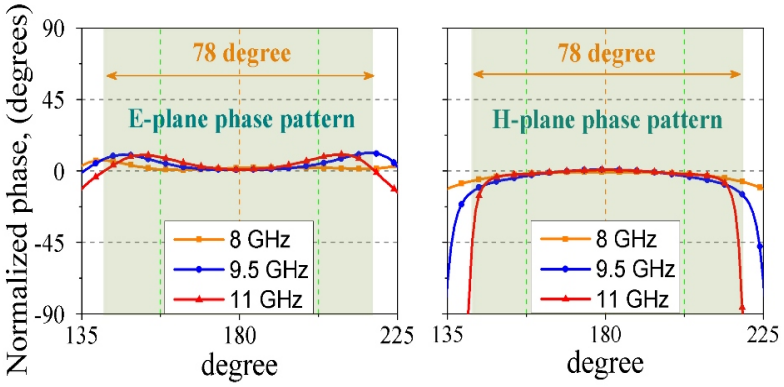

Figure 1.8 – Far field patterns of ATSA which have been determined with respect to its averaged phase center calculated at 9.5 GHz.

1.3 Simulation and Experimental Results

The metamaterial lens with aperture size of $D = 4.56\lambda_0 = 144\,mm$ and F/D=0.7 is centrally illuminated by ATSA antenna as the phase center of the feed is located at the focal point of the Lens. To collimate the feed radiation in to the broadside direction (-z direction), the required refractive index of each elements are calculated by the expression equation (1.1) and are illustrated in Fig. 1.9 for the refractive index variation range of 2.5 from 1.2 to 3.7 and the lens thickness of 12 mm. Since the periodicity of proposed unit cell in the z-direction is P_z=2.4 mm, at least six similar layers with refractive index distribution as the one shown in Fig. 1.9 are required to realize the desired thickness for this lens. Therefore, six layers of RO4350B with thickness of which are separated by two 1 mm foam layers with permittivity near unity are used. Each dielectric layer is composed of unit cell. It needs to be noted that the length of unit cell is 4 mm which is around $\lambda_0/10$, where λ_0 is the wavelength at 9.5 GHz.

To calculate the characteristics of the proposed GRIN Lens antenna, the entire structure which consists of the feed and Lens are simulated with transient solver of CST software. Then, the prototype was implemented through conventional printed circuit board technology. Some holes were also drilled into the substrate to align the substrates and also tie them together by using a few nylon screws. Fig. 1.10 demonstrates a photograph of the fabricated lens, its feed, and the measurement setup prepared inside the anechoic chamber. The measured reflection coefficient of the assembled lens antennas is shown in Fig. 1.11, and it is in good agreement with the simulated ones. It is also revealed that, except some small deviation around 8 GHz, the lens has a -10 dB reflection coefficient bandwidth ranging from 6.7 GHz to frequencies larger than 12 GHz. By comparing the reflection coefficient responses of the feed (not shown here for briefness) and lens, it can be concluded that the lens doesn't deteriorate the impedance matching of the illuminator.

The normalized E- and H-plane radiation patterns of the feed and lens antennas were measured inside the anechoic chamber and are compared with the simulated ones as exhibited in Figs. 1.7 and 1.12. The radiation patterns of feed antenna are shown only at the center frequency for brevity; while they are presented at three different frequencies across the achieved bandwidth for the lens antenna. As it can be noticed in these figures, there are good consistency between the simulation and measurement radiation patterns for both feed and lens antennas. Moreover, the lens antenna offers good high gain radiation pattern across a broad frequency range of 7-12 GHz. It has side

lobe level less than -20 *dB* and cross-polarization levels better than -26 *dB* for both E- and H-plane patterns across the entire 7-12 *GHz* bandwidth. To further assess the performance of proposed lens antenna, the realized gain of both feed and lens were measured using gain comparison method [22] and are compared with the simulated ones in Fig. 1.11. The results demonstrate that an averaged gain enhancement of 9.5 *dB* across 5 GHz frequency range is realized. The measured and simulated -3 *dB* gain bandwidth for this lens are 65% (7- 13.2 *GHz*) and 65% (6.7- 12.9 *GHz*), respectively. The slightly frequency shift noticed for this bandwidth might be due to the implementation tolerance caused by antenna assembly and also accuracy of measurements.

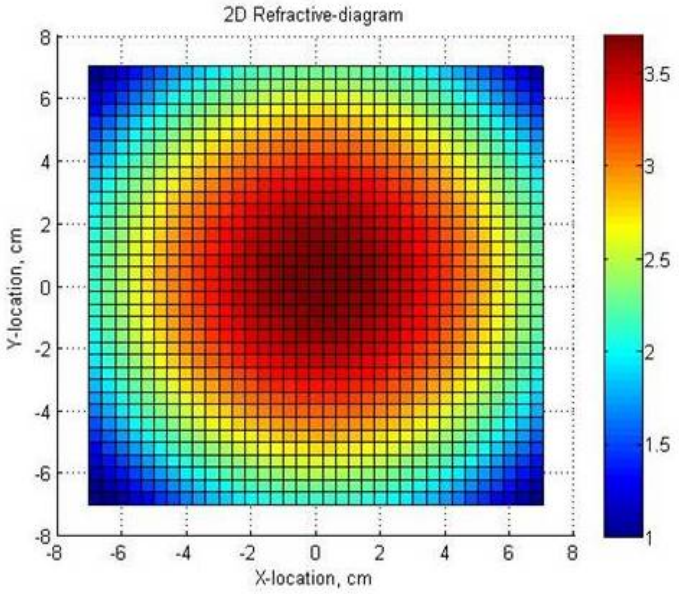

Figure 1.9 – Refractive index distribution of the GRIN lens antenna.

The antenna efficiency at certain frequency is also calculated by $\eta = G_m/D_{max}$, where G_m is the measured gain and D_{max} is the maximum directivity that is defined as

$$D_{max} = \frac{(4D^2\pi)}{\lambda^2} \tag{1.2}$$

where D is the physical size of lens, and λ is the wavelength at that frequency. The results indicate that the proposed lens offer at least 50% antenna efficiency at the center frequency 9.5 *GHz* and its peak efficiency is 52% at frequency 7 *GHz*.

In order to distinguish our remarkable results from other works in [4], [7], [9], and [16], Table 1.1 is provided. In [4], eight layers of FSS lens are stacked together with seven layers of bonding

Figure 1.10 – Photos of fabricated lens, its feed and its radiation pattern measurement setup.

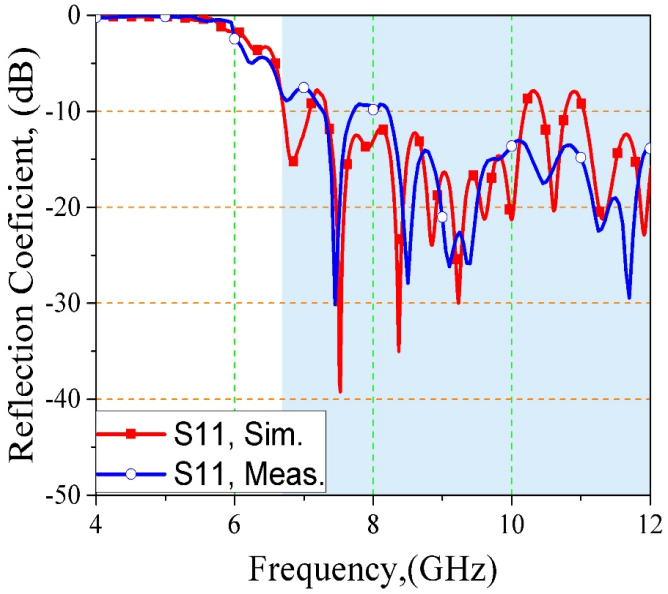

Figure 1.11 – Simulated and measured reflection coefficient of structure.

materials resulting in a total thickness of 0.78λ ($26.1\,mm$) and an aperture size of 6.6λ. This multi-beam lens shows consistent radiation pattern across 22.2% bandwidth (8-10 GHz) with a maximum measured directivity of about 21 dB, which is translated to 23% aperture efficiency based on the above mentioned calculation method. As it appears, the proposed GRIN lens in this work out performs the FSS based lens antenna in [4], generally in terms of all radiation characteristics. Alternatively, the reported results of the lens structure in [7], which is based on bulky 3D anistropic

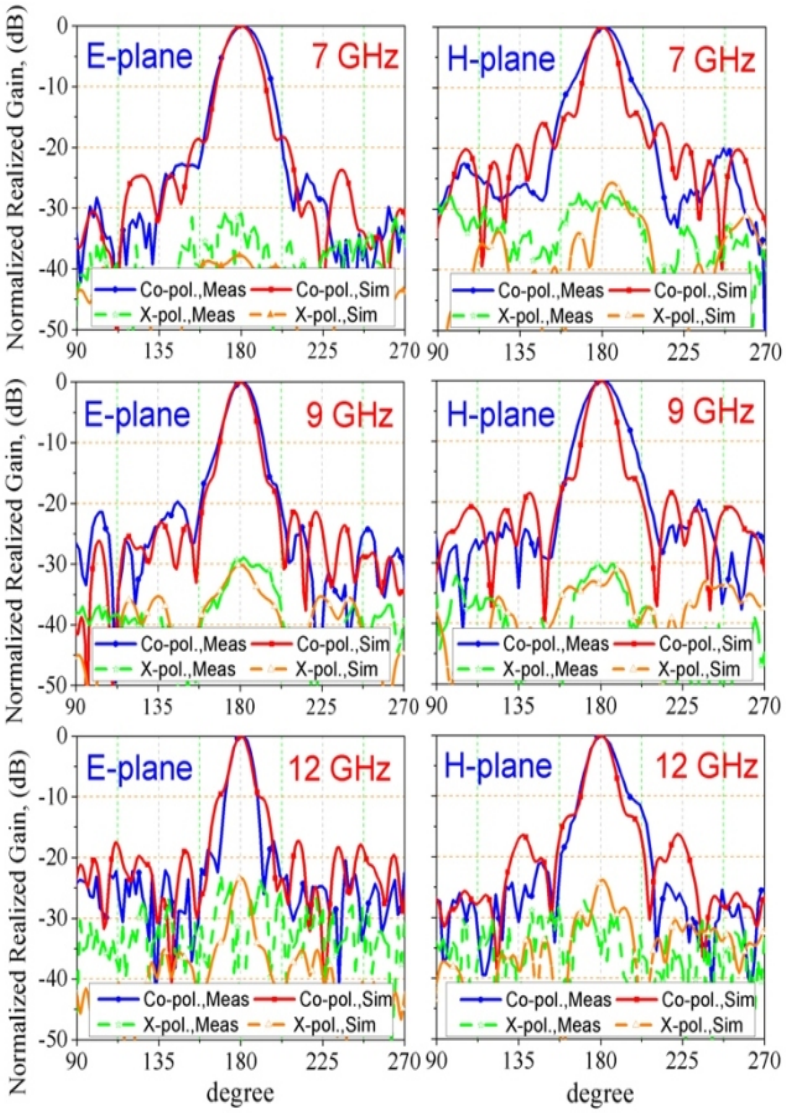

Figure 1.12 – Simulated and measured radiation patterns of the proposed lens for different operating frequencies across the desired bandwidth.

ZIM show that not only their antenna suffers from the lack of bandwidth, but also it distort the radiation pattern of a horn (especially in terms of side lobe).Similarly, the results presented for 3D bulky zero/low-index metamaterial lenses in [9] show a narrow gain bandwidth performance of about 15%. Furthermore, the 3D fish-eye lens demonstrated in [16] is very bulky and its gain response increases with frequency. In brief, most of the metamaterial lenses designed with LIM/ ZIM materials, although they have high aperture efficiency, they are narrow band and bulky. Moreover, most of other addressed lenses constructed with GRIN are also bulky and their gain responses are changing with frequency.

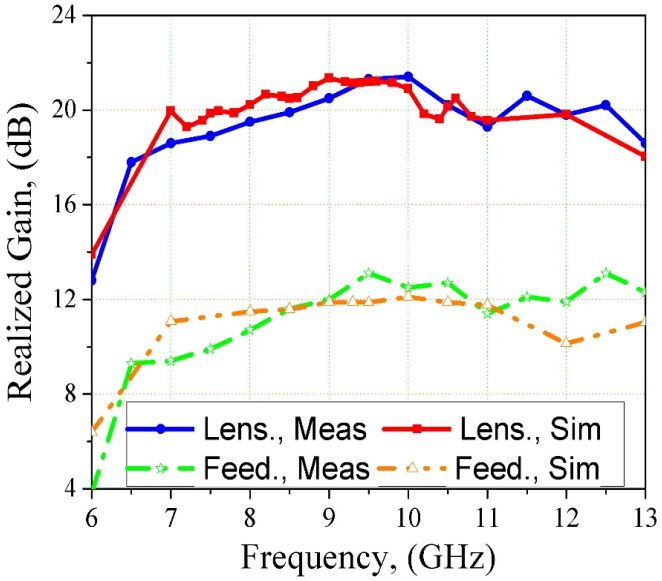

Figure 1.13 – Simulated and measured realized gain of Lens and Feed.

Tableau 1.1 – Comparison of our result with other works.

	Proposed structure	[4]	[7]	[9]	[16]
-3 dB gain bandwidth (%)	65% (7-13.2 GHz)	≥22.2%	-	-	-
Aperture efficiency (%)	50	23	90	90	62.6
Thickness (λ)	0.38λ	0.78λ	0.28λ	0.14λ	0.33λ
Aperture area (λ^2)	4.56×4.56	6.6×6.6	3.76×2.82	1.14×1.14	28

1.4 Conclusion

A high gain, broad band thin GRIN metamaterial lens have been designed and successfully demonstrated. It has been shown that by judiciously controlling the scattering properties of a material unit cell, its gradient-refractive-index can be considerably enhanced and accordingly the thickness of lens is significantly decreased. Moreover, by shifting up the resonant frequency of the unit cell, the operating response of the designed lens is enhanced. By appropriately selecting a feed antenna and deliberately designing the lens configuration, a high gain broadband radiation pattern response with low side lobe (less than -20 dB) and cross polarization (better than -26 dB) levels was realized. The cross polarization of lens antenna was better than its feed by at least 8 dB. Fairly

outperforming most of the cited works in terms of the radiation characteristics, ease of fabrication (being planar), and small thickness, it was demonstrated that the proposed GRIN lens offers a high aperture efficiency of 51% with almost stable radiation characteristics across a broad operating range of 52%.

Bibliographie

[1] T. L. A. Rhys, "The design of radially symmetric lenses," *IEEE Trans. Antennas Propag.*, vol. 18, no. 4, pp. 497- 506, Jul. 1970.

[2] L. Meng, M. A. Joumayly, and N. Behdad, "Broadband True-Time-Delay Microwave Lenses Based on Miniaturized Element Frequency Selective Surfaces," *IEEE Trans. Antennas Propag.*, vol. 61, no. 3, pp. 1166- 79, Mar. 2013.

[3] M. Niroo-Jazi, A. R. Sebak, M. Chaharmir, and J. Shaker., "Applications of Polarization-Independent Frequency Selective Filters for Transmitarray Antennas," *IEEE Int. Sym. On Ant. And Propag.*, Jul. 2014.

[4] S. M. A. M. H Abadi, N. Behdad, "Design of Wideband, FSS-Based MultiBeam Antennas Using the Effective Medium Approach," *IEEE Trans. Antennas Propag.*, vol. 62, no. 11, pp. 5557- 64, Nov. 2014.

[5] B. Pendry, "Negative Refraction Makes a Perfect Lens," *Phys. Rev. Lett.*, vol. 85, pp. 396, Oct. 2000.

[6] R. B. Greegor, C. Parazzoli, J. Nielse,M. A Thompson, M. H. Tanielian, and D. R. Smith, "Simulation and Testing of a Graded Negative Index of Refraction Lens," *Appl. Phys. Lett.*, vol. 87, pp. 091114 /1- 3, Aug. 2005.

[7] H. Xu, G. Wang, and T. Cai., "Miniaturization of 3-D Anistropic Zero-Refractive-Index Metamaterials With Application to Directive Emissions," *IEEE Trans. Antennas Propag.*, vol. 62, no. 6, pp. 3141-9, Jun. 2014.

[8] D. Li, Z. Szabo, X. Qing, E-P. Li, and Z. N. Chen, "A High Gain Antenna With an Optimized Metamaterial Inspired Superstrate," *IEEE Trans. Antennas Propag.*, vol. 60, no. 12, pp. 6018-23, Dec. 2012.

[9] J. Turpin, Q. Wu, D. Werner, B. Martin, M. Bray, and E. Lier, "Low Cost and Broadband Dual-Polarization Metamaterial Lens for Directivity Enhancement," *IEEE Trans. Antennas Propag.*, vol. 60, no. 12,. pp. 5717- 26, Dec. 2012.

[10] L. Yuan, W. X. Tang, H. Li, Q. Cheng, and T. J. Cui., "Three-Dimensional Anisotropic Zero-Index Lenses," *IEEE Trans. Antennas Propag.*, vol. 62, no. 8, pp. 4135-42, Aug. 2014.

[11] D. R. Smith, J. J. Mock, and D. Schurig, "A Gradient Index Metamaterials;" *Phys. Rev.*, vol. 71, no. 3, pp. 036609/1-5, Mar. 2005.

[12] X. Q. Lin, T. J. Cui, J. Y. Chin, X. M. Yang, and R. Liu, "Controlling Electromagnetic Waves Using Tunable Gradient Dielectric Metamaterial Lens," *Appl. Phys. Lett.*, vol. 92, pp. 131904/1-3, Ap. 2008.

[13] O. Paul, B. Reinhard, B. Krolla, R. Beigang, and M. Rahm, "Gradient Index Metamaterial Based n Slot Elements, " *Appl. Phys. Lett.*, vol. 96, no. 24, pp. 241110/1- 3, June. 2010.

[14] X. Chen, H. F. Ma, X. Y. Zou, W.X. Jiang, and T. J. Cui, "Three-dimensional Broadband and High-directivity Lens Antenna Made of Metamaterials," *Appl. Phys.* vol. 110, pp. 044904/1-8, Aug. 2011.

[15] H. Ma, X. Chen, X. Yang, W. Jiang, and T. Cui,"Design of Multibeam Scanning Antennas with High Gains and Low Sidelobes Using Gradient Index Metamaterials," *Appl. Phys. vol.* 107, pp. 014902/1-9, Jan. 2010.

[16] H. F. Ma, B. G. Cai, T. X. Zhang, Y. Yang, W. X. Jiang, and T. J. Cui, "Three-Dimensional Gradient-Index Materials and Their Applications in Microwave Lens Antennas," *IEEE Trans. Antennas Propag.*, vol. 61, no. 5, pp. 2561-9, May. 2013.

[17] A. Dhouibi, S.N. Burokur, A. Lustrac, and, A. Priou, "Compact Metamaterial-Based Substrate-Integrated Luneburg Lens Antenna," *IEEE Antennas Wireless Propag. Lett.*, vol. 11, pp.1504-07, Jan. 2012.

[18] H. X. Xu, G. M. Wang, Z. Tao, and T. Cai, "An Octave-Bandwidth Half Maxwell Fish-Eye Lens Antenna Using Three-Dimensional Gradient-Index Fractal Metamaterials," *IEEE Trans. Antennas Propag.*, vol. 62, no. 9, pp. 4823-28, Sept. 2014.

[19] S. N. Burokur, A. Sellier, B. Kanté, and A. de Lustrac,"Symmetry Breaking in Metallic Cut Wire Pairs Metamaterials for Negative Refractive Index," *Appl. Phys. Lett.*, vol. 94, pp. 201111 /1- 3, May. 2009.

[20] Z. Szabo, G. H. Park, R. Hedge, and E. Li, "A Unique Extraction of Metamaterial Parameters Based on Kramers–Kronig Relationship," *IEEE Trans. Mic. Theory Thechn.*, vol. 58, no. 10, pp. 2646- 53, Oct. 2010.

[21] F. Taringou, D. Dousset, J. Bornemann, and K. Wu, "Broadband CPW Feed for Millimeter-Wave SIW-Based Antipodal Tapered Slot Antenna," *IEEE Trans. Antennas Propag.*, vol. 61, no. 4, pp. 1756- 62. Ap. 2013.

[22] M. Niroo-Jazi and T. A. Denidni, "Frequency Selective Surfaces and Their Applications for Nimble-Radiation Pattern Antennas," *IEEE Trans. Antennas Propag.*, vol. 58, no. 7, pp. 2227-37, Jul. 2010.

Article 2

A Broadband and High Gain Millimeter-Wave Hybrid Dielectric Resonator Antenna

E. Erfani, T. Denidni, and S. O. Tatu

International Symposium on Antenna Technology and Applied Electromagnetic (ANTEMN) , Montreal, QC, Canada, pp. 1-2, July 2016.

Abstract

On propose une nouvelle antenne à résonateur diélectrique hybride à gain élevé (HDRA) pour les systèmes de communication en ondes millimétriques fonctionnant dans la gamme de fréquence de 57-64 *GHz*. Un résonateur diélectrique (DR) annulaire est activé par une antenne de connexion à ouverture couplée pour obtenir des résonances multiples et pour élargir la bande de l'antenne. En vue d'augmenter le gain de l'antenne, l'antenne HDRA est entourée par une cavité métallique. En outre, la performance de ce diagramme de rayonnement est améliorée par l'utilisation des anneaux métalliques reliés à la terre. Les résultats de simulation montrent une bonne performance en ce qui concerne la largeur de bande, le gain et les diagrammes de rayonnement.

Abstract

A new high gain hybrid dielectric resonator antenna (HDRA) is proposed for millimeter-wave (mm-wave) communication systems operating in the frequency range of 57-64 *GHz*. A ring-shape dielectric resonator (DR) is excited by an aperture-coupled patch antenna to achieve multiple resonances and widen the antenna bandwidth. To enhance the antenna gain, the HDRA is surrounded with a metallic dented-cavity. In addition, the performance of its radiation pattern is improved by using grounded-metallic rings. The simulation results demonstrate a good performance in terms of bandwidths, gain, and radiation patterns.

2.1 Introduction

The unlicensed spectrum at 60 *GHz* with several *GHz* of bandwidth and line-of-sight propagation characteristic is suitable for handling high speed wireless communications, distance measurement, and automotive radar systems [1]. Due to high-propagation loss and the limited transmit power, efficient antennas that are high gain, wideband, and compatible with monolithic microwave integrated circuits (MMICs) are needed. Increasing the electrical size of an antenna by employing hybrid configuration is one of the gain enhancement techniques proposed so far [2, 3]. In [3], a cross dielectric resonator antenna (DRA) coupled with a microstrip patch antenna has been presented to obtain the overall gain of 9 *dB*. In [4] and [5] fencing and electromagnetic bandgap (EBG) approaches have been reported to increase the antenna gain. In particular, in [4], a circular metallic fence is used to improve the gain of a patch antenna to 12 *dB* at 31 *GHz*. However, higher gain is required to overcome the mm-wave propagation loss.

In this work, a new hybrid antenna consisting of a ring-shape DRA surrounded with a dented-cavity and grounded metallic-strips is proposed that can provide a gain of about 16.5 *dB* with a balanced radiation pattern, i. e., identical E- and H- plane patterns. The proposed configuration can be easily integrated with mm-wave transceivers. antenna design and simulation

2.2 Antenna Design and Simulation

Fig. 2.1 shows the geometry of the proposed HDRA. This antenna consists of a ring-shape DRA with permittivity of 10.2 and thickness of 0.635 *mm* which is excited by an aperture coupled circular patch resonator. In the design process, the aperture length L_3 and diameter of the patch D_1 are firstly set to have a resonance in the lower edge of the desired bandwidth. Then, the inner and outer radii of DRA are adjusted to have another resonance in its upper part. Indeed, utilizing multiple resonances allow to achieve a widebande matching.

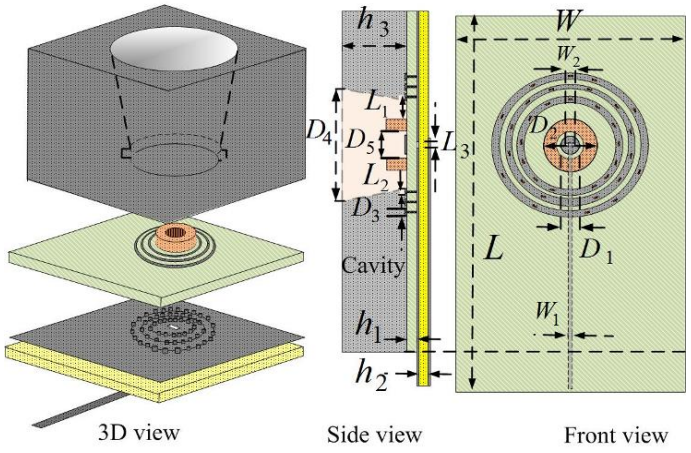

Figure 2.1 – Configuration of the proposed HDRA, h_1=$h2$=0.254, h_3=7, ϵ_r=2.95, ϵ_{r2}=ϵ_{r3}=10.2, D_1=1.26, D_2=7, D_3=0.6, D_4=7.5, D_5=2.3, L_1=2, L_2=0.2, L=45, W_1=0.24, W_2=0.75, and W=30 (all units are in mm).

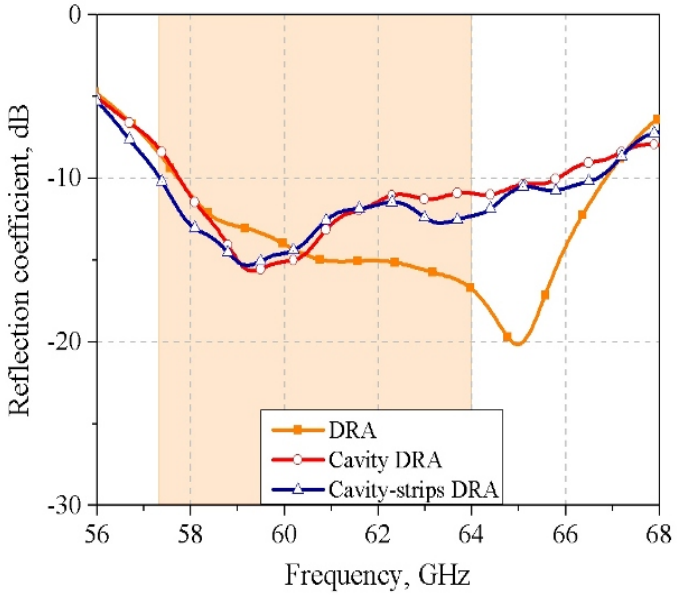

Figure 2.2 – Simulated reflection coefficient of the proposed HDRA compared to the ones without cavity and strips.

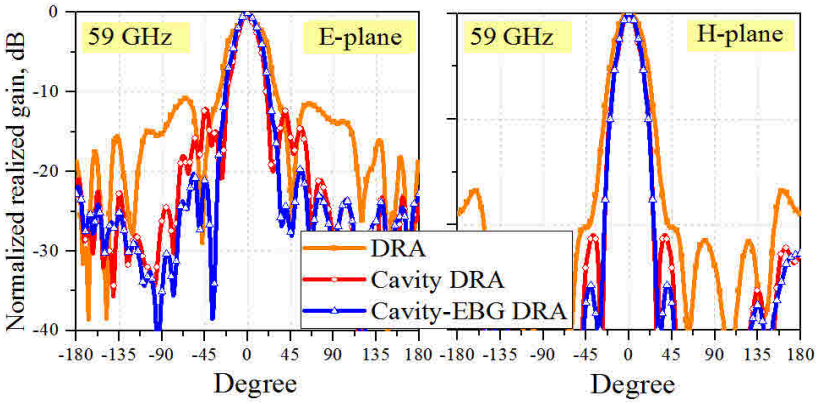

(a)

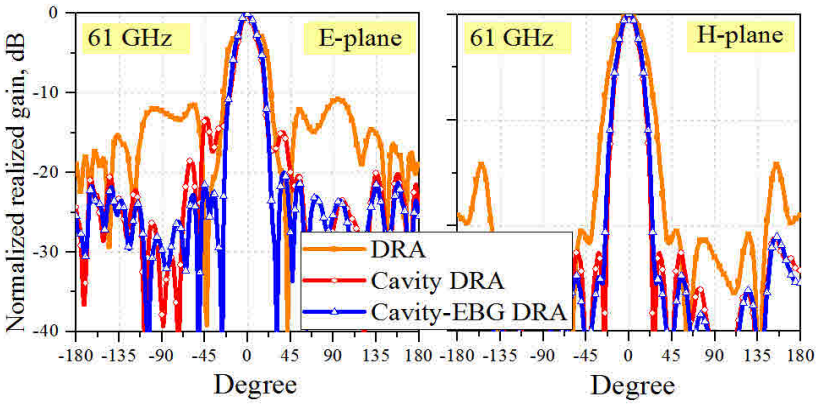

(b)

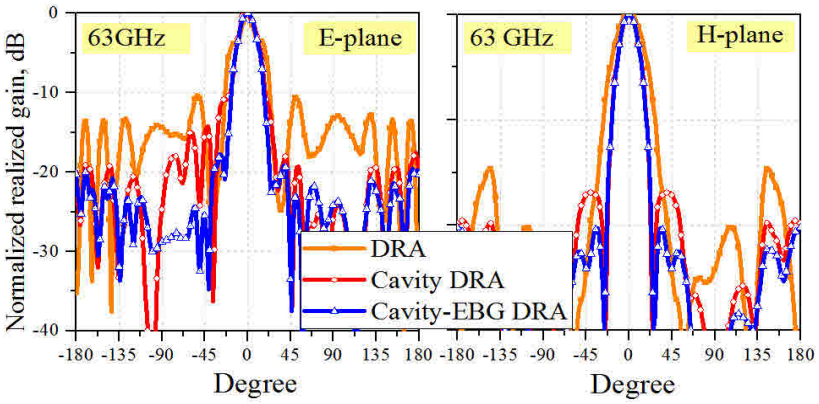

(c)

Figure 2.3 – Simulated radiation patterns of the proposed HDRA compared to the ones without cavity and strips.

To increase the gain and improve the radiation pattern shape of proposed HDRA, a conical dented-cavity is also used. The height and inner radii of the cavity are key parameters to control the gain and reflection coefficient responses of HDRA. In addition, three concentric grounded rings

are utilized to suppress the surface waves propagated in the substrate and hence improve the gain response and decrease the side lobe levels. Summarized in Fig. 2.1, dimensions of the proposed HDRA are optimized to cover the frequency range of 57-64 *GHz*, as seen in Fig. 2.2.

For the sake of comparison, the proposed antenna and the ones without cavity and strips are simulated with the transient solver of Microwave CST Studio. Fig. 2.2 shows that the dented-cavity and strips have negligible effect on the patch resonance frequency but they noticeably affect the matching response at higher region of the bandwidth, where DRA dominantly resonates. The effects of cavity and strips on the radiation patterns are studied in Fig. 2.3. It can be concluded that using cavity and strips considerably decreases the side lobe levels to less than -20 *dB* over the desired bandwidth and also provide balanced radiation patternswith -10 *dB* beam-widths of about 40 ° in the E- and H-planes.

The simulated realized gain of the HDRA shown in Fig. 2.4 demonstrates that the cavity increases the gain of DRA around 4 dB across the lower 4 *GHz* region of the desired bandwidth, while the strips mostly improves the gain response in the higher range of the bandwidth, resulting in a -1 *dB* gain bandwidth of 11% for the HDRA (i. e., almost a stable radiation pattern response).

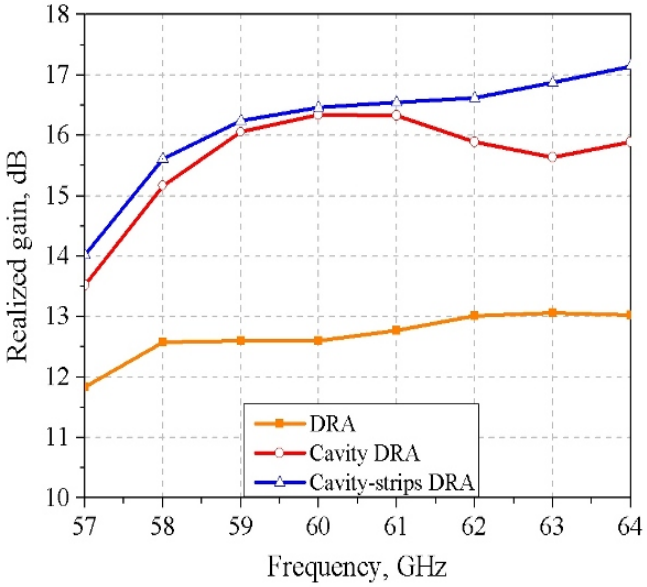

Figure 2.4 – Simulated realized gain of the proposed HDRA compared to the ones without cavity and strips.

2.3 Conclusion

A new hybrid mm-wave antenna consisting of a ring DRA, a dented-cavity, and grounded metallic strips has been presented. By optimally designing the hybrid antenna structure, a broad matching bandwidth of 12% (57-64 GHz) has been realized. In addition, the integration of cavity and metallic grounded strips with DRA enhance the antenna gain response to around 16.5 dB with -1 dB bandwidth of 11%. Furthermore, the HDRA has a balanced radiation pattern with -10 dB beam width of about 40 ° the E- and H-planes across the desired frequency range. The simulated results demonstrate that the proposed antenna is a good candidate for mm-wave applications, in particular as a feed for reflector or lens antennas.

Bibliographie

[1] T. S. Rappaport, J. Murdock, and F. Gutierrez, “State of the Art in 60-GHz Integrated Circuits and Systems for Wireless Communications,” *IEEE Proc.*, vol. 99, no. 8, pp. 1390–1436, Aug. 2011.

[2] A. Perron, T. A. Denidni, and A. Sebak, "High-Gain Hybrid Dielectric Resonator Antenna for Millimeter-Wave Applications: Design and Implementation," *IEEE Trans. Antennas Propag.*, vol. 57, no. 10, pp. 2882-2892, Oct. 2009.

[3] Nasimuddin, K. P. Esselle, "A Low-Profile Compact Microwave Antenna with High Gain and Wide Bandwidth," *IEEE Trans. Antennas Propag.*, vol. 55, no. 6, pp. 1880-1883, June 2007.

[4] A. Elboushi and A. Sebak, "High-Gain Hybrid Microstrip/Conical Horn Antenna for MM-Wave Applications," *IEEE Antennas Wireless Propag. Lett.*, vol. 11, pp.129-132, 2012.

[5] H. Boutayeb and T. A. Denidni, "Gain Enhancement of a Microstrip Patch Antenna Using a Cylindrical Electromagnetic Crystal Substrate," *IEEE Trans. Antennas Propag.*, vol. 55, no. 11, pp. 3140-3145, Nov. 2007.

Article 3

An Improved Performance Millimeter-Wave Antenna Array by Using Artificial Materials

E. Erfani and S. O. Tatu

IET Microwaves, Antennas and Propagation, Under review, July 2018.

Abstract

On présente un réseau d'antennes en ondes millimétriques, à 2×4 éléments intégrant une structure à surface souple. L'antenne proposée est alternativement interprétée comme un réseau d'antennes couples (EACPA), alimenté par un réseau d'amenée par une transition (SL-to-GCPW) à faible perte et à large bande. Il est démontré que, par rapport à un réseau planaire conventionnel à 4×4 éléments, ayant une certaine taille d'ouverture, on a besoin de huit éléments rayonnants pour obtenir presque la même directivité/le même gain, en utilisant la structure à surface souple entre les éléments du réseau. En réduisant le nombre d'éléments excités par cette méthode, on simplifie le réseau d'alimentation. En outre, du fait qu'elle est plus visible dans le plan E, où l'on utilise la structure à surface souple, le niveau du lobe latéral est meilleur dans les deux plans (E et H).

D'autres avantages de l'approche proposée sont les améliorations liées à l'adaptation d'impédance, directivité, gain et largeur de bande.

Abstract

A millimeter-wave 2×4-element antenna array integrated with a soft surface structure is presented. The proposed antenna is alternatively interpreted as an array of overlapped eared-aperture-coupled-patch-antenna (EACPA), fed by strip-line feed-network through a low loss and wideband strip-line-to-grounded-coplanar-waveguide (SL-to-GCPW) transition. It is shown that, compared to a 4×4-element conventional planar array with a given aperture size, eight radiating elements are required to achieve an almost same directivity/gain by utilizing the soft surface structure between elements of the array. By reducing the number of excited elements with this method, the feed-network is simplified. Furthermore, being more noticeable in the E-plane, where soft surface structure is used, the side lobe level is improved in both E- and H-planes. Enhancements of matching and directivity/gain bandwidths are other advantages achieved with the proposed approach.

3.1 Introduction

Demands on seamless high data rate communications with good quality of services have spurred 5^{th} generation (5G) of wireless technology to tackle the shortcomings of current systems [1]-[4]. Because of the vast available frequency range, millimeter-wave (mm-wave) technology has been considered as the favorite solution to address this high capacity requirement. Nonetheless, high propagation loss is one of the main obstacle in the mm-wave regime to establish a robust point-to-point wireless link. Considering the limited power delivered by transmitter, high gain antennas are needed to compensate the high propagation loss [3] and [4]. Depending on the demanded antenna gain dictated by the coverage requirement, horn, reflector, lens, and planar arrays can be used. Planar arrays seem to be the most appropriate solution because of their low costs, low profile structures, and flexibilities to integrate with RF-circuitry [4]. Microstrip patch antennas excited by vias or coupled slots are the most common elements used in mm-wave planar arrays [5]. Aperture coupled patch antennas (ACPA) are preferred because of avoiding vias and hence their undesired spurious radiations and inductive effects. Furthermore, by using this feeding approach, the radia-

ting layer, is separated from the feed layer. This gives enough design flexibilities to enhance the antenna bandwidth by selecting a thick substrate with a low dielectric constant. It also facilitates the integration of RF-circuitry with antenna. Although, with a trade between matching bandwidth and peak gain, the bandwidth can be improved by a few percent for a non-resonant-slot ACPA etched on a thick substrate with a dielectric constant in the range of 2-5, the propagation of surface and traveling leaky waves increases with this method [6]. This decreases the antenna efficiency by increasing the radiation losses, which is crucial for antenna arrays with complex feed-network designed for mm-wave applications.

The unique properties of electromagnetic band gap (EBG) and/or artificial magnetic conductor (AMC) given by high impedance surfaces (HIS) have made these structures attractive in improving the radiation performances of antennas mainly in terms of their bandwidth and gain [7]-[10], suppressing the propagation of surface waves on dielectric surfaces to reduce mutual coupling between elements of an array and improving scan coverage [11]-[17], increasing isolation between two closely spaced radiating elements/arrays [18], and designing low-profile antennas [7], [12], and [19]. In addition, as a kind of EBG structure with band gap response for the waves propagating in one direction, soft surface structures have also been used to increase the planar antenna gain and control the pattern shape [10], [20], and [21]. In all these works, antenna gain has been enhanced up to 5 dB by increasing the effective aperture area with EBG or soft surface structures. This has been achieved by capturing the propagating surface and radiating space waves and effectively transforming them into radiating waves. This method has also been used in the E-plane of arrays to enhance their gain [22] and [23]. When AMC and EBG properties of HIS are overlapped over the desired operating bandwidth, the utilized approach seems to be more effective by realizing a uniform aperture field phase distribution over the substrate surface. In this way, the artificial materials can also be placed very close to the radiating element [7], [9]-[12], and [19].

In this paper, the advantages of soft surfaces are deliberately exploited to improve the radiation performances of antenna arrays in terms of matching and directivity bandwidths, gain, and side lobe level. It is also shown that when elements of an array are interleaved with a soft surface structure, the required number of excited elements is decreased by two times, while still a directivity level almost equal to a conventional array with an equivalent aperture size is obtained. This is crucial in mm-wave applications to simplify the feed-network and the design complexity. As a proof of concept, an array of 2×4 aperture coupled patch (ACP) interleaved with a soft surface structure

is presented and its performance is compared with an equivalent conventional 4×4-element array. The radiation mechanism of this array is alternatively described based on its constructing radiating element named eared-aperture-coupled-patch-antenna (EACPA), and accordingly, the step-by-step design procedure of the proposed antenna array is presented. A strip-line-to-grounded-coplanar-waveguide transition is also designed to facilitate the antenna characterization with an end-launch connector and the measurement results are presented and discussed.

3.2 Antenna Array Design

Fig. 3.1 shows the geometry of the proposed antenna array. The antenna consists of an array of aperture-coupled-patch (ACP) elements interleaved with an artificial material (i. e., a soft surface structure), which are excited by a strip-line corporate-feed network. This antenna can be alternatively described as an array of 2×4 overlapped eared-aperture-coupled-patch antenna (EACPA) as depicted in. To uniformly excite the elements, an optimized T-junction power divider and some quarter-wavelength transformers are used to construct the feed-network. In addition, a strip-line-to-grounded-coplanar-waveguide (SL-to-GCPW) transition is employed to match the antenna input impedance to 50 Ω and facilitate its characterization by connecting to an end-launch mm-wave connector. The antenna is designed based on design rules of PCB fabrication technology. The step-by-step design procedure of the proposed antenna array and its transition are described in the following sub-sections.

3.2.1 EACPA Design and Its Radiation Mechanism

The proposed EACPA, as shown in Fig. 3.2, consists of a strip-line-fed aperture coupled patch (ACP) surrounded by a soft surface structure. The soft surface structure is constructed by three rows of shortened metallic strips, and it is shaped to improve the radiation performance of the element in terms of peak directivity and -10 *dB* matched input impedance bandwidth. In addition, the width of last strip is slightly modified to improve the radiation pattern side lobe level. The proposed EACPA element is optimized with Ansoft HFSS simulator.

The EACPA is simulated for the cases of with/without the soft surface structure and their results are compared with the ones of an array of 1×2-ACPA with element distance of $d_2 = 3.6\,mm$

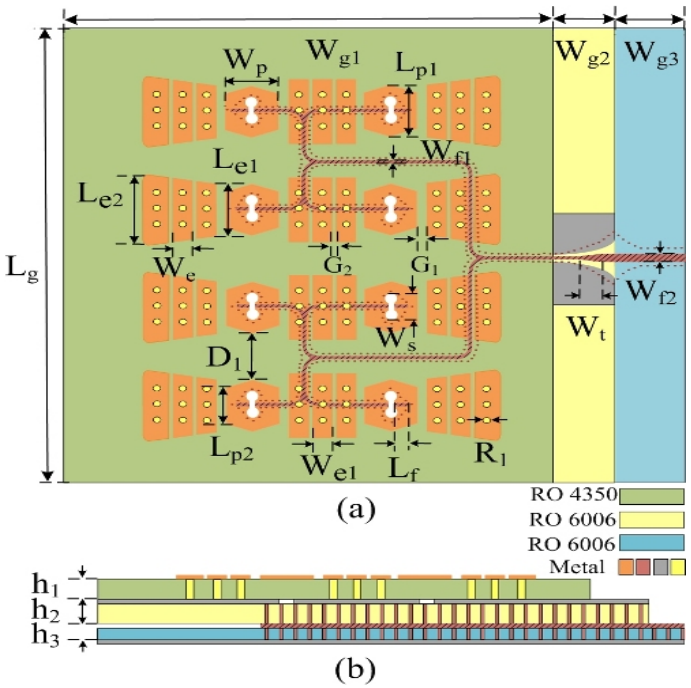

Figure 3.1 – Configuration of the proposed antenna, W_{g1}=14, W_{g2}=6, W_{g3}=4, L_g=16, W_p=1.05, L_{p1}=1.2, L_{p2}=0.9, W_{f1}=0.15, L_f=0.45, W_s=0.88, W_e=0.65, P_e=0.825, L_{e1}=2.3, L_{e2}=2.6, L_{e3}=2.45, R_1=0.1, G_1=0.175, G_2=0.125, D_1=2.4, W_t=0.5, W_{f2}=0.35, H_1=0.254, H_2=0.127, and H_3=0.254, (all units are in mm).

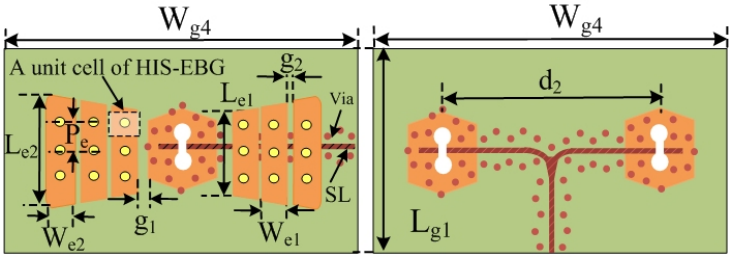

Figure 3.2 – Configuration of an eared-aperture-coupled-patch radiating element (left) and its equivalent 1×2-element conventional array (right): W_{g4}=9, L_{g1}=4.6, L_{e1}=2.3, L_{e2}=2.6, g_1=0.175, g_2=0.125, W_{e1}=0.65, W_{e2}=0.75, P_e=0.825, and d_2=3.6 (all units are in mm).

(it is equal to the center-to-center distance of the middle strips in the soft surface structure). The 1×2-element array is also excited with a T-junction strip-line power divider. To fairly justify their performances, especially in term of directivity, the substrate dimensions of all three designs are kept equal. Their reflection coefficient and directivity responses are compared in Figs. 3.3 and 3.4. The achieved results show that ACPA and two element linear array have matching bandwidths of 4.7 GHz (56.5-61.2 GHz) and 3.5 GHz (57-60.5 GHz), respectively, while the bandwidth of ACPA is improved to 5.9 GHz (57-62.9 GHz) when the soft surface structure is used. This intuitively can be described as the decrease of substrate effective dielectric constant by enforcing fringing electric

fields of the patch to be concentrated in the gap between its side edges and closest shortened strips in their vicinity (stored energy underneath of the patch is reduced, resulting in a smaller antenna Q factor). In addition, the antenna directivity is increased by 3.7 dB compared to the case without soft surface structure. As depicted in Fig. 3.5, this directivity enhancement is achieved without creating any side-lobe level in the radiation pattern of the EACPA.

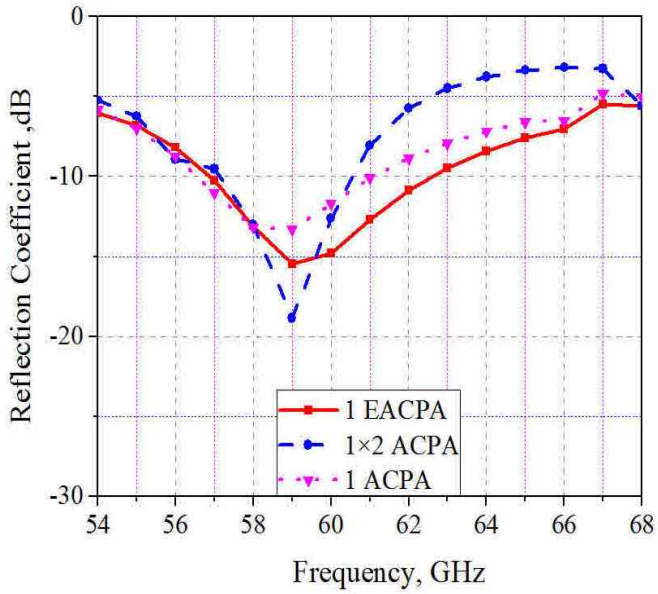

Figure 3.3 – Reflection coefficient response of the proposed EACPA compared to the case of without soft surface structure and an array of 1×2 ACPA.

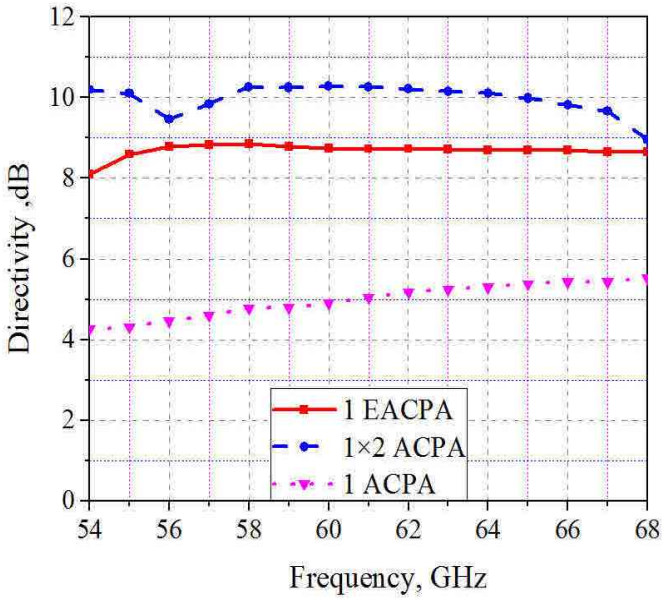

Figure 3.4 – Directivity response of the proposed EACPA compared to the cases of without soft surface structure and an array of 1×2 ACPA.

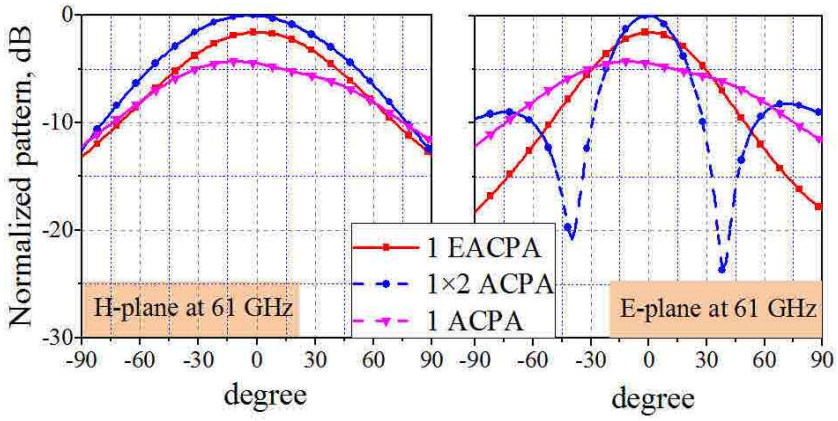

Figure 3.5 – E- and H-plane patterns of EACPA compared with an ACPA and an array of 1×2 ACPA.

To understand the radiation mechanism of the proposed EACPA, its near field patterns are demonstrated in Fig. 3.6. As it can be noticed, the propagating surface and coupled space waves are captured by the utilized soft surface structure in the E-plane, and they are constructively contributed into the radiated fields. Indeed, the captured fields increase the effective aperture of the radiating element, and therefore, it considerably increases the antenna gain. To justify the operating mechanism of the soft surface structure, the transmission coefficient of a matched transmission line passing over seven rows of utilized shortened strips and the reflection phase response of one of its unit cells (as illustrated in Fig. 3.2) are simulated and the results are shown in Fig. 3.7. As it can be seen, when soft surface material is used underneath of the transmission line, a frequency band gap is effectively created over the desired band, where it also operates as an AMC structure according to the reflection phase response of its unit cell [12]. As shown in Fig. 3.7, this agrees with the dispersion diagram calculated for Γ-X direction of the unit cell Brillouin-zone, predicting a band gap from 56.9 GHz to 72.4 GHz [7], [10], and [12].

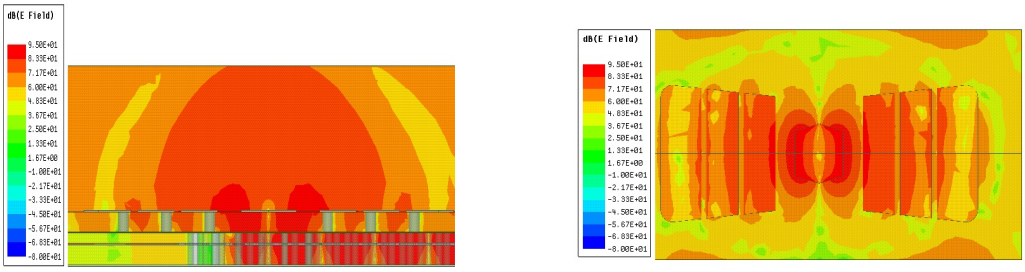

(a) Top view (b) Side view

Figure 3.6 – Radiated near field pattern of the proposed EACPA simulated at 61 *GHz*.

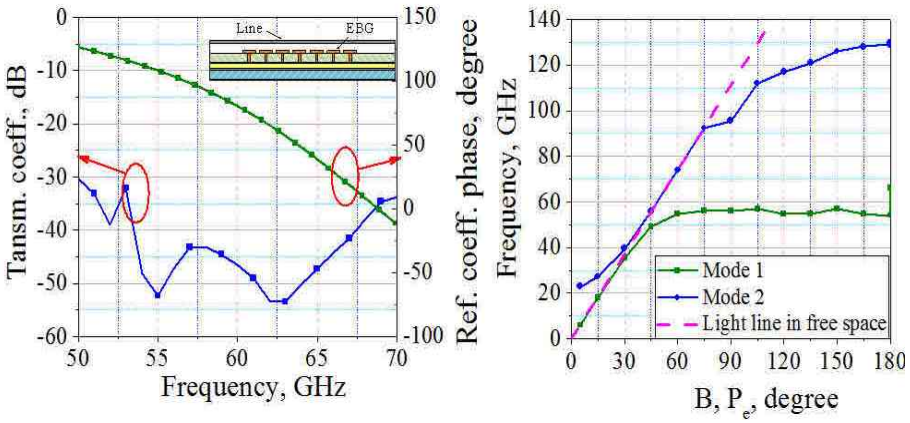

Figure 3.7 – Performance of soft surface in response to propagating surface and normal-incident waves, simulated transmission coefficient response of a matched transmission line passed over seven rows of soft surface structure and reflection phase response of a unit cell of the utilized soft surface structure (left side), dispersion diagram calculated for Γ-X direction of the unit cell Brillouin-zone (right side).

3.2.2 Array Design and Its Simulation Results

The optimized EACPA is used to design the proposed array shown in Fig. 3.1. First, two EACPA are combined and the lengths of overlapped shortened strips in the middle are equalized as L_{e3}=(L_{e1}+L_{e2})÷2. Then, two of the overlapped EACPA are cascaded to construct a 2×2-element sub-array (Fig. 3.8, top right). The sub-array and its feed-network are optimized in terms of maximum bandwidth, peak directivity, and minimum side lobe level. In the next step, the optimized 2×2-element sub-array is used to design the 2×4-element array (Fig. 3.8, bottom right). To compare the performance of designed sub-array and array with their equivalent planar arrays without any soft surface structure, 2×4- and 4×4-ACPA antenna arrays with element distance of 3.6 mm) are also simulated (Fig. 3.8, left). To fairly compare the results, all four arrays have equal aperture sizes. It needs to highlight that the number of excited elements in arrays with the soft surface structure is half of the conventional arrays. This simplifies the feed network of equivalent 4×4-ACPA array antenna by reducing the total number of T-junctions and eliminating the bottom $\frac{1}{4}$ microstrip power divider. The presented simulation results in this section does not include the SL-to-GCPW transition.

The simulated reflection coefficient responses of designed arrays, as shown in Fig. 3.9, demonstrate that when ACPAs are integrated with soft surface structure, the antenna array bandwidth is considerably improved. This is more pronounced when the array gets larger. It has been proved that

EBG and soft surface structures reduce the mutual coupling between two closely spaced radiating patches [7, 14], and this improves the impedance bandwidth [8, 20].

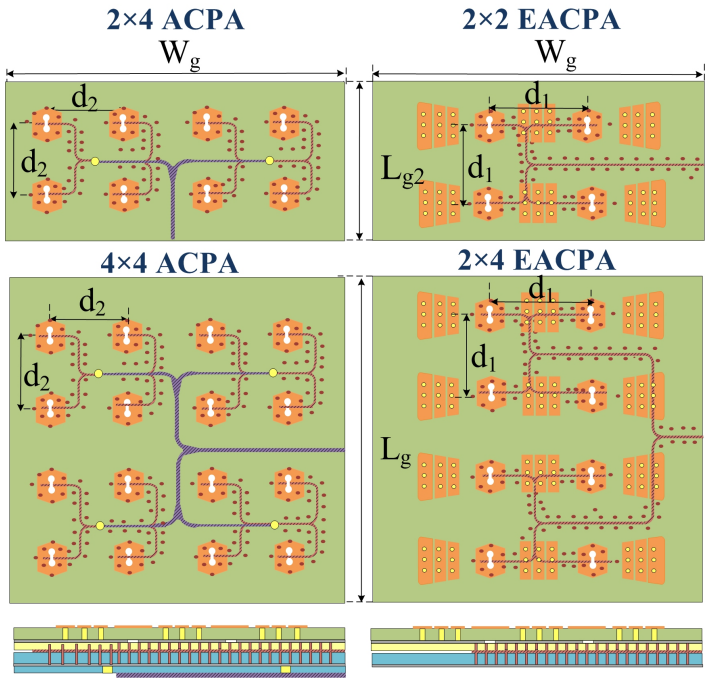

Figure 3.8 – Configurations of the designed arrays, sub-array of 2×4 ACPA and 4×4 ACPA array (left); sub-array of 2×2 EACPA and 2×4 EACPA array (right), d_1**=**d_2**=3.6,** W_g**=14,** L_g**=16, and** L_{g2}**=8** *mm*.

The simulated radiation pattern directivity of these four arrays are compared in Fig. 3.10. The results demonstrate that the directivity of antennas integrated with the soft surface structure follow their equivalent arrays without artificial materials. This shows that soft surface structures can be used to decrease the complexity of feeding network by reducing the number of excited elements by two times, while almost similar peak directivity/gain level is obtained. In addition, by interleaving array elements with these structures, the array directivity is improved by about 2 *dB* at higher frequencies compared to its equivalent 4×4-element array. Indeed, the -3 *dB* directivity bandwidths of proposed array and its equivalent antenna are >13 *GHz* and 10.3 *GHz*, respectively.

Furthermore, when soft surface structures are used, the pattern side lobe levels are decreased in both E- and H-planes over the desired bandwidth by at least 9 *dB* and 2 *dB*, respectively. This is more noticeable in the E-plane because of effective interaction with the captured propagating-surface and radiated-space waves. To demonstrate the side lobe level enhancement, radiation patterns of arrays are only shown at 61 *GHz* in Fig. 3.11 due to the space paucity. The achieved results prove that the proposed structure outperforms its equivalent to conventional arrays, i. e., arrays with the

same aperture area without any soft surface structure, in terms of directivity, bandwidth, and side lobe level performances. The electrical performances of simulated arrays are summarized in Table 3.1.

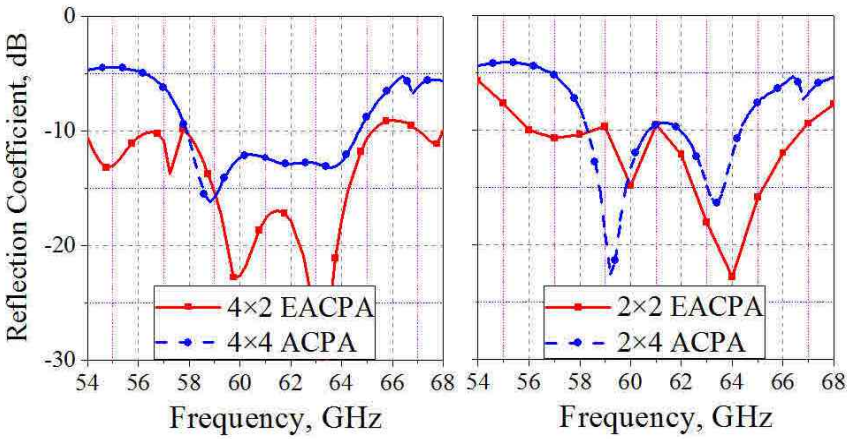

Figure 3.9 – Reflection coefficient responses of the designed arrays: 2×2 EACPA array compared with 2×4 ACPA array (left); 2×4 EACPA array compared with 4×4 ACPA array (right).

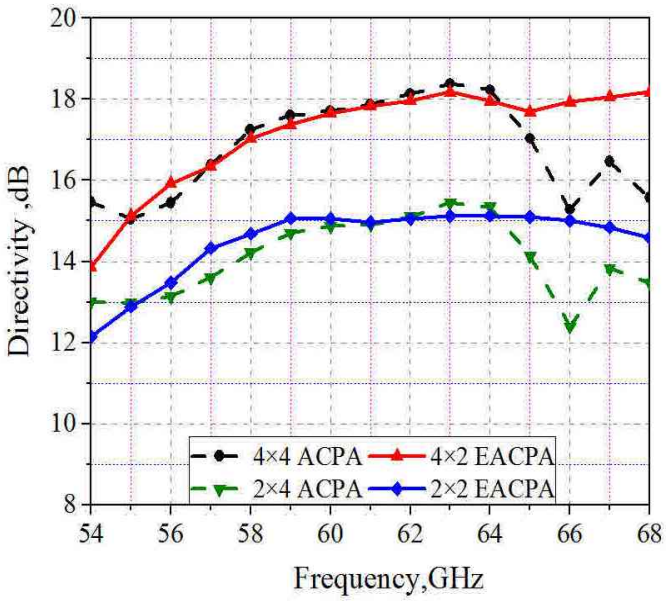

Figure 3.10 – Directivity responses of the designed arrays: 2×2 EACPA array compared with 2×4 ACPA array and 2×4 EACPA array compared with 4×4 ACPA array.

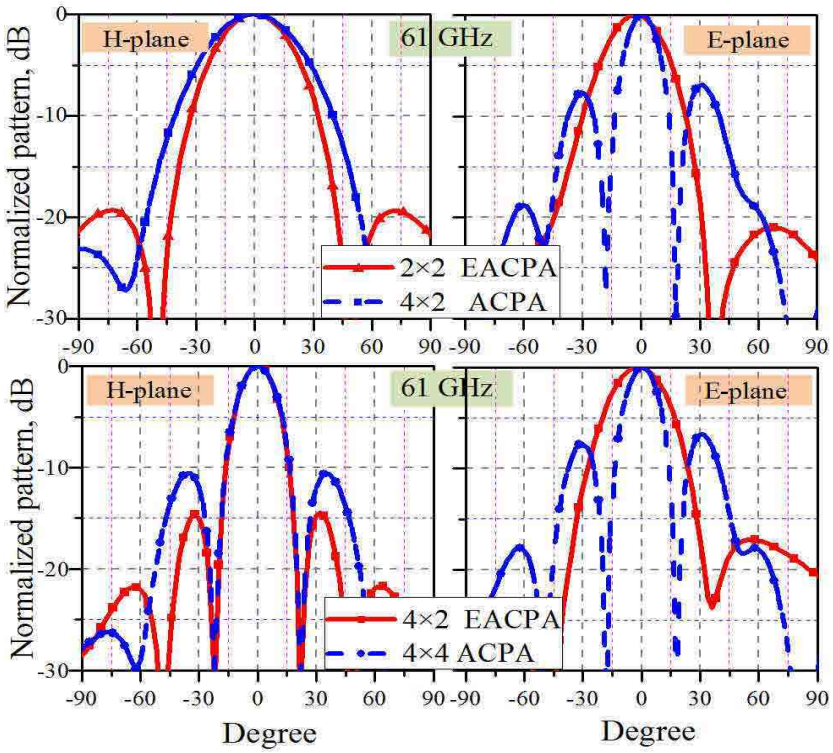

Figure 3.11 – Normalized radiation patterns of the designed arrays: 2×2 EACPA array compared with 2×4 ACPA array, and 2×4 EACPA array compared with 4×4 ACPA array.

Tableau 3.1 – Radiation characteristics of designed antenna arrays.

		2×2 EACPA		2×4 ACPA		2×4 EACPA		4×4 ACPA	
Matching BW (*GHz*)		56-67		58.3-64.4		54-68		58-64.8	
-1 *dB* directivity BW (*GHz*)		56.7-68.5		58-64.8		58.2-68		58.3-64.7	
Peak gain (*dB*)		14.24		14.47		17.3		17	
		E	H	E	H	E	H	E	H
SLL(*dB*)	58 *GHz*	-18	-21	-9	-19	-19	-13.2	-9	-11.4
	61 *GHz*	-21	-19	-7	-23	-17	-14	-7.8	-10.6
	64 *GHz*	-27	-17	-10	-21	-22	-13.8	-10	-10
Gain at 61 *GHz* (*dB*)		14		13.9		17		16.76	

3.3 Transition Design

To facilitate antenna characterization, a wideband low loss SL-to-GCPW is designed and integrated with the designed antenna array. To minimize the reflection and transmission coefficient responses, the transition at the junction of strip line to GCPW is tapered. Because of the fabrication constraints, two rows of vias are used to shield the transmission lines in this design. Fig. 3.12 demonstrates the proposed transition and its optimized dimensions. As depicted in Fig. 3.13, the designed transition is well matched and its transition loss is less than 0.6 *dB* over the desired bandwidth. In addition, not shown here for brevity, it does not degrade the radiation pattern of proposed antenna array when it is integrated with it.

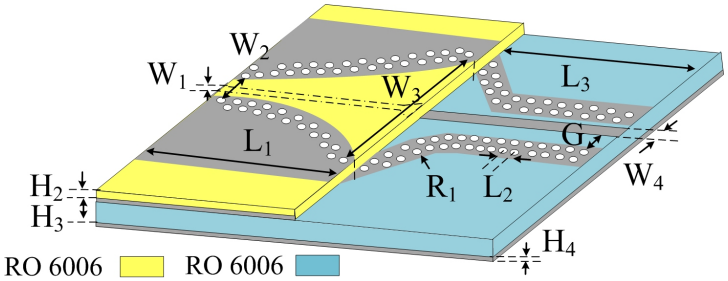

Figure 3.12 – Geometry of proposed SL-to-GCPW transition. W_1=0.15,W_2=0.17, W_3=4.7, W_4=0.35, L_1=6, L_2=0.5, L_3=4, G=0.4, R_1=0.1, H_2=0.127, H_3=0.254,and H_4=0.017 (all units are in *mm*).

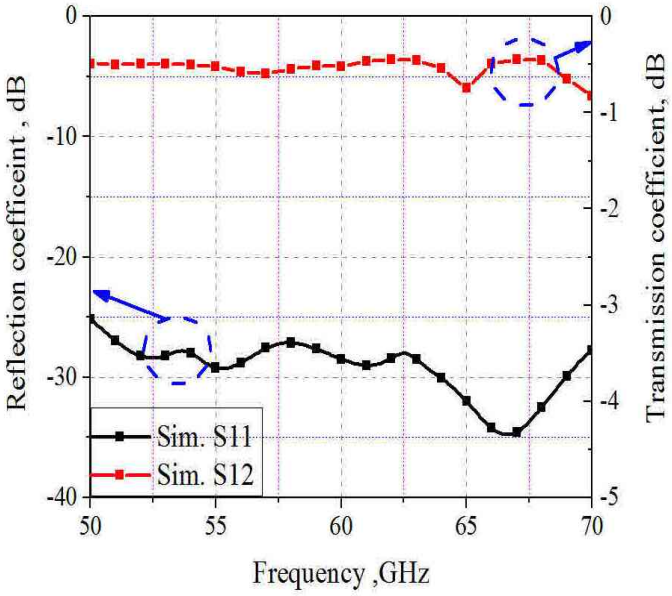

Figure 3.13 – Scattering parameters of the proposed SL-to-GCPW transition.

3.4 Fabrication and Measurement Results

Each antenna layer is individually etched with photo lithography technique on a piece of Rogers substrate, while their vias have been metalized. Then, three layers are glued with heat and pressure. Fig. 3.14 shows the photo of fabricated antenna array and its transition connected to an end-launch connector. The antenna was experimentally characterized and its results are compared with the simulated ones as summarized in Table 3.1. The simulations in this section include the transition and end-launch connector effects.

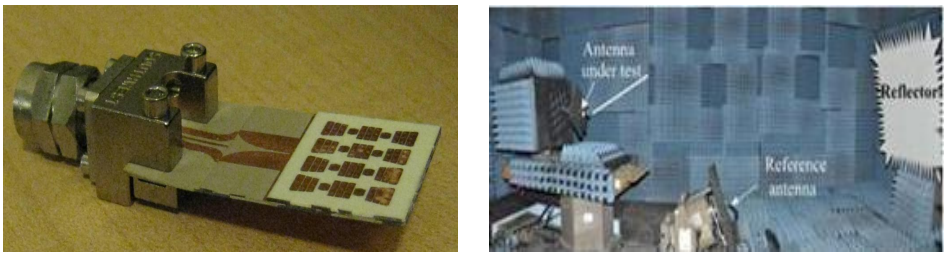

(a) (b)

Figure 3.14 – Photos of fabricated proposed antenna array and its measurement setup.

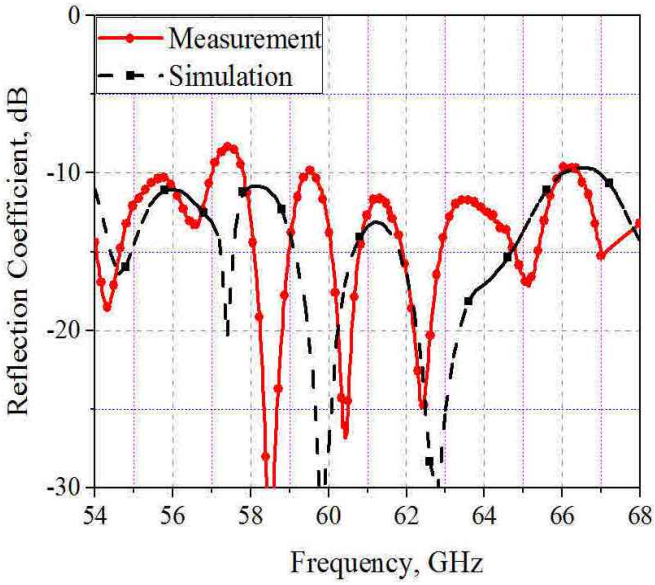

Figure 3.15 – Simulated and measured reflection coefficient responses of the proposed antenna array.

Being in good agreement with the simulate one, the measured reflection coefficient of the antenna is depicted in Fig. 3.15. The results show that, by neglecting a slightly impedance mismatch around 57.3 *GHz*, the matching bandwidth of the proposed antenna is at least 1.76 times larger (>12 *GHz*)

than its equivalent 4×4-element conventional array antenna (6.8 *GHz*). The radiation patterns of the proposed antenna were measured in an anechoic chamber and are shown in Fig. 3.16. Confirming the simulated ones, there are some degradations in the pattern shape and side lobe level that might be because of the fabrication tolerances and measurement set-up misalignment. To further substantiate the performance of proposed antenna, its realized gain was also measured and, as demonstrated in Fig. 3.17, it agrees well with the simulated one. The above-mentioned uncertainties are the reason of slightly deviation of measured realized gain from the simulated curve.

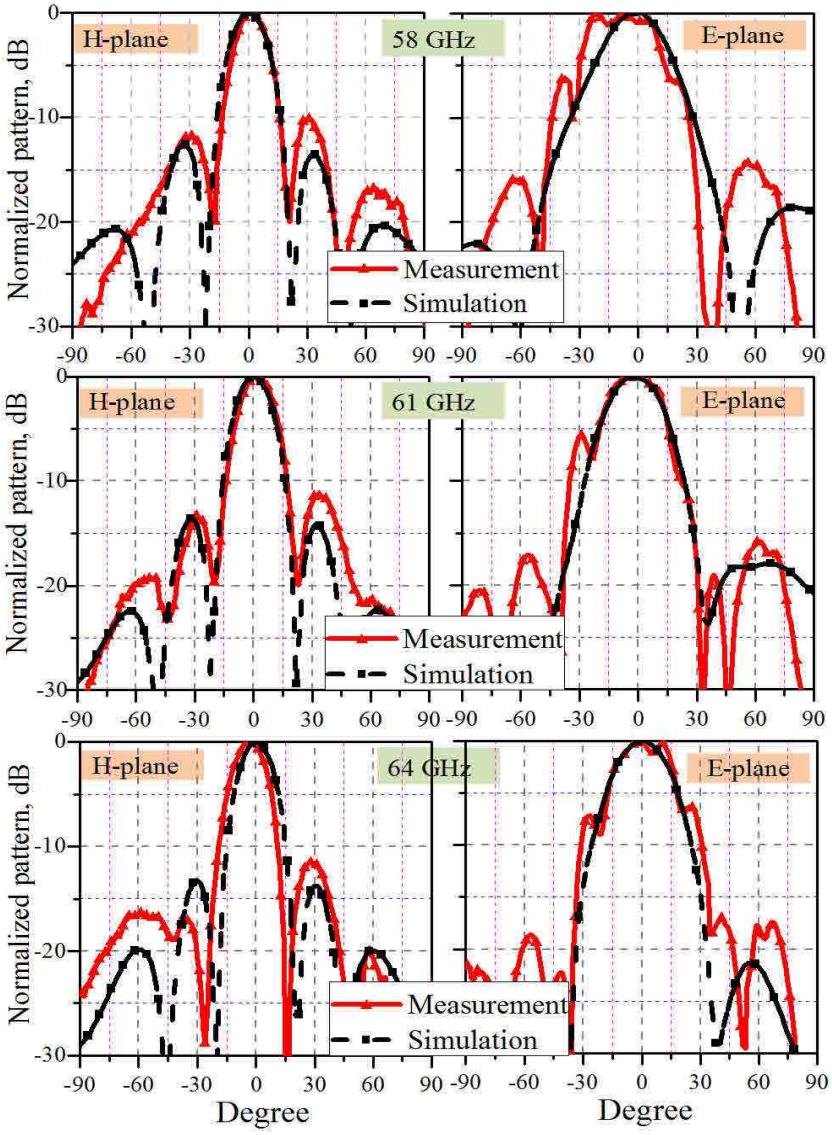

Figure 3.16 – Simulated and measured radiation patterns of the proposed antenna array.

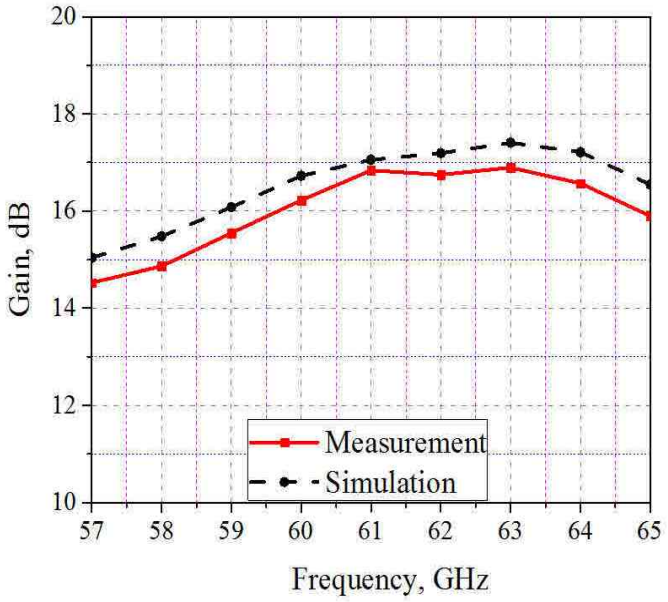

Figure 3.17 – Simulated and measured realized gains of the proposed antenna array.

3.5 Conclusion

Application of artificial materials to effectively improve the antenna array performances in terms of bandwidth, side lobe level, and feed-network thinning is investigated. It was shown that by interleaving array elements with appropriate artificial materials, the number of excited elements in an array can be reduced by two times without scarifying the antenna gain. This results in a simpler feed-network and larger directivity/gain bandwidth. Indeed, this is achieved by controlling the propagating surface and radiating space waves over the antenna substrate. Furthermore, it was demonstrated that the utilized artificial materials improve the pattern side lobe level, especially in the E-plane by at least 9 dB. The antenna matched bandwidth for the antenna array was also improved to>12 GHz, which is considerably larger than the one of its equivalent conventional 4/$times$4-element antenna array (which is 6.8 GHz).

Bibliographie

[1] T. S. Rappaport S. Sun, R. Mayzus, H. Zhao,Y. Azar, K. Wang, G. N. Wong, J. K. Schulz, M. Samimi, and F. Gutierrez.,"Millimeter wave mobile communications for 5G cellular: it will work!," *IEEE Access*, vol. 1, pp. 335-349, May 2013.

[2] J. Qiao, X. S. Shen, J. W. Mark, Q. Shen, Y. He, and L. Lei, "Enabling device-to-device communications in millimeter-wave 5G cellular networks," *IEEE Comun. Mag.*, vol. 53, no. 1, pp. 209-215, Jan. 2015.

[3] P. Wang, Y. Li, L. Song, and B. Vucetic, "Multi-gigabit millimeter wave wireless communications for 5G: from fixed access to cellular networks," *IEEE Comun. Mag.*, vol. 53, no. 1, pp. 168-178, Jan. 2015.

[4] Roh, J. Y. Seol, J. Park, B. Lee, J. Lee, Y. Kim, J. Cho, K. Cheun, and F. Aryanfar, "Millimeter-wave beamforming as an enabling technology for 5G cellular communications: theoretical feasibility and prototype results," *IEEE Com. Mag.*, vol. 52, no. 2, pp. 106-113, Feb. 2014.

[5] P. Bhartia, I. Bahl, R. Garg, and A. Ittipiboon, "Microstrip antenna design handbook" (Artech House, MA, USA, 2001)

[6] C. C. Liu, A. Hessel, and J. Shmoys, "Performance of probe-fed microstrip-patch element phased arrays," *IEEE Trans. Antenna Propag.*, vol. 36, no. 11, pp. 1501-1509, Nov. 1988.

[7] D. Sievenpiper, L. Zhang, R. F. J. Broas, N. G. Alexopolous, and E. Yablonovitch, "High-impedance electromagnetic surfaces with a forbidden frequency band," *IEEE Trans. Mic. Theory. Tech.*, vol. 47, no. 11, pp. 2059-2074, Nov. 1999

[8] N. Llombart, A. Neto, G. Gerini, and P. De Maagt, "Bandwidth, efficiency and directivity enhancement of printed antenna performance using planar circularly symmetric EBGs," *Eur. Conf. Mic.*, 2005.

[9] A. Foroozesh, L. Shafai, "Investigation into the application of artificial magnetic conductors to bandwidth broadening, gain enhancement and beam shaping of low profile and conventional monopole antennas," *IEEE Trans. Antenna. Propag.*, vol. 59, no. 1, pp. 4-20, Jan. 2011.

[10] M. NirooJazi, T. A. Denidni, M. R. Chaharmir, and A. R. Sebak, "Meta-surfaces and antennas' radiation characteristics enhancement: planar microstrip and microstrip-based quasi-aperture antennas," *IET Mic. Antenna Propag.*, vol. 8, no. 12, pp. 901-911, Sept. 16 2014.

[11] L. Yang, M. Fan, F. Chen, J. She, and Z. Feng, "A novel compact electromagnetic-bandgap (EBG) structure and its applications for microwave circuits," *IEEE Trans. Mic. Theory Tech.*, vol. 53, no. 1, pp. 183-190, Jan. 2005.

[12] G. Goussetis, A. P. Feresidis, and J. C. Vardaxoglou, "Tailoring the AMC and EBG characteristics of periodic metallic arrays printed on grounded dielectric substrate," *IEEE Trans. Antenna Propag.*, vo. 54, no. 1, pp. 82–89, Jan. 2006.

[13] A. E. I. Lamminen, A. R. Vimpari, and J. Saily, "UC-EBG on LTCC for 60-GHz frequency band antenna applications," *IEEE Trans. Antenna Propag.*, vol. 57, no. 10, pp. 2904-2912, Oct. 2009.

[14] F.Yang and Y. Rahmat-Samii,"Microstrip antennas integrated with electromagnetic band-gap (EBG) structures: a low mutual coupling design for array applications," *IEEE Trans. Antenna Propag.*, vol 51, no. 10, pp. 2936–2946, Oct. 2003.

[15] Y. Fu and N. Yuan, "Elimination of scan blindness in phased array of microstrip patches using electromagnetic bandgap materials," *IEEE Antenna Wirelss Propag. Lett.*, vol. 3, pp. 63-65, 2004.

[16] Z. Iluz, R. Shavit, and R. Bauer, "Microstrip antenna phased array with electromagnetic bandgap substrate," *IEEE Trans. Antenna Propag.*, vol. 52, no. 6, pp. 1446-1453, June 2004.

[17] M. Li, S. Q. Xiao, and B. Z. Wang, "Investigation of using high Impedance surfaces for wide-angle scanning arrays," *IEEE Trans. Antenna Propag.*, vol. 63, no. 7, pp. 2895-2901, Jul. 2015.

[18] M. Niroo-Jazi, T. A. Denidni, M. R. Chaharmir, and A. R. Sebak, "A hybrid isolator to reduce electromagnetic interactions between Tx/Rx antennas," *IEEE Antenna Wirelss Propag. Lett.*, vol. 13, pp. 75-78, Dec. 2014.

[19] A. Vallecchi, J. R. De Luis, F. Capolino, and F. De Flaviis, "Low profile fully planar folded dipole antenna on a high impedance surface," *IEEE Trans. Antenna Propag.*, vol. 60, no. 1, pp. 51-62, Jan. 2012.

[20] L. Wang, Y. X. Guo, and W. X. Sheng, "Wideband high-gain 60-GHz LTCC L-probe patch antenna array with a soft surface," *IEEE Trans. Antenna Propag.*, vol. 61, no. 4, pp. 1802-1809, Ap. 2013.

[21] H. Jin, W. Che, K. S. Chin, G. Shen, W. Yang, and Q. Xue, "60-GHz LTCC differential-fed patch antenna array with high gain by using soft-surface structures," *IEEE Trans. Antenna Propag.*, vol. 65, no. 1, pp. 206-216, Jan. 2017.

[22] L. Li, X. j. Dang, B. Li, and C. h. Liang, "Analysis and design of waveguide slot antenna array integrated with electromagnetic band-gap structures,"*IEEE Antenna Wirelss Propag. Lett.*, vol. 5, pp. 111-115, Ap. 2006.

[23] W. E. McKinzie, D. M. Nair, B. A. Thrasher, M. A. Smith, E. D. Hughes, and J. M. Parisi, "60-GHz 2×2 LTCC patch antenna array with an integrated EBG structure for gain enhancement,"*IEEE Antenna Wirelss Propag. Lett.*, vol. 15, pp. 1522-1525, Jan. 2016.

Article 4

A Millimeter-Wave Transmitarray Antenna

E. Erfani, M. Niroo-Jazi, S. Safavi-Naeini, and S. O. Tatu

International Symposium on Antenna Technology and Applied Electromagnetic (ANTEMN) , Montreal, QC, Canada, pp. 1-2, July 2016.

Abstract

Une antenne à réseau d'émission (TA) à large bande et à gain élevé, fonctionnant à 60 GHz, est proposée. Comme élément constitutif d'une antenne TA, une cellule unitaire (UC) multicouche est conçue de manière optimale pour obtenir une réponse en phase de transmission linéaire, ayant une plage de variation de 270 ° et une perte de transmission inférieure à -3 dB, sur toute la bande de fréquence désirée, de 58 GHz à 64 GHz. En outre, pour l'alimentation de l'antenne TA proposée, on utilise une antenne slot à ouverture exponentielle (ATSA). Les résultats de simulation obtenus montrent une adaptation large bande et un gain en largeur de bande à -1 dB de 16%, respectivement de 13%.

Abstract

A broadband and high gain transmitarray (TA) antenna, operating at 60 *GHz*, is presented. As a constituent part of the TA, a multi-layer unit cell (UC) is optimally designed to realize a linear transmission phase response with a continuous variation range of at least 270 ° and a transmission loss less than -3 *dB* across the desired frequency range from 58 GHz to 64 *GHz*. Furthermore, an antipodal exponential taper slot antenna (ATSA) is utilized to feed the proposed TA. The achieved simulation results demonstrate broad matching and -1 *dB* gain bandwidths of 16% and 13%, respectively.

4.1 Introduction

The intensive amount of available spectrum at millimeter-wave (mm-wave) frequencies has recently drawn increased attention of cellular service providers in leveraging this underutilized band as a worthy candidate for 5^{th} generation (5G) cellular systems [1, 2]. In the 5G scenario, a wideband and high-gain antenna is required to tackle the concerns of high propagation loss and non-light-of-sight issues in mm-wave frequencies. Horn and dielectric lens antennas are some of traditional approaches, but they are rather bulky and heavy [1]. As an alternative, planar antenna arrays, such as the one chosen in [4], are usually the preferred choice, but they suffer from excessive transmission line losses when designed for mm-wave frequencies. Among the other approaches which are operating based on spatial feeding technique, transmitarray (TA) antennas demonstrate high efficiency and broadband performances [5]. In a TA antenna, the waves emanated from the feed are collimated by adjusting the phase delays of its unit cells (UCs). It appears that because of the advantages offered by planar structures and spatial feeding approach, these antennas hold more promises for mm-wave frequencies [6].

To address the demands of mm-wave cellular networks, this work demonstrates a broadband and high gain shaped beam TA antenna. A unit cell based on receive/transmit approach with continuous phase variation (270 °) is optimally designed to realize the required transmission coefficient response of the TA antenna. Based on the realized phase variation range of the proposed UC and the radiation pattern of the optimized antipodal taper slot antenna (ATSA), as its feed, a TA antenna with an aperture size of $15.6\lambda_0 \times 15.6\lambda_0 \times 0.27\lambda_0$ is simulated and the results are presented in this work.

4.2 Transmittarray Antenna Design

The configuration of a TA antenna is shown in Fig. 4.1. It consists of a planar square surface with side length dimension d and substrate thickness T, which is centrally illuminated by a ATSA antenna placed at the focal distance F, far from the surface. This surface consists of a 26×26 array of band-pass FSS unit cells with the dimension of $2.6mm \times 2.6mm \times 1.35mm$. Each UC is composed of two square patches in one side, working as receiving antennas, which are coupled to the other two transmitting patches through a resonant aperture etched on the common ground plane. Indeed, by exciting multiple coupled resonances, a low loss band-pass filter with broadband transmission response is created. In addition, to maintain this desired performance for entire elements of the TA, the dimensions of UC are optimized for four different regions and curve fitting approach is used to extract a nonlinear relation between the varied sizes in each section.

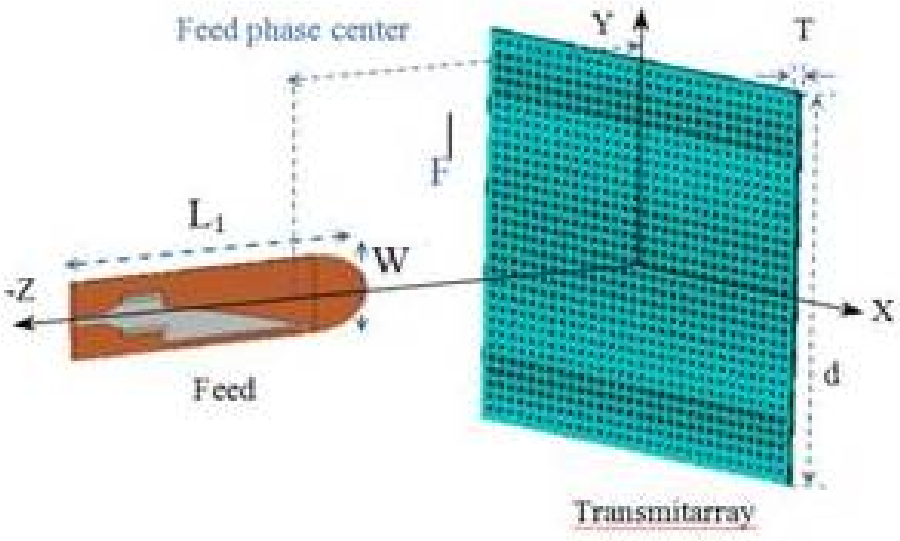

Figure 4.1 – Configuration of center feed TA antenna, d_1=78, L_1=35, W=7, and F=100 (all units are in mm).

To investigate the scattering performance of the UC, the frequency domain solver of Microwave CST Studio was used. The reflection and transmission coefficient responses for normal incident x- and y-polarized waves are shown in Fig. 4.2. It can be found that the low-loss transmission bandwidth of 39 GHz, as seen in Fig. 4.3, is large enough to realize a phase variation range of at least 270 ° across the TA aperture within the frequency range of 58-64 GHz, when the filter response is detuned by changing its dimensions.

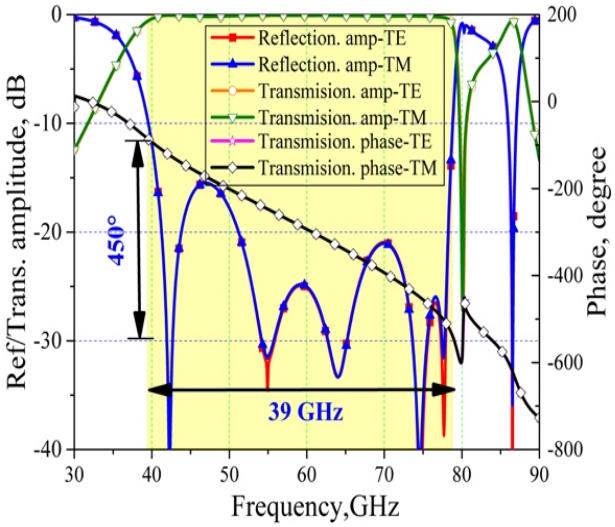

Figure 4.2 – Transmission and reflection coefficient responses of the proposed TA element.

In order to have a broadband and highly efficient TA antenna, a wide-band and stable radiation pattern feed with low cross polarization and side lobe levels is ideally desired. In this work, a planar ATSA with a broadband SIW feeding structure is chosen to illuminate the TA. As another critical parameter that should be considered, it is the phase center location of the ATSA, where the electromagnetic radiation spreads spherically. To avoid spatial phase error in the design of TA, a balanced-pattern feed with unique and stable phase center location in the E- and H-plane is required. All parameters of ATSA are optimized for center frequency of 61 *GHz* with CST Microwave Studio.

The TA with aperture size of d=15.6 λ_0=78 mm and F/d=1.25 is centrally illuminated by a ATSA antenna as the phase center of the feed is located at the focal point of the TA. The F/d=1.25 is chosen to match -10 dB radiation pattern beam-width of the ATSA antenna to the TA aperture. The phase distribution of each unit cell across the TA is calculated to collimate the radiation pattern of feed only in the E-plane. The entire TA antenna is simulated with transient solver of CST Microwave Studio. The simulated results for the radiation pattern of feed and TA antenna are illustrated in Fig. 4.3. These results confirm the collimation mechanism of the TA in the E-plane across the desired frequency band of 58-64 *GHz*. The simulated realized gain of TA is also compared to its feed as shown in Fig. 4.4. The 1 dB gain bandwidth of TA is 13%.

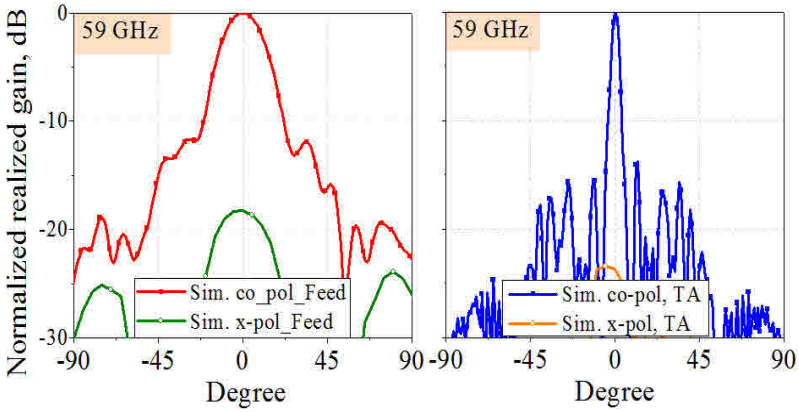

(a)

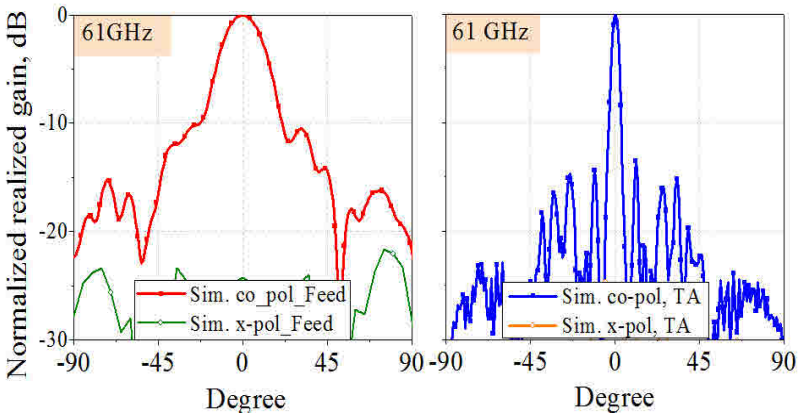

(b)

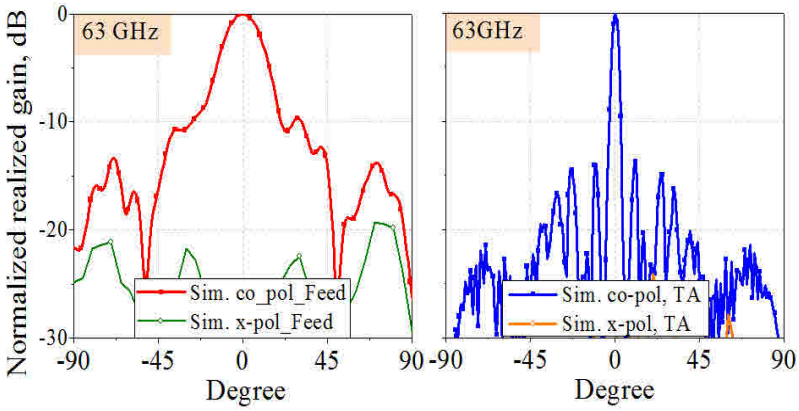

(c)

Figure 4.3 – Simulated radiation patterns of TA and its feed in E-plane. .

4.3 Conclusion

The potential of receiving/transmitting FSS unit cell for mm-wave TA antenna is investigated in this work. It is demonstrated that by optimally designing the UC and utilizing a curve fitting

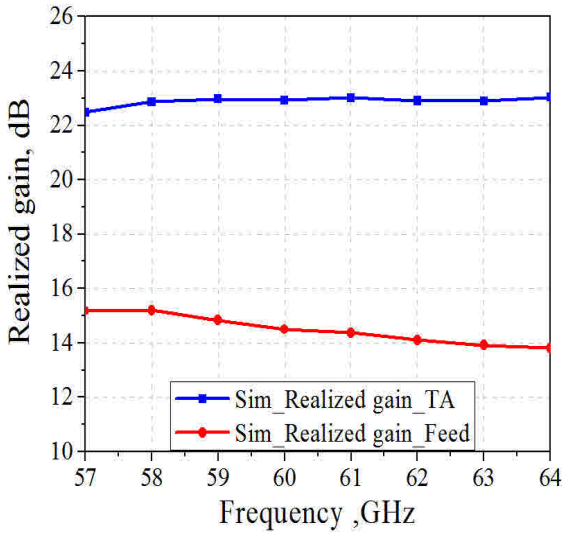

Figure 4.4 – Simulated realized gains of the TAantenna compared with its feed.

approach across different frequency regions, a low loss and linear phase response with minimum 270 ° continuous variation range can be realized for this UC. It is also shown that this unit cell can be used to design a broadband and high gain shaped beam transmitarray antenna. Indeed, by appropriately selecting a feed antenna and precisely designing the TA, high gain and broadband radiation pattern performances with low side lobe level (less than -15 dB) can be realized.

Bibliographie

[1] T. S. Rappaport, S. Sun, R. Mayzus,Z. Hang, Y. Azar, K. Wang, G. N. Wong, J. K. Schulz., M. Samimi, and F. Gutierrez, "Millimeter Wave Mobile Communications for 5G Cellular: It Will Work!,"*IEEE Access*, vol. 1, pp. 335-349, 2013.

[2] C. Dehos, J. L. Gonzalez, A. Domenico, D. Ktenas, and L. Dussopt, "Millimeter-wave Access and Backhauling," *IEEE Mag. Commun.* , vol. 52, no. 9, pp. 88-95, 2014.

[3] A. Artemenko, A. Maltsev, A. Mozharovskiy, A. Sevastyanov, V. Ssorin, and R. Maslennikov, "Millimeter-Wave Electronically Steerable Integrated Lens Antennas for WLAN/WPAN Applications," *IEEE Trans. Antennas Propag.*, vol. 61, no. 4, pp.1665-1671, 2013.

[4] W. Roh, J. Y. Seol, P. JeongHo, B. Lee, J. Lee, Y. Kim, J. Cho, K. Cheun, and F. Aryanfar, "Millimeter-wave Beamforming as an Enabling Technology for 5G Cellular Communications," *IEEE Mag. Commun.* , vol. 52, no. 2, pp. 106-113, 2014.

[5] C. C. Cheng, A. Abbaspour-Tamijani, "Study of 2-bit Antenna–Filter–Antenna Elements for Reconfigurable Millimeter-Wave Lens Arrays," *IEEE Trans. Mic. Theory Techn.*, vol. 54, no. 12, pp. 4498-4506, 2006.

[6] S. B. Yeap, X. Qing, and Z. N. Chen, "77-GHz Dual-Layer Transmit-Array for Automotive Radar Applications," *IEEE Trans. Antennas Propag.*, vol. 63, no. 6, pp. 2833-2837, 2015.

Article 5

Design and Analysis of a Millimeter-Wave High Gain Antenna

E. Erfani, S. Safavi-Naeini, and S. O. Tatu

IET Microwaves, Antennas and Propagation, Accepted, Nov. 2018.

Abstract

On propose une antenne à réseau d'émission (TA) à large bande et à gain élevé, fonctionnant à 60 *GHz*. Pour répondre aux exigences liées à la conception d'une antenne TA, ayant des performances de rayonnement insensibles à la polarisation, on a conçu une cellule unitaire (UC) multicouche optimale. Les dimensions de la cellule unitaire sont paramétrées de manière à assurer une réponse en phase de transmission linéaire, ayant une plage de variation de 270 ° et une perte d'insertion inférieure à -3 *dB*, sur la bande de fréquence désirée, de 58 *GHz* à 64 *GHz*. Pour activer l'antenne TA proposée, on a aussi conçu un nouveau module de réseaux d'antennes planaires composé de connexions à ouverture couplée 2×4 intercalées avec une structure à surface souple. En outre, l'on a développé une approche semi-analytique afin de calculer les caractéristiques de rayonnement de l'antenne TA et l'on a comparé les résultats à ceux obtenus avec les simulations en pleines ondes. On a fabriqué l'antenne TA proposée et on en a présenté les résultats de mesure. Les résultats obtenus montrent une efficacité d'ouverture maximale de 38.48% (un gain maximal de 30.85 *dB*),

respectivement de 32.37% (un gain maximal de 30.1 *dB*), et un gain en largeur de bande à -1 *dB* de 7.7%, respectivement de 8.2%, par rapport aux simulations et aux mesures. Cette antenne à large bande et à gain élevé est considérée appropriée pour les liaisons terrestres en ondes millimétriques des systèmes cellulaires 5G.

Abstract

A broadband and high gain transmit array (TA) antenna, operating at 60 *GHz*, is proposed. To meet the design requirements of a TA antenna with polarization-insensitive radiation performance, an optimal multi-layer unit cell (UC) is introduced. The dimensions of the UC are parametrically expressed to realize a linear transmission phase response with a variation range of 270 ° and insertion loss less than -3 *dB* over the desired frequency band ranging from 58 *GHz* to 64 *GHz*. A new planar array composed of 2×4 aperture-coupled-patches interleaved with a soft-surface is also designed as a feed for the proposed TA. Furthermore, a semi-analytical approach is developed to calculate the radiation characteristics of the TA antenna and the results are compared to the ones achieved with full wave simulations. The designed TA antenna is fabricated and the measurement results are presented. The obtained results show peak aperture efficiencies of 38.48% (30.85 *dB* peak gain) and 32.37% (30.1 *dB* peak gain), and -1 *dB* gain bandwidths of 7.7% and 8.2% from the full-wave simulations and measurements, respectively. Such a broadband and high gain antenna is deemed to be suitable for *mm*-wave backhaul links in 5G cellular systems.

5.1 Introduction

The enormous amount of spectrum at millimeter-wave (mm-wave) frequencies and also recent advances in RF integrated circuits design, such as cost effective CMOS technology, have encouraged cellular service providers to take advantage of the mm-wave band as a potential solution for achieving more capacity and high data transfer rates in the emerging 5G wireless networks [1]-[5]. In the 5G networks, to cope with the mm-wave propagation loss and blockage hurdles, a wideband and high gain antenna with scanned/switched-beam capability in a narrow angular sector is desired for mm-wave backhaul links. Existing approaches including horn [1] and dielectric lens antennas [6],depending on the required gain, are rather expensive, bulky, and heavy. As an alternative, in

[5], a hybrid beam-forming antenna system has been proposed for 5G cellular networks to realize directive beam(s) in the desired direction(s) and to support various multi-antenna schemes such as multiple-input-multiple-output (MIMO) and diversity. Although, planar antenna arrays are usually the preferred choice because of the ease of fabrication/integration and costs, but they suffer from design complexity and excessive transmission-line losses when designed for high gain applications in mm-wave frequencies. Other proposed structures, which are operating based on leaky wave principles [7] and Fabry-Perot resonators [8], are intrinsically narrow band. Spatial beam-forming techniques such as reflectarray (RA) [9, 10] and transmitarray (TA) antennas [11]-[25] with their high efficiency and broadband performances are promising approaches for mm-wave frequencies. Compared to center-fed RA antennas, TA antennas do not suffer from feed blockage and they are less sensitive to the surface errors. In addition, they can fulfill multi-beam requirements through using a feed cluster without degrading the overall antenna radiation performances [25].

In a TA antenna, the waves emanated from the feed, placed at its focal point, are collimated by adjusting the phase delay of each unit cell of the TA. In TAs, the phase compensation is usually achieved using the phase characteristics of the periodic structures. Since the design of a mm-wave TA is challenging in term of fabrication limitations of low-cost standard printed-circuit board technology, a realizable phasing technique is required. A common approach is to utilize multiple layers of cascaded resonant or sub-wavelength frequency selective surfaces (FSSs) separated by dielectric or air gap, in which the phase can be continuously changed across the TA aperture [11]-[18]. For instance, in [12], by changing the sizes of a resonant dual-square-ring mounted on the four-layer of substrates, 270 ° continuous phase variation has been realized over the frequency range of 28-31 *GHz*. Alternatively, sub-wavelength multilayer elements have been used to considerably increase the TA bandwidth [1]-[13]. However, these kinds of multilayer structures are not easy to implement in mm-wave frequency ranges because of extremely high precision required in stacking of multi-layers (dielectric foam) and etching tolerance. An alternative approach is based on the quantized-phase receive/transmit elements concept proposed in [1]-[4], [25]. Specifically, a 60 *GHz* TA antenna has been demonstrated in [21], in which the receive/transmit antennas of each element are connected through a via. A similar quantized-phase element, constructed with dual metal-layer coplanar patches, has also been presented in [22], which is operating at 77 *GHz*. Nonetheless, the quantized-phase method causes an additional loss and radiation pattern degradation. Moreover, the via-holes increase the complexity and fabrication cost. Most recently, to avoid using vias and in-

crease the quantized-phase resolution to seven states, three phase shifting unit cells have been used to demonstrate a V-band switched beam TA [25]. Although, it has a high aperture efficiency for the fixed beam case (TA is fed with a horn antenna), the design fails to maintain this performance when a switched focal array is used as its feed (switched beam).

To address the demands of mm-wave cellular networks, this manuscript analytically and experimentally demonstrates a high gain, broadband, and polarization-insensitive TA antenna. Based on receive/transmit approach without any vias, a unit cell with continuous phase variation (270 °) is optimally designed to realize the required transmission coefficient response for a $15.6\lambda \times 15.6\lambda$ TA (where λ is wavelength at 60 GHz). A new planar 2×4 array of aperture-coupled-patch-antennas interleaved with a soft-surface is also developed as a feed for this TA. The advantages of soft-surface structures are exploited to improve the feed radiation performances with minimum number of excited elements. In addition, the radiation characteristics of this TA antenna are semi-analytically (SA) calculated and the results are compared with the full-wave (FW) simulation and measurement results.

5.2 Unit Cell Design

The configuration of the proposed wideband unit cell used to construct the TA has been shown in Fig. 5.1. It consists of five patterned metal layers embedded in between the layers of low loss dielectric material RO6002. Working as receiving antennas, two square patches in one side receive the incident signals and they are coupled to the other two transmitting patches through a resonant aperture etched on the ground. This technique has been utilized in TAs and is also known as Antenna-Filter-Antenna configuration [24]. Indeed, by exciting multiple coupled resonances, a low loss-band pass filter with broadband transmission response is created. In addition, because of the geometrical symmetry, the unit cell is insensitive to the polarization of incident waves.

To investigate the polarization-insensitive unit cell, frequency domain solver of Microwave CST Studio was used to simulate the scattering parameters of the proposed element. Its reflection and transmission coefficients for normal incident x- and y-polarized waves are plotted as a function of frequency in Fig. 5.2. In these simulations $L = 1.17\,mm$. As it can be seen, the unit cell operates as a band-pass filter with an identical l phase response for both incident field components. Indeed,

by effectively coalescing multiple resonances (because of two patches, slot, and interaction between them), the proposed unit cell demonstrates very low reflection coefficient responses for both vertically and horizontally polarized incident fields, i. e., highly transparent in a wide -3 dB transmission band of 39 *GHz*. The low loss transmission bandwidth is large enough to realize the required phase variation range across the TA aperture within the frequency range of 58-64 *GHz* when the filter resonance response is detuned by changing its dimensions.

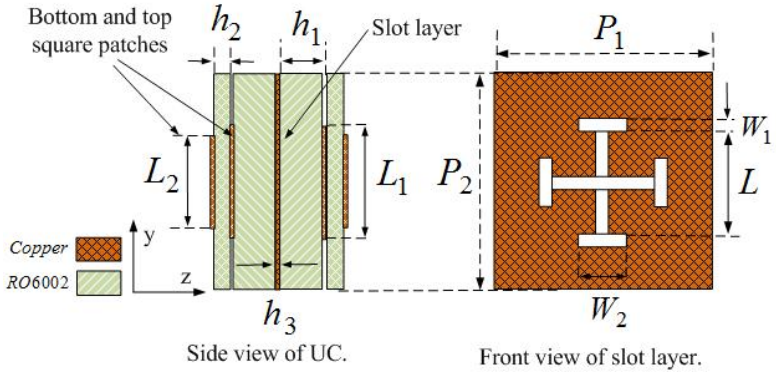

Figure 5.1 – Configuration of the proposed aperture-coupled-patch,element for TA antenna, P_1=P_2=2.6, h_1=0.508, h_2=0.127, h_3=0.017, ϵ_r=2.95, L = 1.17, L_1 = 0.975, L_2 = 0.95, and W_1=0.17 (all units are in mm).

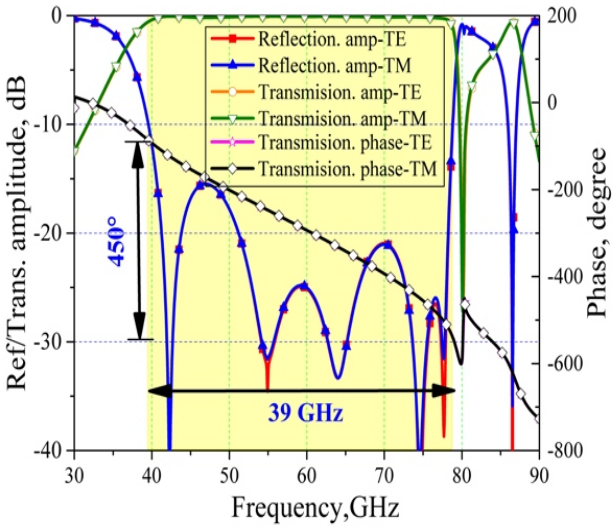

Figure 5.2 – Transmission and reflection coefficient responses of the proposed TA element simulated for $L = 1.17$ *mm*.

To maintain the desired performance for all elements of the TA, the dimensions of unit cell were optimized for four different regions (Reg.1 to Reg.4) and then a curve fitting approach was

used to derive a relation between the element dimensions and the phases shift over the entire TA. This results in desired phase transmission responses for both incident field components in a broad range of frequencies. The final dimensions of the unit cell for each region have been summarized in Table 5.1. The simulation results carried out at different frequencies are shown in Fig. 5.4. The results demonstrate that the proposed element has a linear and continuous phase variation range (at least 270 °) with low loss performance (less than -0.5 dB) within the -3 dB transmission band for both incident electric-field components. Furthermore, the element performance for different angles of incidence (up to 20 °) has been investigated, and it is demonstrated that it has a stable response for both polarizations. This polarization-insensitive unit cell is, therefore, a good choice to construct an efficient and broadband TA antenna.

Tableau 5.1 – Parametric expressions for the dimensions of the proposed unit cell shown in Fig. 5.2 for each simulated region.

Parm.(mm)	Reg.1	Reg.2	Reg.3	Reg.4
L	$0.6 - 1$	$1 - 1.3$	$1.3 - 1.7$	$1.7 - 2.05$
$P_1 = P_2$	2.6	2.6	2.6	2.6
W_2	0.3	$4.14L^4 + 2.6L - 12.4$	$0.12L^2 + 0.188$	$0.83L^2 - 2.4L + 2.25$
L_1	$0.11L^7 - 0.5L^4 + 0.9L^2 + 0.35$	$0.11L^7 - 0.5L^4 + 0.9L^2 + 0.35$	$0.17L^3 + 0.16L^2 + 0.9$	$-0.16L^2 + 0.76L + 0.46$
L_2	$0.26L + 0.5$	$-0.2L^5 + 0.68L^3 + 0.3$	$0.25L + 0.73$	1.15

5.3 Feed Design

A new millimeter wave 2×4-element antenna array is designed as a feed for the TA antenna. As it is illustrated in Fig. 5.4, the proposed feed is composed of an array of aperture-coupled-patches (ACPs) fed by a strip-line feeding-network, which are implement with three layers of Rogers substrates and PCB fabrication technology. Radiating elements of the proposed array are interleaved with three rows of shortened strips employed as a soft surface structure. To uniformly excited the elements, an optimized T-junction power divider and some quarter wavelength transformers are used to construct the feed network. In addition, to facilitate antenna characterization, a wideband strip-line-to-grounded-coplanar-waveguide (SL-to-GCPW) is designed. This transition has less than 0.5 dB transition loss in the 50-68 GHz frequency band.

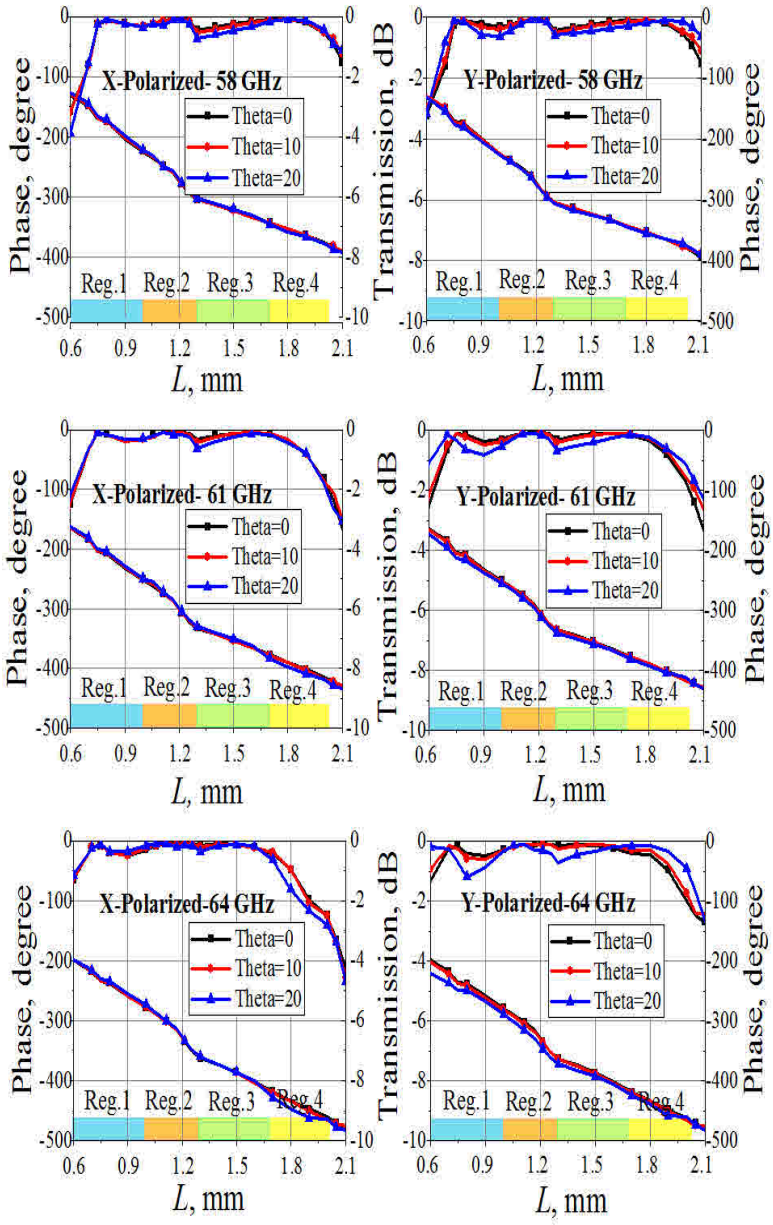

Figure 5.3 – Amplitude-length and phase-length curves of the proposed UC simulated at different angles of incidence across the desired frequency range.

In this antenna, the advantages of soft-surface structure are exploited to improve the array radiation performances in terms of directivity, side lobe level, and bandwidth by reducing the mutual coupling between its elements (because of the surface and radiating space waves) [26]. Indeed, maximum directivity is realized with the minimum number of excited elements (2×4-element) for a given aperture size (not shown here because of space paucity, it has been compared with its equivalent 4×4-element conventional array). This also reduces the complexity of the feed-network and decrease the fabrication cost. To achieve such electrical features, the soft-surface structure is

optimized to create a frequency band gap (56.9-72.4 *GHz*) for the waves propagating on the surface as well as an artificial magnetic conductor performance over the desired band of 58-64 *GHz* for the vertically-polarized incident waves. Not shown here for brevity, these results are achieved from the dispersion and reflection coefficient responses of a unit cell of the soft-surface structure. The soft-surface structure in two sides of the array is shaped to further improve the E-plane side lobe level of the array.

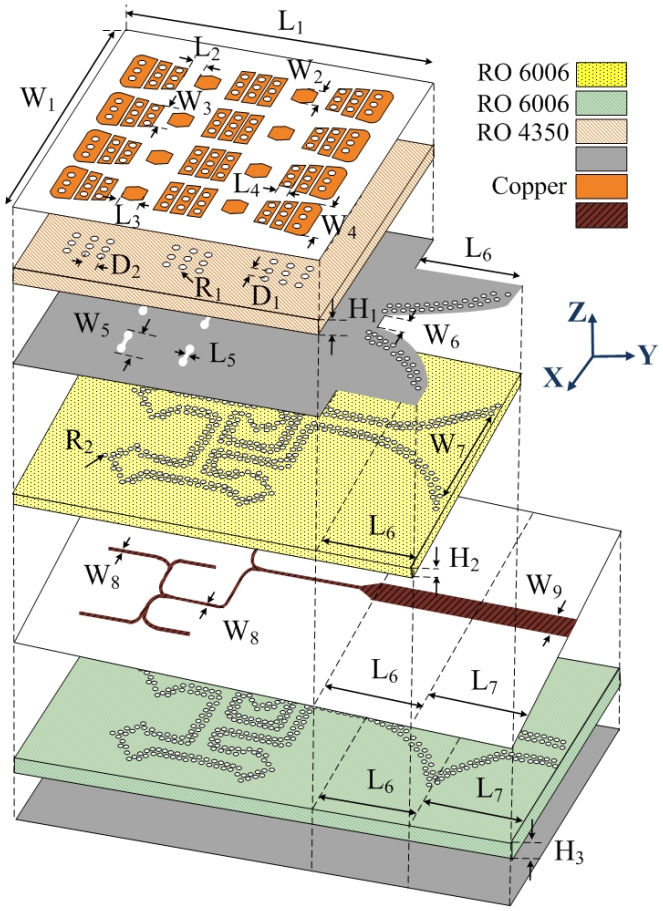

Figure 5.4 – Configuration of the proposed antenna array, W_1=16, W_2=1.2, W_3=2.3, W_4=2.6, W_5=0.88, W_6=0.17, W_7=4.7, W_8=0.15, W_9=0.35, L_1=14, L_2=0.175, L_3=1, L_4=0.65, L_5=0.17, L_6=6, L_7=4, R_1=0.1, D_1=0.825, H_1=0.254, H_2=0.127, and H_3=0.254, (all units are in mm).

The simulate reflection coefficient and realized gain of this feed are shown in Fig. 5.5, and they demonstrate -10 *dB* matched and -1 *dB* gain bandwidths of >22.9} (54-68 *GHz*) and >9.5} (59.2-65 *GHz*), respectively. The radiation pattern performance is only shown for the center frequency here in Fig. 5.6. Being more noticeable in the E-plane, where soft surface structure effectively operates, the side-lobe levels in the E- and H-planes are better than -17 *dB* and – 14 *dB* over the desired band. The simulation results show that, by accepting an average phase variation of 10.35 ° over the -10 *dB*

beam-widths of the E- and H-plane patterns within the desired frequency band, the phase center of this array is located on the central point of its top surface. These results show that the proposed feed can be used as a feed for the TA.

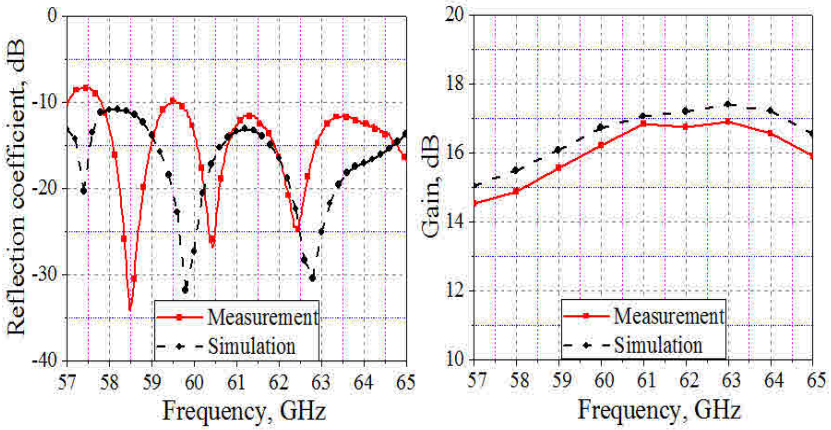

Figure 5.5 – Simulated and measured reflection coefficient (left) and realized gain (right) responses of the proposed antenna array.

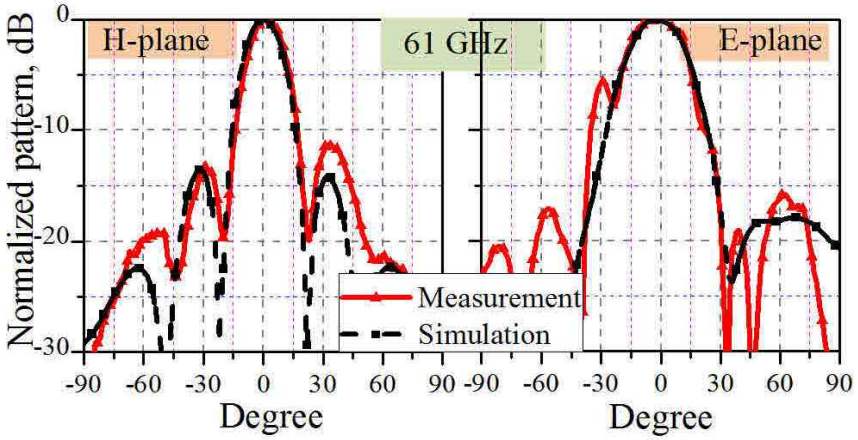

Figure 5.6 – Simulated and measured radiation patterns of the proposed antenna array.

5.4 Transmitarray Design and Experimental Results

5.4.1 Design and Analysis of The Proposed TA Antenna

The TA antenna is composed of 30×30 unit cells of the proposed element depicted in Fig. 5.1, and it is illuminated with the proposed feed shown in Fig. 5.4 placed at a distance F from the TA

surface. The side length of the square TA aperture is chosen to achieve the desired directivity of about 35 dBat the center frequency 61 GHz. In addition, $F \doteqdot 1.41$ is selected to realize a broadband and efficient antenna with a low side lobe level pattern. To collimate the feed radiation into the broadside direction, the corresponding phase delay of each element of the TA is calculated and the phase distribution on its aperture is illustrated in Fig. 5.7.

To calculate the radiation characteristics of the proposed TA, a semi-analytical approach is presented here and the results are compared to the ones obtained from a full wave simulator (the entire structure is simulated with transient solver of Microwave CST Studio). In this method, it is assumed that TA is in the far field region of the feed and hence its elements are locally excited with the incident plane waves. Indeed, as schematically demonstrated in Fig. 5.8, stacked patches of each element on the feed side receive the signal ray emanated from the feed. The power received by the receiving patches will then be reradiated by the transmitting patches on the other side. Using a mathematical model for the feed pattern and the element radiation pattern obtained from a full wave simulation of the reception and transmission processes of a single cell, the total radiation pattern of the TA can be easily calculated by the antenna array theory as described below [27].

In this work, the designed linearly polarized array is considered as a focal source for the TA and its radiation pattern is analytically approximated by equation (5.1)

$$\vec{E_y^f}(\acute{\theta},\acute{\phi}) = \frac{jke^{(-jkR\acute{}_{mn})}}{2\pi R\acute{}_{mn}} \cdot \left[C_e(\acute{\theta})\sin(\acute{\phi})\hat{a_\theta} + C_h(\acute{\theta})\sin(\acute{\phi})\hat{a_{\acute{\phi}}}\right] \tag{5.1}$$

where $C_e(\acute{\theta}) = \cos^{Q_e}(\acute{\theta})$ and $C_h(\acute{\theta}) = \cos^{Q_h}(\acute{\theta})$ are the E- and H-plane radiation patterns of the array expressed in the feed coordinate system, and $0 \leq \acute{\theta} \leq \frac{\pi}{2}$ and $0 \leq \acute{\phi} \leq \frac{\pi}{2}$ [28].

In this model, it is supposed that the pattern has no side/back lobe. This assumption introduces some errors in the calculated pattern mainly in the side-lobe region. The relevant parameters of E- and H-plane pattern functions in the method are achieved from the simulated radiation patterns over the desired operating band. Considering the schematic representation of TA antenna shown in Fig. 5.8 and assuming that the TA is in the far field region of the proposed focal array feed, the amplitude of the signal received by each element is proportion al to the induced open-circuit voltage, i. e. the vector dot product of $(\vec{E_{mn}^f} \cdot \vec{E_{mn}^r})$, where $\vec{E_{mn}^f}$ and $\vec{E_{mn}^r}$ are the feed and receiving

element radiation patterns' vectors in the TA coordinate system, respectively [27]. Then, weighted by the element transmission response (with a complex number), the induced voltage is considered as an excitation for the two stacked re-radiating patches on the other side of the TA. Therefore, from the knowledge of the elements' radiation patterns , i. e $\vec{E_{mn}^{t}}$, the total radiation pattern of the TA can be analytically calculated by the equation (5.2) expression

$$E(\theta,\phi) = \sum_{m=1}^{M}\sum_{n=1}^{N} \vec{E_{mn}^{f}} \cdot \vec{E_{mn}^{r}} |T_{mn}| e^{(j\angle T_{mn})} \cdot \vec{E_{mn}^{t}} e^{jkR_{mn}^{\vec{t}}\hat{r_0}} \tag{5.2}$$

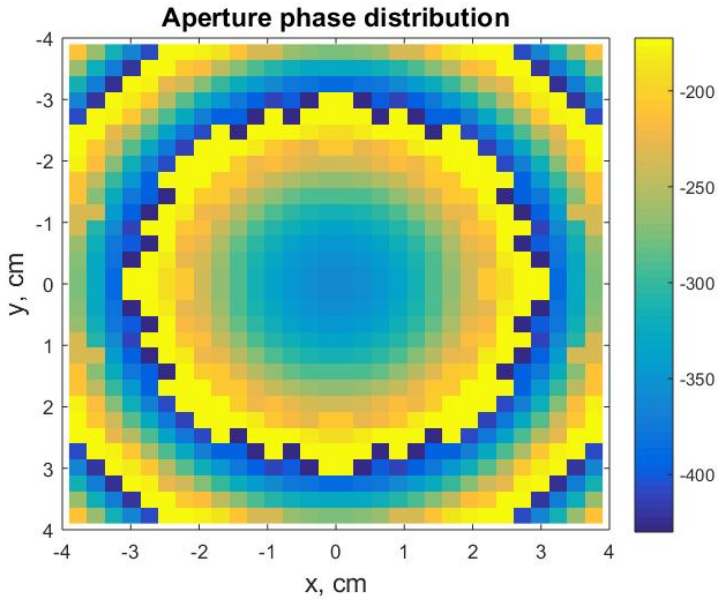

Figure 5.7 – Aperture phase distribution of the proposed TA calculated at 61 *GHz*.

The radiation pattern of one element (i. e, θ and ϕ far-field components) is simulated by the full-wave numerical solver CST Microwave Studio using periodic boundary model. Being a symmetric unit cell with respect to its ground plane, the simulated radiation pattern can be used for both receiving ($\vec{E_{mn}^{r}}$) and transmitting in ($\vec{E_{mn}^{t}}$) patches. Since periodic boundary conditions are applied in these pattern calculations, the effect of mutual coupling is considered to some extent. However, in the presented simulation results, the radiation pattern of the central unit cell, simulated at 61 *GHz*, has been used as a common model for all receive/transmit elements. This simplification has a negligible effect on the TA radiation pattern calculation, since the central region of the TA has the most significant contribution to the radiate field in the far zone.

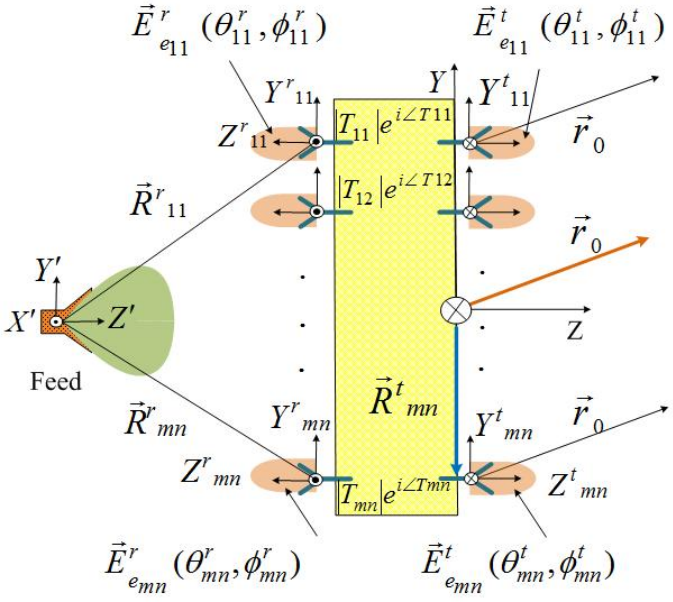

Figure 5.8 – Schematic representation of radiation pattern calculations of the proposed TA antenna. TA consists of 30×30 elements arranged in a square lattice with periodicity equal to $P_1 = P_2 = 2.6\,mm$.

5.5 Simulation and Experimental Results

To simulate the entire TA antenna with a rigorous full wave solver, firstly, the phase center of the proposed feed was determined as it was described in the previous section, and then it was aligned with the focal point of the TA. The parametric models of Table I at 61 *GHz* were used to determine the TA elements dimensions. The phase variation range across the aperture is about 270 °. The most linear and lowest loss region of the unit cell transmission coefficient response, as shown in Fig. 5.3, is chosen for the design of each TA element. Transient solver of CST Microwave Studio was used to calculate the radiation characteristics of the entire TA antenna. The obtained results reasonably agree with the ones simulated by theoretical approach, especially within the main beam region.

The designed TA and its feed were fabricated using a standard printed-circuit board technology and the radiation patterns of its feed and the entire TA antenna were measured inside the anechoic chamber by the far field method. A dielectric fixture was fabricated to hold the feed and the TA surface. Photos of fabricated TA, its feed, and its measurement setup are shown in Fig. 5.9. To verify the TA antenna performance, the proposed feed was firstly characterized and its parameters are compared with the simulated ones in Figs. 5.5 and 5.6. The achieved results confirm that the feed has wide matching and gain bandwidths with a good radiation pattern (small side lobe level in both

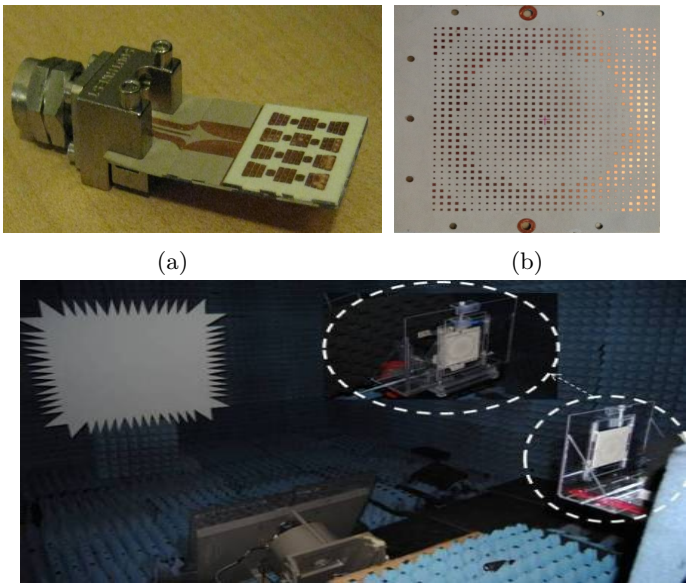

(a) (b)

(c)

Figure 5.9 – Photos of a) feed array, b) the TA, and c) its radiation pattern measurement setup.

E- and H-planes over the desired band). Slightly degradation noticed in the reflection coefficient response and pattern shape are because of the fabrication and end-launch connector effects.

Tableau 5.2 – Half-power beam-width of the proposed TA antenna achieved from full-wave simulation, SA-method, and measurement.

Frequency (GHz)			58	61	64
-3 dB beam width (degree)	Sim.	E	3.4	3.3	2.8
		H	4	3.4	4
	Meas.	E	3.7	3.3	3.2
		H	4.3	4	5.3
	SA.	E	3.44	3.27	3.29
		H	3.63	3.44	3.29

Then, the radiation characteristics of the TA antenna were measured and they are compared with the full wave and semi-analytical methods in Figs. 5.10 and 3.11. Being very close to the one measured for the feed alone, as shown in Fig. 5.10, the TA reflection coefficient is matched over the entire desired bandwidth and it follows the one achieved by the full wave simulator. The simulated results for the radiation patterns, as illustrated in Fig. 5.11, are in good agreement with measurements, particularly in the main lobe region, over a wide range of frequencies. Table 5.2

summarizes the -3 dB beam-width of radiation pattern within the bandwidth. As results show, there are some discrepancies between the near- and especially far-side lobe levels calculated by the analytical method with the ones of the two other cases. As it was expected, this is because of ignoring the side lobes of the practical feed pattern which has been mathematically modeled with cosine functions and the spillover radiation caused by the feed pattern. Moreover, the dielectric fixture may also affect the radiation pattern, especially the side lobe level in the E-plane. Therefore, considering that the feed has been modeled with an ideal mathematical expression, the developed method predicts the performance of designed TA with a reasonable accuracy.

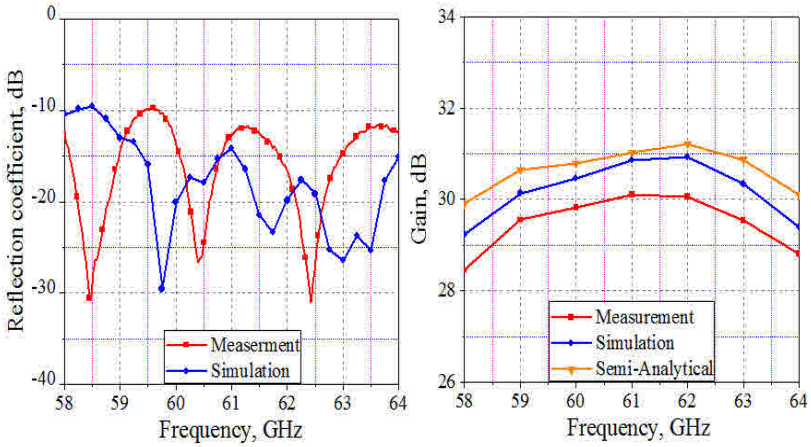

Figure 5.10 – Simulated and measured reflection coefficient (left) and realized gain (right) responses of the proposed TA antenna.

As a further validation, the realized gain of the TA was measured by using gain comparison method and is compared with the simulated ones in Fig. 5.10. The slight discrepancy between full wave and measurement might be due to the fabrication tolerances and measurement misalignments. The results show that the developed hybrid analytical method predicts the gain of antenna with a good accuracy especially close to the 61 GHz (where the element pattern was simulated and it was used for other frequencies within the desired bandwidth). The slight discrepancy at other frequencies is basically due to the feed modeling, violation of point source assumption, and the element pattern which has been ideally considered to be identical for all array elements. The -1 dB gain bandwidths of the TA achieved with SA-method, full-wave, and measurements are 9%, 7.7%, and 8.2%, respectively.

Finally, to fully characterize the performance of the proposed TA antenna, its calculated power budget and aperture efficiency are presented in Table 5.3. The values are determined for 62 *GHz*, where the measured realized gain is maximum. This table shows that the maximum calculated and measured antenna aperture efficiencies are 40.46% (at 62 *GHz*) and 32.37% (at 61 *GHz*), respectively. The peak aperture efficiency obtained from full wave simulation is 38.48% at 61 *GHz*.

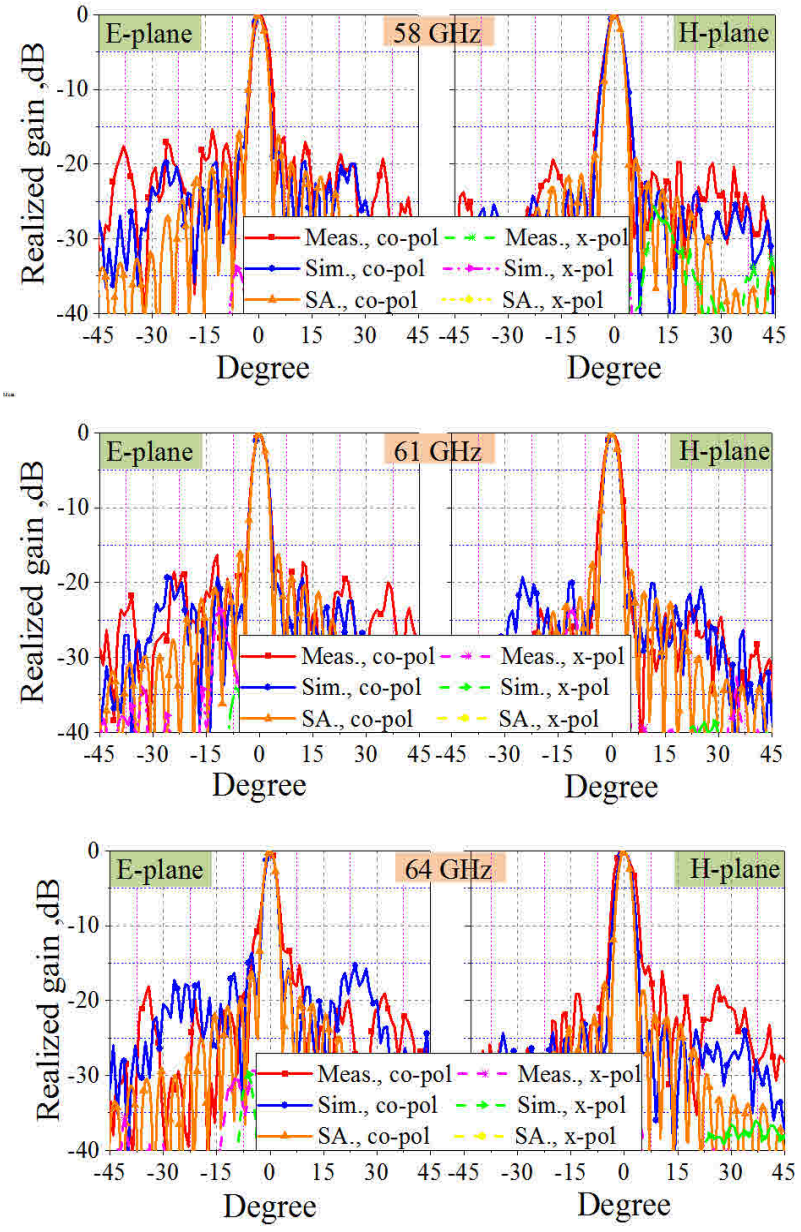

Figure 5.11 – Simulated and measured radiation pattern of the proposed TA antenna.

Tableau 5.3 – Loss budget of the proposed TA antenna.

	Peak gain value	
	SA method	Meas.
Directivity of a uniform aperture (dB)	35.14	
Calculated directivity of TA (dB)	33.48	
Calculated spill-over loss (dB)	0.66	
Calculated illumination loss (dB)	1.04	
Calculated insertion loss (dB)	0.6	
Gain of TA (dB)	31.21	30.1
Aperture efficiency (%)	40.46	32.37

Aperture efficiency is the ratio between maximum measured/simulated realized gain and the maximum directivity of the TA with uniform illumination. The peak aperture efficiencies are calculated at 62 GHz and 61 GHz for SA-method and measurement, respectively

5.6 Conclusion

This work demonstrates a broadband and high gain transmitarray antenna. An optimally designed multi-layer unit cell for mm-wave frequency range of 58-64 GHz is presented. The proposed unit cell has a continuous phase variation range of around 270 ° with insertion loss of less than -3 dB within the desired operating bandwidth for TA applications. Furthermore, a new planar array antenna is demonstrated as a feed for the proposed TA. A semi-analytical approach is also developed to calculate the radiation characteristics of TA antennas. The proposed method is validated through a successful comparison of the model results and those of the rigorous numerical method and measurements. The achieved results show that the high gain TA antenna has a good radiation characteristic within the frequency range of 58 GHz to 64 GHz. These features make this antenna a suitable choice for backhaul links in 5G cellular systems.

Bibliographie

[1] T. S. Rappaport S. Sun, R. Mayzus, H. Zhao,Y. Azar, K. Wang, G. N. Wong, J. K. Schulz, M. Samimi, and F. Gutierrez,“Millimeter wave mobile communications for 5G cellular: it will work!,” *IEEE Access*, vol. 1, pp. 335-349, May 2013.

[2] H-X. Wang, F. Haider, X. Gao, X-H. You, Y. Yang, D. Yuan, H. Aggoune, H. Hass, S. Fletcher, and E. Hepsaydir, "Cellular Architecture and Key Technologies for 5G Wireless Communication Networks," *IEEE Commun. Mag.*, vol. 52, no. 2, pp. 122-130, Feb. 2014.

[3] F. Boccardi, R. W. Heath, A. Lozano, T. L. Marzetta, and P. Popovski, "Five Disruptive Technology Directions for 5G," *IEEE Commun. Mag.*, vol. 52, no. 2, pp. 74-80, Feb. 2014.

[4] C. Dehos, J. L. Gonzalez, A. Domenico, D. Ktenas,and L. Dussopt, "Millimeter-wave Access and Backhauling, The Solution to the Exponential Data Traffic Increase in 5G Mobile Communications Systems," *IEEE Commun. Mag.*, vol. 52, no. 9, pp. 88-95, Sept. 2014.

[5] W. Roh, J. Y. Seol, P. JeongHo, B. Lee, J. Lee, Y. Kim, J. Cho, K. Cheun, and F. Aryanfar, "Millimeter-wave Beamforming as an Enabling Technology for 5G Cellular Communications: Theoretical Feasibility and Prototype Results," *IEEE Commun. Mag.*, vol. 52, no. 2, pp. 106-113, Feb. 2014.

[6] A. Artemenko, A. Maltsev, A. Mozharovskiy, A. Sevastyanov, V. Ssorin, and R. Maslennikov, "Millimeter-Wave Electronically Steerable Integrated Lens Antennas for WLAN/WPAN Applications," *IEEE Trans. Antennas Propag.*, vol. 61, no. 4, pp.1665-1671, Ap. 2013.

[7] J. L. Gomez-Tornero, F. Quesada-Pereira, and A. Alvarez-Melcon, "Analysis and Design of Periodic Leaky-wave Antennas for the Millimeter Waveband in Hybrid Waveguide-planar Technology," *IEEE Trans. Antennas Propag.*, vol. 53, no. 9, pp. 2834-2842, Sept. 2005.

[8] R. Sauleau, P. Coquet, T. Matsui, and J. Daniel, "A New Concept of Focusing Antennas Using Plane-Parallel Fabry-Perot Cavities with Nonuniform Mirrors," *IEEE Trans. Antennas Propag.*, vol. 51, no. 11, pp. 3171-3175, Nov. 2003.

[9] D. Pozar, S. Targonski, and H. Syrigos, "Design of Millimeter Wave Microstrip Reflectarrays," *IEEE Trans. Antennas Propag.*, vol. 45, no. 2, pp. 287-296, Feb. 1997.

[10] H. Kamoda, T. Iwasaki, J. Tsumochi, T. Kuki, and O. Hashimoto, "60- *GHz* Electronically Reconfigurable Large Reflectarray Using Single-Bit Phase Shifters," *IEEE Trans. Antennas Propag.*, vol. 59, no. 7, pp. 2524-2531, Jul. 2011.

[11] N. Gagnon, A. Petosa, and D. A. McNamara, "Research and Development on Phase-Shifting Surfaces (PSSs)," *IEEE Commun. Antenna Propag.*, vol. 55, no. 2, pp. 29-48, Ap. 2013.

[12] C. Ryan, M. R. Chaharmir, J. Shaker, J. Bray, Y. Antar, and A. Ittipiboon, "A Wideband Transmitarray Using Dual-Resonant Double Square Rings," *IEEE Trans. Antennas Propag.*, vol. 58, no. 5, pp. 1486-1493, May 2010.

[13] H. Nematollahi, J. J. Laurin, M. Barba, and J. A. Encinar, "Realization of Focused Beam and Shaped Beam Transmitarrays Based on Broadband Unit Cells," *IEEE Trans. Antennas Propag.*, vol. 65, no. 8, pp. 4368-4373, Aug. 2017.

[14] M. Niroo-Jazi, M. R. Chaharmir, J. Shaker, and A. R. Sebak, "Applications of Polarization-Independent Frequency Selective Filters for Transmitarray Antennas," *IEEE Symp. Antennas Propag.*, pp.1057-1058, Jul. 2014.

[15] M. Li, M. Al-Joumayly, and N. Behdad, "Broadband True-Time-Delay Microwave Lenses Based on Miniaturized Element Frequency Selective Surfaces," *IEEE Trans. Antennas Propag.*, vol. 61, no. 3, pp. 1166-1179, Mar. 2013.

[16] B. Rahmati, and H. R. Hassani, "High-Efficient Wideband Slot Transmitarray Antenna," *IEEE Trans. Antennas Propag.*, vol. 63, no. 11, pp. 5149-5155, Nov. 2015.

[17] L. Boccia, I. Russo, G. Amendola, and G. D. Di Massa, "Multilayer Antenna-Filter Antenna for Beam-Steering Transmit-Array Applications," *IEEE Trans. Mic. Theory Thechn.*, vol. 60, no. 7, pp. 2287-2300, Jul. 2012.

[18] A. H. Abdelrahman, A.Z. Elsherbeni, and Y. Fan, "High-Gain and Broadband Transmitarray Antenna Using Triple-Layer Spiral Dipole Elements",*IEEE . Antennas Wireless Propag. Lett.*, vol.13, pp.1288-1291, 2014.

[19] C. Pfeiffer, and A. Grbic, "Millimeter-Wave Transmitarrays for Wavefront and Polarization Control," *IEEE Trans. Mic. Theory Thechn.*, vol. 61, no. 12, pp. 4407-4417, Dec. 2013.

[20] C. C. Cheng,and A. Abbaspour-Tamijani, "Study of 2-bit Antenna–Filter–Antenna Elements for Reconfigurable Millimeter-Wave Lens Arrays," *IEEE Trans. Mic. Theory Thechn.*, vol. 54, no. 12, pp. 4498-4506, Dec. 2006.

[21] H. Kaouach, L. Dussopt, J. Lanteri, T. Koleck, and R. Sauleau, "Wideband Low-Loss Linear and Circular Polarization Transmitarrays in V-Band," *IEEE Trans. Antennas Propag.*, vol. 59, no. 7, pp. 2513-2523, Jul. 2011.

[22] S. B. Yeap, X. Qing, and Z. N. Chen, "77- *GHz* Dual-Layer Transmit-Array for Automotive Radar Applications," *IEEE Trans. Antennas Propag.*, vol. 63, no. 6, pp. 2833-2837, Jun. 2015.

[23] L. Di Palma, A. Clemente, L. Dussopt, R. Sauleau, P. Potier, and P. Pouliguen, "Circularly Polarized Transmitarray With Sequential Rotation in Ka-Band," *IEEE Trans. Antennas Propag.*, vol. 63, no. 11, pp. 5118-5124, Nov. 2015.

[24] A. Abbaspour-Tamijani, K. Sarabandi, and G. Rebeiz, "Antenna-Filter-Antenna Arrays as a Class of Bandpass Frequency-Selective Surfaces," *IEEE Trans. Mic. Theory Thechn.*, vol. 52, no. 8, pp. 1781-1789, Aug. 2004.

[25] L. Dussopt, A. Moknache, J. Saily, A. Lamminen, M. Kaunisto, J. Aurinslo, T. Bateman, and J. Francey, "A V-Band Switched-Beam Linearly Polarized Transmit-Array Antenna for Wireless Backhaul Applications," *IEEE Trans. Antennas Propag.*, vol. 65, no. 12, pp. 6788-6793, Dec. 2017.

[26] D. Sievenpiper, Lijun Zhang, R. F. J. Broas, N. G. Alexopolous, and E. Yablonovitch, "High-Impedance Electromagnetic Surfaces with a Forbidden Frequency Band,"*IEEE Trans. Mic. Theory Thechn.*, vol. 47, no. 11, pp. 2059-2074, Nov. 1999.

[27] W. L. Stutzman, and G. L. Thiele, "Antennas Theory and Design," *USA, Hoboken*, New Jersey, John Wiley and Sons, Inc., 3rd ed, pp. 101-103, 2012.

[28] Huang, and J. A. Encinar, "Reflectarray Antennas," *USA, Hoboken*, John Wiley and Sons, Inc., 1^{nd}, pp. 64-67, 2007.

Article 6

A V-Band High Gain Antenna System Integrated with a Six-Port Receiver

E. Erfani and S. O. Tatu

IEEE Transaction on Antenna and Propagation, Under revision, Oct. 2018.

Abstract

Une nouvelle antenne planaire à réseau d'émission (TA) à large bande et à gain élevé, intégrant un récepteur à six-ports, conçue pour les systèmes 5G de liaison terrestre est présentée dans ce chapitre. Pour répondre aux exigences de l'antenne TA (aussi dénommée antenne à lentilles diélectriques discrètes), on a conçu une cellule unitaire, insensible à la polarisation, avec une réponse en phase de transmission linéaire, une plage de variation de 270 ° et une perte d'insertion inférieure à -3 dB, sur une bande de fréquence désirée, de 58 GHz à 64 GHz. En outre, pour activer cette antenne à lentille planaire, on présente un nouveau module de réseaux d'antennes planaires composé de connexions à ouverture couplée 2×4 intercalées avec une structure à surface souple. La structure à surface souple est utilisée pour améliorer les performances du réseau en termes d'efficacité (gain), de largeur de bande et du niveau des lobes latéraux. Cette lentille discrète montre un gain maximal de 30.92 dB avec une efficacité d'ouverture de 38.4. Comme convertisseur abaisseur, l'on a conçu un circuit six-port composé de quelques éléments passifs et l'on en a fait une caractérisation complète,

afin d'obtenir des ports d'entrée/de sortie mis en correspondance, une isolation inférieure à -20 *dB*, et une bonne réponse en amplitude de transmission et en phase, sur toute la largeur de bande désirée. En outre, afin de récupérer les données de bande de base, on propose un détecteur de puissance équilibré, à une largeur de bande de plus de 10 *GHz*. Afin de faciliter les mesures, on a conçu et intégré dans le récepteur à six-ports une transition entre la ligne micro ruban et le guide d'ondes standard WR12, ayant une perte d'insertion inférieure à 0.2 dB sur une largeur de bande de 16 GHz. Par l'utilisation de la technologie d'interconnexion avec câblage filaire (bonding wire), l'antenne fabriquée avec la technologie PCB est intégrée à l'amplificateur à faible bruit (LNA) et au récepteur à six-ports fabriqué en technologie MHMIC. L'antenne à lentille planaire est testée pour différents types de constellations et de distances entre le récepteur et l'émetteur. Cette architecture d'antenne est considérée comme une solution innovatrice pour les communications sans fil en ondes millimétriques.

Abstract

A new high gain, broadband planar transmit-array antenna (TA) integrated with a six-port receiver is demonstrated for 5G backhaul systems. To meet the requirement of the TA (also dubbed as discrete planar lens antenna), a polarization-insensitive unit cell with a linear transmission phase response with a variation range of 270 ° and insertion loss less than -3 *dB* over a desired bandwidth of 58-64 *GHz* is designed. Furthermore, to excite this planar lens antenna, a new planar array module composed of 2×4 aperture-coupled-patches interleaved with a soft-surface structure is presented. Soft-surface structure is used to improve the array performances in terms of efficiency (gain), bandwidth, and side-lobe level. This discrete lens shows a peak gain of 30.92 with 38.4 aperture efficiency. As a down convertor, a six-port circuit composed of some passive elements is designed and fully characterized to obtain matched input/output ports, isolation less than -20 *dB*, and a good transmission amplitude and phase responses over the desired bandwidth. In addition, to recover the baseband data, a balanced power detector with a reflection coefficient bandwidth of more than 10 *GHz* is proposed. To facilitate the measurement, a Microstrip to WR12 transition with an insertion loss less than 0.2 *dB* over 16 *GHz* bandwidths is designed and integrated with the six-port receiver. By applying a bond wire, the antenna fabricated with PCB technology is integrated with LNA and six-port receiver built in MHMIC technology. The integrated planar lens antenna

is tested for different types of constellation and various distances between receiver and transmitter. This antenna architecture is considered as an innovative solution for long-distance millimeter-waves wireless communications.

6.1 Introduction

Recently, the data service proliferation and explosively increased needs on mobile data traffic have emerged the 5^{th} generation of cellular networks that are expected to address the plethora of high data rate and capacity [1]-[3]. Because of the abundant amount of unused frequencies available in millimeter-wave (mm-wave) frequency regime, this band has been considered as a prominent candidate for future 5G mobile communication. However, radio propagation at these frequencies suffer from high losses due to atmospheric absorption, rain, and foliage [1, 3]. Therefore, the use of a wideband high directive antenna is necessary to overcome the propagation loss.

Various types of high gain mm-wave antenna structures have been proposed for base stations [4]-[19]. Planar antenna arrays are usually the preferred choice because of the ease of fabrication/integration and costs. But they suffer from design complexity and excessive transmission-line losses when designed for high gain applications in mm-wave frequencies [5]. Other proposed structures which are operating based on leaky wave principles [6] and Fabry-Perot resonators [7], are intrinsically narrowband. Lens antennas with their high efficiency and broadband performances are promising approaches for mm-wave frequencies [8]-[11]. In [8], to achieve 30 dBi gain for backhaul system, an elliptical dielectric lens antenna has been fed with an integrated patch array antenna within a ball grid array module. In another work presented in [9], $2D$ beam-steering feature has been explored by illuminating a dielectric lens antenna with 64 patches integrated with a few switches. Nonetheless, dielectric lens antennas are bulky and expensive.

Alternatively, planar focused antenna systems including transmit-array (TA) and reflect-array (RA) are two promising approaches to design an aesthetically pleasing antenna with lower profile and cost compared to the dielectric lenses [12]-[19]. In addition, the antenna architecture gives the flexibility to easily integrate its feed system with the RF-circuitry without affecting the total radiation performances of the antenna system. In this perspective, TA (also dubbed as a discrete

lens) is much more attractive because of less sensitivity to its surface tolerances and architecture flexibility to mechanically scan the antenna beam.

In a TA antenna, the wave emanated from the feed are collimated by adjusting the phase delay of each unit cell of TA. A common approach is to utilize multiple layers of cascaded resonant or sub-wavelength frequency selective surfaces (FSSs) separated by dielectric or air gap, in which the phase can be continuously changed across the TA aperture [13]-[16]. For instance, in [13], by changing the sizes of a resonant dual-square-ring mounted on the four-layer of substrates, 270 ° continuous phase variation has been realized over the frequency range of 28-31 *GHz*. However, these kinds of multilayer structures are not easy to implement in mm-wave frequency ranges because of extremely high precision required in stacking of multi-layers (dielectric and foam) and etching tolerance. An alternative approach is based on the quantized-phase receive/transmit elements concept [17]-[19]. A 60 *GHz* TA antenna has been demonstrated in [17], in which the receive/transmit antennas of each element are connected through a via. Nonetheless, the quantized-phase method causes an additional loss and radiation pattern degradation. Moreover, the via-holes increase the complexity and fabrication cost. Since the design of a mm-wave TA is challenging in term of fabrication limitations of low-cost standard printed-circuit board technology, a realizable phasing technique is required.

To design a high performance planar focused antenna system, a wideband, low side-lobe level, and efficient feed tailored to the aperture of the designed TA/RA is required. In addition, this feed must have the flexibility to be easily integrated with the RF-circuitry with mm-wave interconnecting technologies including, ball-grid-array (BGA), land-grid-array (LGA)and wire-bonding [20, 21].

To address these requirements, planar antennas implemented with the antenna-on-chip (AOC) and antenna-in-package (AIP) integration solutions are two possible choices [22]-[25]. Because of the higher efficiency performance, AIP approach is preferred over AOC method, and it involves advanced fabrication and interconnection technologies to develop highly integrated devices, making them suitable for high-end applications. Alternatively, as a kind of AIP solution using same interconnection technologies, antenna package/module (AP/AM) solution is preferred for our application since there is no need to co-design the antenna and its package, and it can be fabricated with lower cost PCB fabrication technology [24]. In addition, low-cost wire-bonding method can be easily used to connect the antenna with RF circuitry. Therefore, the AP/AM method is the chosen antenna architecture to be integrated with a six-port based receiver here.

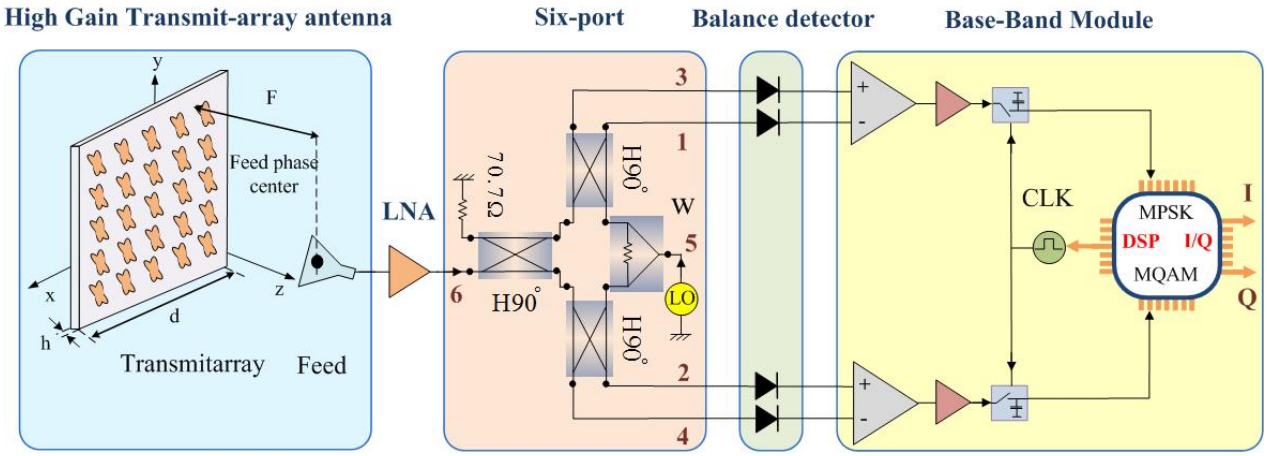

Figure 6.1 – Architecture design of the proposed integrated planar discrete lens antenna with six-port receiver.

In this paper, we will utilize a high gain planar discrete lens antenna (i. e., TA) and a six-port quadrature receiver with a low noise amplifier. From the antenna aspect, a new planar 2×4 array of aperture-coupled-patch-antennas interleaved with a soft-surface is specifically developed as a feed for the proposed TA. The advantages of soft-surface structures are exploited to improve the feed performance with minimum number of excited elements. In addition, based on receive/transmit approach without any vias, a unit cell with continuous phase variation (270 °) is optimally designed to realize the required transmission coefficient response for a $15.6\lambda \times 15.6\lambda$ TA (where λ is the free space wavelength at 60 GHz). Furthermore, the six-port receiver as a low-complex architecture consisting of only passive components, low dc power, and suitable for integrating with discrete components, is used to demonstrate a low-cost mm-wave receiver integrated with the proposed high gain antenna [26]-[28]. In this regard, a broad band V- band six-port structure is designed and characterized using the Miniature Hybrid Microwave Integrated Circuit (MHMIC) technology. In addition, to improve the bandwidth and dynamic range, a balanced detector configuration is also proposed. The wire bonding interconnection approach is utilized to interconnect all the received components on an aluminum fixture.

6.2 Receiver Architecture

The architecture of the proposed integrated high gain planar lens antenna with the six-port receiver is presented in Fig. 6.1. It consists of a planar discrete lens (i. e., a TA), feed array antenna,

low noise amplifier (LNA), six-port down-convertor, balanced detector diodes, and baseband module. In this architecture, the planar discrete lens adjusts the phases of RF-signals intercepted by its aperture and focuses them in its focal point, where the proposed novel planar feed array is located. Thereafter, RF-signals received by the feed array are amplified by a LNA and enter into the input port of six-port quadrature down-convertor. The six-port circuit consists of three compact 90° -hybrid couplers and a Wilkinson power divider. This circuit has two inputs, the local oscillator (LO) port (5) and RF-signals port (6), and four outputs (1-4) connected to the matched power detectors. The output signals of this six-port are linear combinations of two input signals with different phase shifts (0°, 90°, 180°, and 270°). Each of the four outputs are injected into a diode operating in its quadratic region, where the output voltage depends linearly on the input power. In addition, a balanced detector diode structure is proposed to improve the bandwidth and dynamic range of the receiver. The I and Q signal can be attained by appropriately subtracting output detected voltages with a differential amplifier. If the frequency of RF and LO signal is identical, the circuit operate in direct conversion scheme. A sample-and-hold circuit (SHC) processes the amplified output baseband signals and a time clock synchronizes the quadrate outputs. These signals are then used as the inputs of a digital signal processing (DSP) module. A four-inputs digital oscilloscope can be utilized in a laboratory set-up for convenience to replace the base-band module. It can display the four output detected voltages (quadrature differential ones), generate quadrature $\frac{I}{Q}$ signals using math functions, and display the demodulated constellation using Lissajous curves. In the following sub-sections, the step-by-step design and characterization results of the proposed integrated receiver are presented and discussed. First, the developed high gain planar lens antenna is presented and discussed.

6.2.1 High Gain Transmit-array Antenna System Design

To achieve a wideband and efficient antenna system, both TA and its feed must be accurately designed. In this work, the size of square TA aperture is chosen to achieve a directivity of about $35\,dB$ at the center frequency $61\,GHz$. The focal distance to aperture size ratio of $\frac{F}{d} = 1.41$ is selected to realize a broadband and efficient antenna with a low side lobe level pattern. The TA antenna is composed of 30×30 unit cells based on the concept of band-pass filters (BPF) realized with frequency-selective-surfaces (FSS) [16]. As shown in Fig. 6.2, the unit cell of TA consists of five patterned metal layers embedded in between four layers of low loss dielectric material RO6002. Two

patches in one side of the stacked dielectric layers receive the incident signals and they are coupled to the other two transmitting patches through a resonant Jerusalem cross aperture. Not shown here for brevity, the proposed unit cell simulated using periodic boundary model in CST Microwave Studio demonstrates a -3 *dB* transmission bandwidth of 39 *GHz* with a large phase variation range of 450 ° over the bandwidth of 40-80 *GHz*.

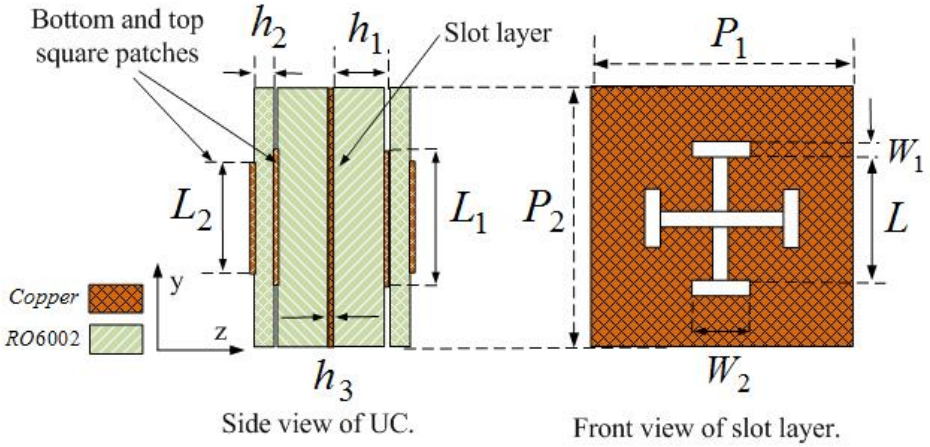

Figure 6.2 – Configuration of the proposed aperture-coupled-stacked-patch element for the TA antenna, $P_1 = P_2 = 2.6$, $h_1 = 0.508$, $h_2 = 0.127$, $h_3 = 0.017$, $\epsilon_r = 2.95$, $L = 1.17$, $W_1 = 0.17$, $W_2 = 0.7$, $L_1 = 0.975$, **and** $L_2 = 0.95$ **(all units are in** mm**).**

To maintain the desired performance for all elements of the TA, dimensions of the unit cell were optimized for four different regions, and then a curve fitting approach was used to derive a relation between the element dimensions and the maximum realizable phase variation. This results in desired phase transmission responses for both TE- and TM-incident field components in a broad range of frequencies. The results demonstrate that the proposed element has a linear and continuous phase variation range (at least 270 °) with low loss performance (less than -0.5 *dB*) within the -3 *dB* transmission band for both incident electric-field components. Furthermore, the element performance is stable for angles of incidence of at least 20 ° , making it a good choice for our application.

To focus the RF-signals intercepted by the TA aperture at its focal point, the corresponding phase delay of each element of the TA is calculated by using ray-tracing approach and the phase distribution on its aperture is illustrated in Fig. 6.3 [29]. In this method, it is supposed that each element of TA is in the far filed region of the antenna array feed. The calculated phase distribution determines the required dimensions of each unit cell within the TA aperture to compensate the differential spatial delay from center of that unit cell to the focal point of the TA. The central elements within the aperture are chosen from the ones having the most linear phase variation responses with the

minimum transmission loss performance. In the next step, to realize a high gain antenna with large aperture efficiency over the desired bandwidth, the TA aperture must be ideally matched to -10 *dB* radiation pattern beam-width of the antenna feed located in its focal point. Therefore, a broad band and stable radiation pattern feed antenna with -10 *dB* radiation beam-width of about 40 ° (ideally in both planes) and low side lobe level must be designed.

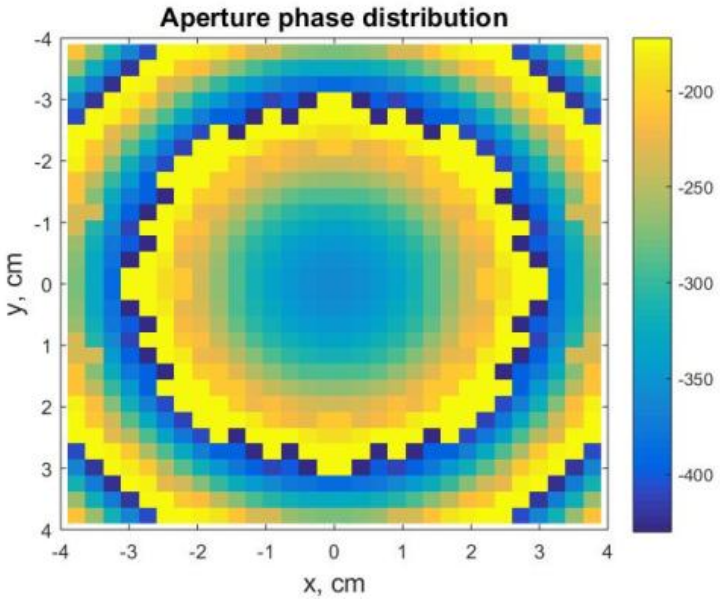

Figure 6.3 – Aperture phase distribution of the proposed TA antenna calculated at 61 *GHz*.

The proposed novel antenna array feed is shown in Fig. 6.4. It is composed of 2×4 aperture-coupled-patch (ACP) antennas interleaved with an artificial material (soft-surface-structure). The soft-surface-structure consists of three rows of shortened strips, and the ones in two sides of the array are shaped to improve the array pattern shape and its side-lope-level. The array is fed using a corporate-feed network implemented with strip-line transmission lines. To connect the antenna feed to the RF-circuit using wire-bonding method, a new broadband low loss strip-line-to-microstrip-line transmission is also designed and integrated with the antenna feed network. Furthermore, this facilitates the characterization of antenna feed and TA antenna system before integration with other parts of the receiver. This transition is well matched and it has less than 0.5 *dB* transition loss over the entire desired band. The soft-surface-structures and electromagnetic band gap materials are usually used to improve only one or two radiation characteristics of an antenna usually in terms of gain and bandwidth [30]. In this work, their potentials are fully exploited to improve the antenna feed radiation performances in terms of matching and directivity bandwidths, efficiency (gain), side-

lobe-levels, and pattern shape. By using the proposed soft-surface-structure, the number of excited elements is also reduced by two times compared to a conventional array with the same aperture sizes to get almost equal directivity/gain over the matched bandwidth. This considerably decreases the complexity of the feeding network and array stack-up. The feed array was optimized with CST Microwave Studio and its dimensions are defined in Fig. 6.4.

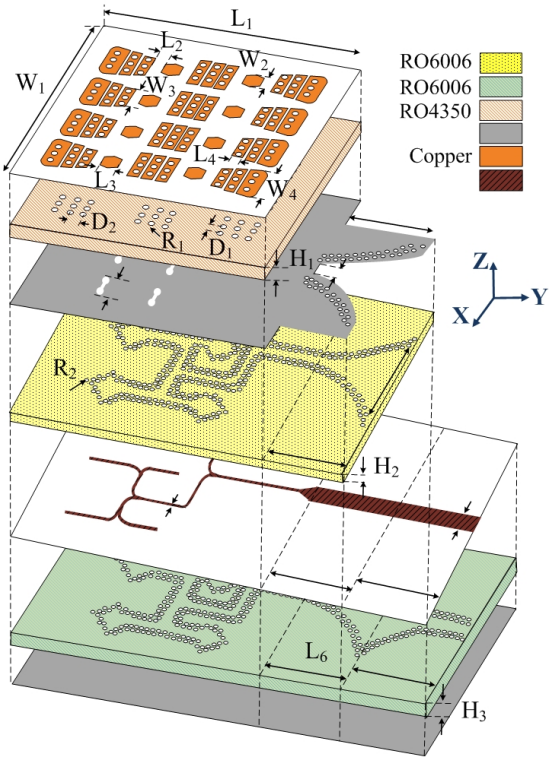

Figure 6.4 – Configuration of the proposed antenna array, W_1=16, W_2=1.2, W_3=2.3, W_4=2.6, W_5=0.88, W_6=0.17, W_7=4.7, W_8=0.15, W_9=0.35, L_1=14, L_2=0.175, L_3=1, L_4=0.65, L_5=0.17, L_6=6, L_7=4, R_1=0.1, R_2=0.07, D_1=0.825, H_1 = 0.254, H_2=0.127, and H_3=0.254, (all units are in mm).

Printed-circuit-board (PCB) fabrication technology was used to fabricate TA and its feed array. To fabricate the feed array, three antenna layers are individually etched, their vias are plated, and then they are glued under pressure and heat. The same assembly method was used to fabricate the TA. A dielectric fixture was also prepared to hold the array feed and TA in the characterization setup. The photos of fabricated TA, feed array, and their measurement setup are shown in Fig. 6.5.

The TA antenna system was experimentally characterized and its results are compared with the simulated ones in Figs. 6.6-6.10 . The simulate reflection coefficient and realized gain of this feed are shown in Figs. 6.6 and 6.7, and they demonstrate -10 dB matched and -1 dB gain bandwidths of >22.9% (54-68 GHz) and >9.5% (59.2-65 GHz), respectively. In addition, the antenna feed shows a

simulated and measured gain of 17 *dB* and 16.7 *dB* at 61 *GHz*, respectively. The radiation pattern performance is only shown for the center frequency here in Fig. 6.8. Being more noticeable in the E-plane, where soft surface structure effectively operates, the side-lobe levels in the E- and H-planes are better than -17 *dB* and – 14 *dB* over the desired band. These results justify how the advantages of soft-surface-structures can be fully exploited to improve the antenna radiation performances and reduced the design complexity.

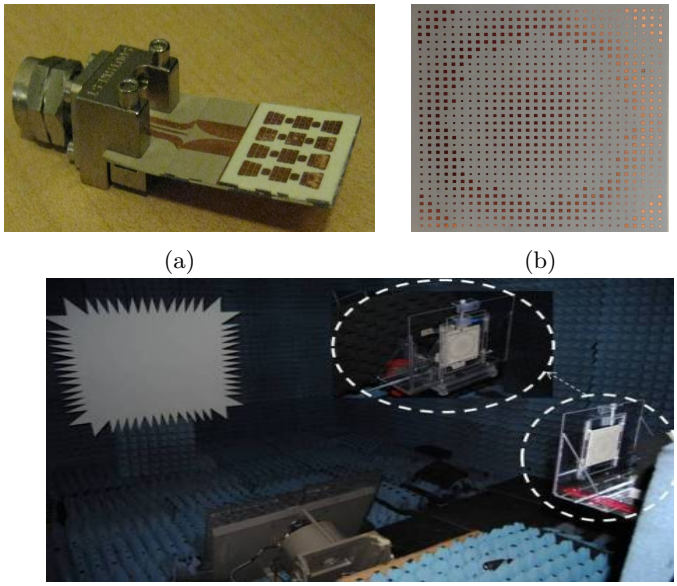

(a) (b)

(c)

Figure 6.5 – Photos of a) feed array, b) the TA, and c) its radiation pattern measurement setup.

Finally, the simulation results show that, by accepting an average phase variation of 10.35 ° over the -10 *dB* beam-widths of the E- and H-plane patterns within the desired frequency band, the phase center of this array is located on the central point of its top surface. These results show that the proposed feed can be used as a feed for the TA.

After characterizing the antenna feed, the entire TA antenna system is characterized in the anechoic chamber and its measurement results are compared with the simulated ones as shown in Figs. 6.9 and 6.10. To achieve the simulation results, the entire structure (i. e., feed and TA without dielectric supporting fixture) is simulated with transient solver of Microwave CST Studio. The gain plot shows -1 *dB* gain bandwidths 7.7%, and 8.2% for the simulated and measured cases, respectively. The slight discrepancy between full wave and measurement might be due to the fabrication tolerances and measurement misalignments. The achieved results show that the maximum simula-

ted and measured antenna aperture efficiencies are 38.48% and 32.37% at 61 *GHz*, respectively. As a further validation, the simulated and measured radiation patterns are in good agreement over the desired bandwidth (especially for the main beam region) and it is only shown for 61 *GHz* in Fig. 6.10. The side lobe level degradation is mainly because of the aperture phase error caused fabrication tolerances, measurement misalignment and scatterings from dielectric fixture not included in the simulations. Overall, the achieved results confirm the proposed antenna as a solution to address the high gain requirement of mm-wave applications.

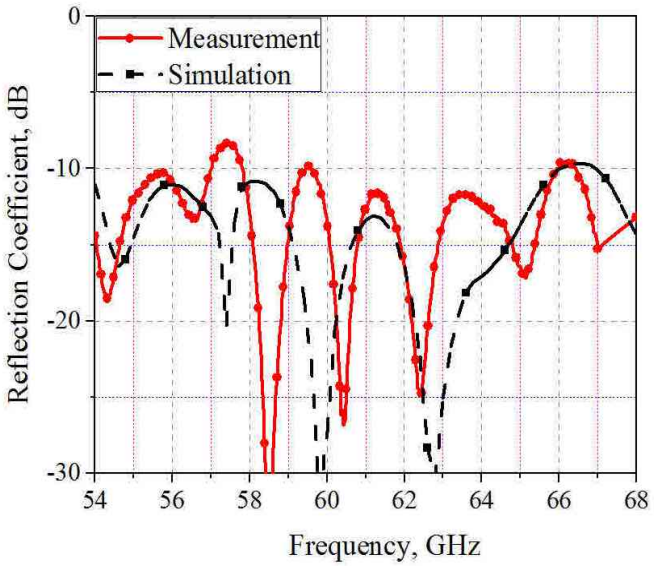

Figure 6.6 – Measured and simulated reflection coefficient of the proposed feed antenna.

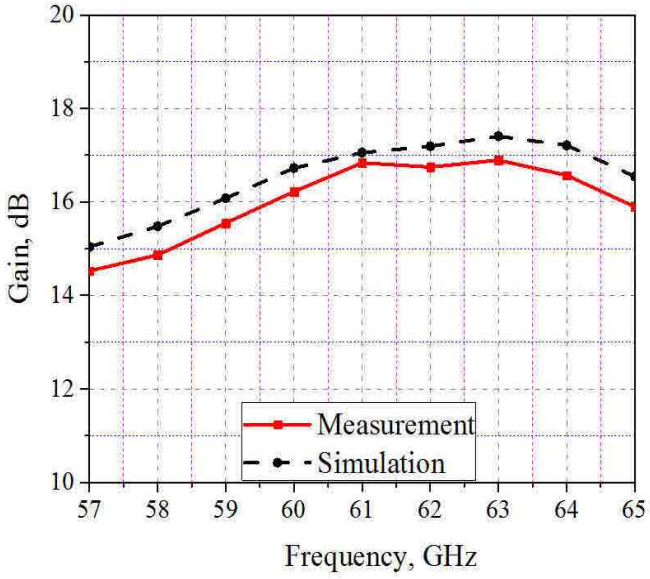

Figure 6.7 – Measured and simulated realized gains of the proposed feed antenna.

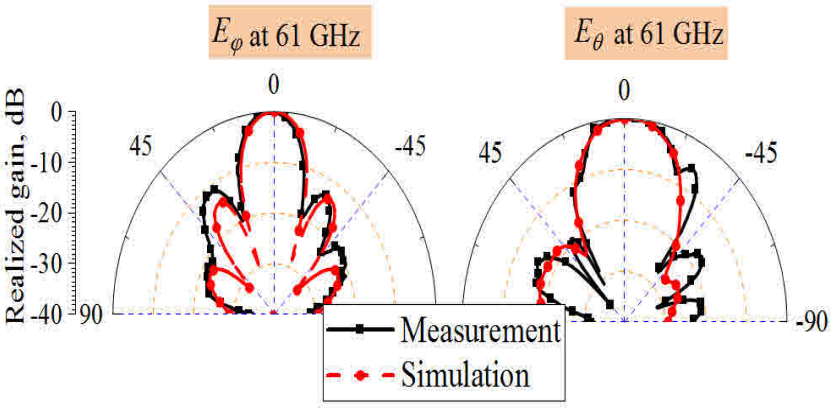

Figure 6.8 – Measured and simulated radiation patterns of the proposed feed antenna.

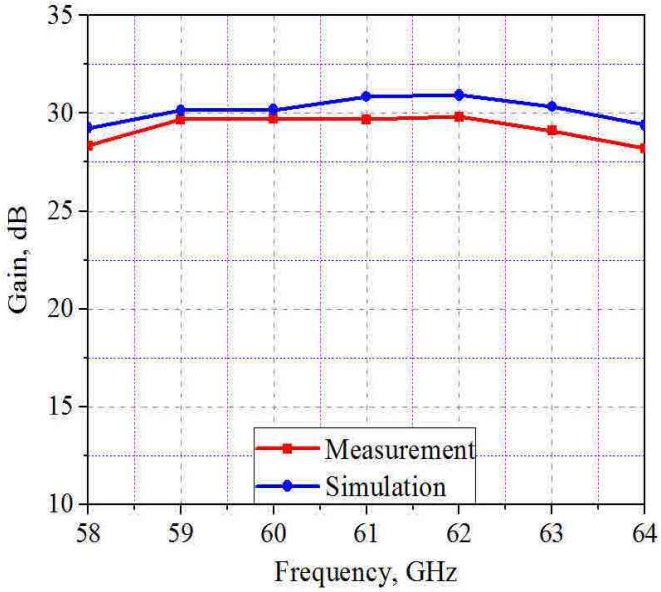

Figure 6.9 – Measured and simulated realized gain of the proposed TA antenna.

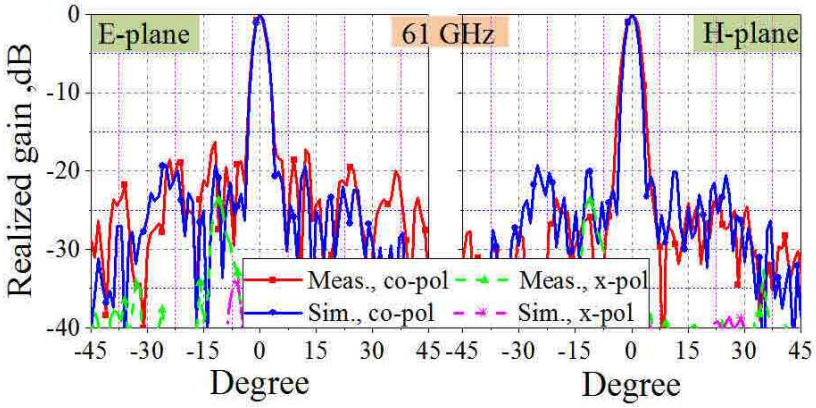

Figure 6.10 – Measured and simulated radiation patterns of the proposed TA antenna.

6.2.2 Six-Port Demodulator Design and Characterization

As it is schematically shown in Fig. 6.1, the six-port quadrature demodulator consists of three compact 90° hybrid couplers interconnected with a Wilkinson power divider through transmission lines. To optimally design the proposed six-port structure, its constructing components are individually optimized with Momentum tool of Advanced Design System (ADS) software of Keysight Technologies in terms of best matching, maximum isolation, and minimum transmission loss over the desired bandwidth and then they are integrated and fine-tuned.

To reduce the interconnection loss between antenna and six-port structure and decrease the wire bond length, the thickness of six-port substrate is chosen as the same as the thickness of antenna feed substrate (0.254 mm). In addition, to miniaturize the circuit, alumina substrate with a high relative permittivity substrate is chosen, which is compatible with MHMIC technology.

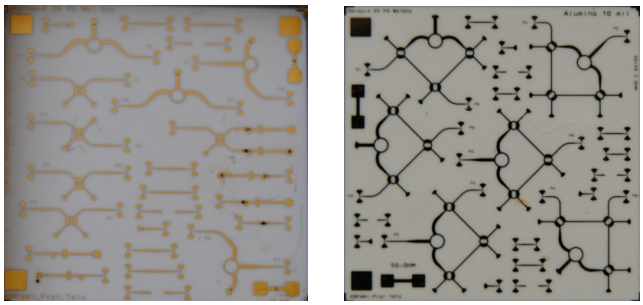

(a) (b)

(c)

Figure 6.11 – Photo of, a) MHMIC component and diode, b) MHMIC six-port circuit, and c) Picoprobe measurement setup.

To minimize the loss caused by thin dielectric thickness in mm-wave region, a high characteristic impedance of 70.7Ω and rounded-shape microstrip transmission lines are utilized to design the power divider and the hybrid couplers. The wide band Wilkinson power divided is implemented with two pieces of half-wavelength long 0.091 mm width transmission lines connected to a 100Ω integrated

resistor. Similarly, the quadrature hybrid coupler is designed with some pieces of rounded-shape microstrip transmission lines with width of 0.291 and 0.082 mm and length of 0.289 mm.

In addition, to facilitate the characterization of designed components and six-port structure with a 150 μm Cascade Microtech Ground-Signal-Ground (GSC) waveguide probe station, a transition of 70.7Ω microstrip to 70.7Ω GCPW has been designed and connected to each ports of circuits. In the characterization setup, the unused ports are terminated with matched 70.7Ω loads.

Fig. 6.11 shows a microphotograph of fabricated characterization chip of the designed components and six-port structure, and a picture of on wafer measurement with Pico-probes. Each die consists of multiple through-reflect-line (TRL) calibration kits, which includes non-zero length thru, open, and delay line. The length of delay line is related to the higher measurement frequency. These kits are used to calibrate the two-port network measurement system. In addition, a squared metallization pad is utilized for the alignment of Pico-probe in terms of mechanical pressure and electrical contact of three probe. Since the six-port structure is symmetric, six measurement cases are enough to completely characterize it on a single ceramic die of 2.54 $cm \times 2.54$ cm.

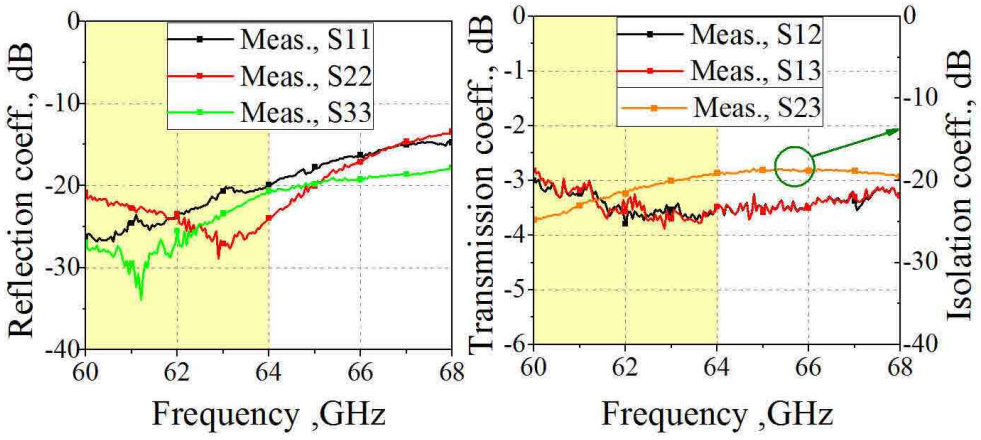

Figure 6.12 – Reflection and transmission coefficient responses of the power divider.

The measured scattering parameters of fabricated MHMIC circuit are shown in Figs. 6.12-6.16. Because of the measurement frequency range limitation of the equipment, the results are shown for the range of 60 GHz to 68 GHz. In addition, agreeing with the simulations, only measurement results are shown for better figure clarifications.

The measured results of the Wilkinson power divider in Fig. 12 show a reflection coefficient of less than -20 *dB* with a quite stable transmission loss of 3.7 *dB* and an isolation better than -20 *dB* between its output ports over the desired band width of 58-64 *GHz*. The additional 0.7 *dB* transmission loss might be because of the scratch on the very thin metallized gold layer created during the measurement process and calibration accuracy. Alternatively, the results for hybrid coupler also demonstrate a reflection coefficient better than -17 *dB* at all ports and isolation around 16 *dB* as depicted in Fig. 6.13. The measured phase response of 90 ° hybrid coupler is also illustrated in Fig. 6.13, showing a phase shift of about 89 ° over the desired band.

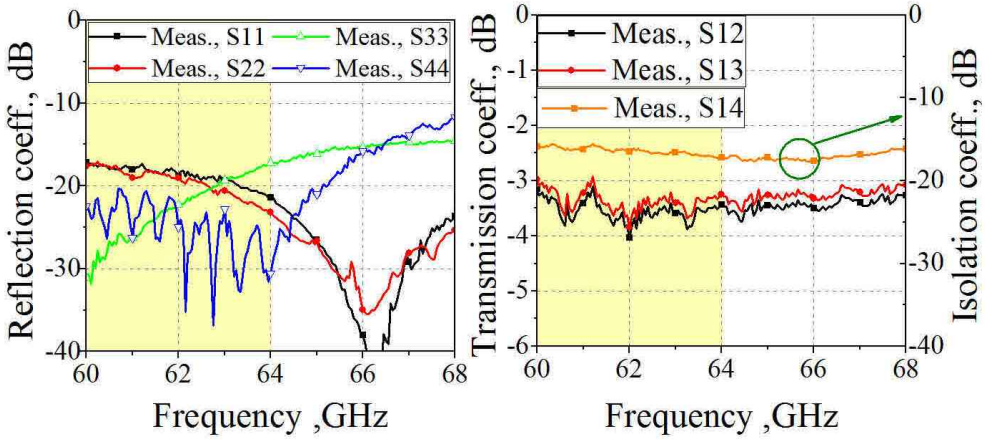

Figure 6.13 – Reflection and transmission coefficient responses of the hybrid coupler.

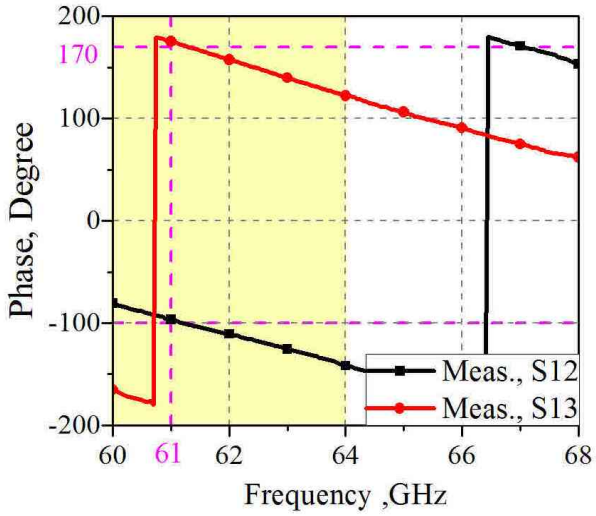

Figure 6.14 – Phase of transmission coefficient response of the hybrid coupler.

The measured scattering parameters, magnitude and phase of transmission responses of the six-port, when the RF-signal is injected into port 6 are depicted in Figs. 6.15 and 6.16, respectively. It can be observed that, a reflection coefficient of less than -20 *dB*, a magnitude variation less than 0.6 dB, and a quasilinear phase variation with respect to 90 ° multiple differences over the desired bandwidth are achieved. These results are well in the expectation range of the six-port circuit designed as a quadrature down converter [26].

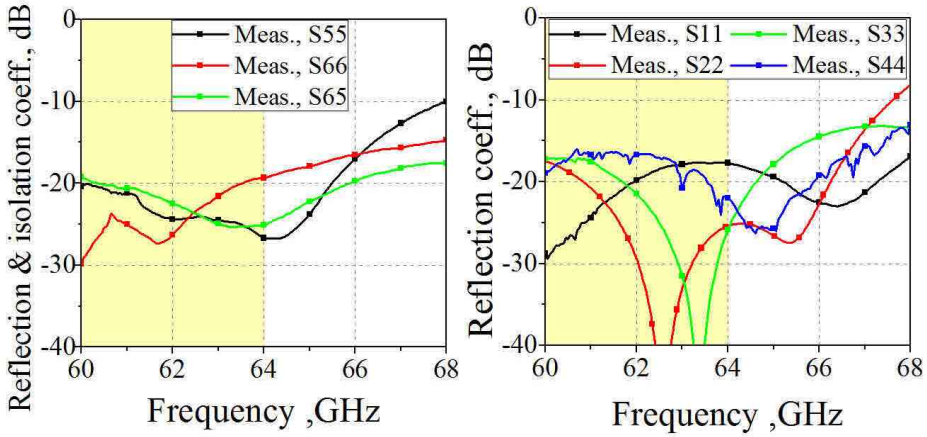

Figure 6.15 – Reflection coefficient and isolation responses of the input and output ports of the proposed six-port structure.

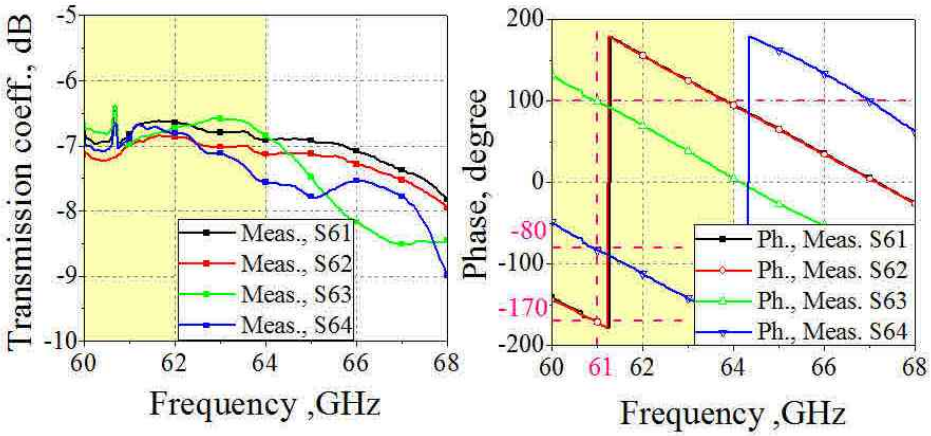

Figure 6.16 – Transmission performance of the six-port structure between its RF-input and four RF-output ports.

6.2.3 Diode Power Detector Design and Characterization

To recover the low IF signals, four outputs of the six-port are connected to power detectors as schematically shown in Fig. 6.1 To have a reliable communication and increase the link performance, any reflection caused by elements such as diodes should be prevented. Therefore, measuring scattering parameters of diodes to characterize them, and accordingly, designing impedance matching circuits at millimeter wave frequency band is necessary. Several millimeter wave RF power detector circuits have been proposed in [31]-[32]. In [31], a power detector circuit with an impedance bandwidth of 3.8 GHz has been presented for low frequency applications, which it consists of an input impedance matching network, GaAs Schottky diode, and detected DC voltage output circuit. However, in millimeter-wave frequency band, any change in the position of diode during fabrication process causes a considerable degradation in the matching performance of the circuit. Therefore, a wide band power detector circuit is required to demonstrate a wideband six-port receiver architecture. To address this requirement, in this paper, the advantages of balanced configuration is exploited in the design of power detector.

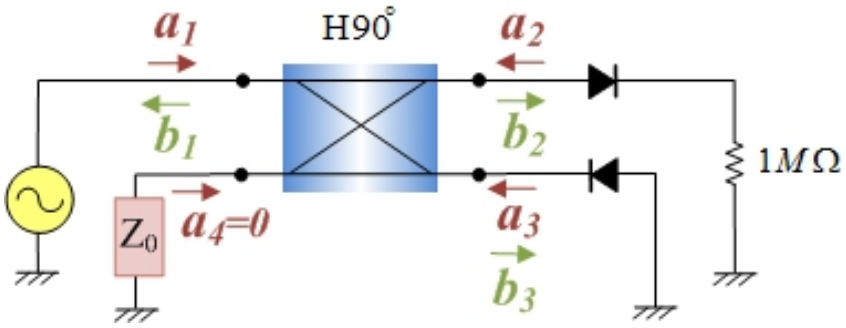

Figure 6.17 – Configuration of the proposed balanced diode power detector.

As it is depicted in Fig. 6.17, two identical zero-bias Schottky diodes of $HSCH-9161$ are connected to the port 2 and 3 of a hybrid coupler, while port 4 is terminated with an impedance of 70.7Ω. Considering $\Gamma=\frac{a_3}{b_3}=\frac{a_2}{b_2}$ (supposing two diodes are quasi-identical) and $a_4=0$ (matched port 4 with Z_0 load), normalized power outputs are expressed in equation (6.1).

$$\begin{bmatrix} b_1 \\ b_2 \\ b_3 \\ b_4 \end{bmatrix} = \frac{1}{\sqrt{2}} \begin{bmatrix} 0 & j & 1 & 0 \\ j & 0 & 0 & 1 \\ 1 & 0 & 0 & j \\ 0 & 1 & j & 0 \end{bmatrix} \cdot \begin{bmatrix} a_1 \\ \Gamma b_2 \\ \Gamma b_3 \\ 0 \end{bmatrix} \tag{6.1}$$

It can be easily shown that the output at port 1 is given by

$$b_1 = \frac{1}{\sqrt{2}} \cdot (jb_2 + b_3) \cdot \Gamma \tag{6.2}$$

and

$$b_2 = \frac{1}{\sqrt{2}} \cdot (ja_1), b_3 = \frac{1}{\sqrt{2}} \cdot (a_1) \tag{6.3}$$

Therefore, proving the desired performance of a balanced RF-circuit, the total reflection at port 1 will be zero and port 1 is ideally matched.

$$b_1 = \frac{1}{2} \cdot (-a_1 + a_1) \cdot \Gamma = 0 \tag{6.4}$$

To design the power detector based on the described principle, the scattering parameters of diode is firstly measured by a calibration and characterization setup designed for this purpose. Then, by using the measured scattering parameters of the diode, the proposed balanced power detector depicted in Fig. 6.16 is designed. It is implemented on the ceramic substrate ($\epsilon = 9.9$ and h=0.254 mm). In this design, the wideband RF short circuit at port 3 is realized by a balanced butterfly and via hole. Being in good agreement with each other, the achieved measured reflection coefficient response of power detector results is compared with the simulated one in Fig. 6.18. It is demonstrated that a wideband measured impedance bandwidth from 60-70 *GHz* is achieved by the

proposed configuration. It should be mentioned again that due to frequency limitation of Keysight vector network analyzer (E8362B), only the performance for frequencies higher than 60 *GHz* could be measured.

The power detection range of proposed circuit can be measured by injecting an RF-signal to the input port of the proposed detector, while a digital multimeter of Keysight 34401A is connected to its output. The detector was separately build in a metallic fixture to allow connection to standard millimeter wave equipment (WR-12 rectangular waveguide). The input signal is generated by an HP Series Synthesized frequency synthesizer with +6 *dBm* output power connected to a K-band power amplifier with a gain of 10 *dB* in series with a millimeter wave frequency multiplier (×83) of SFP-123KF-S1. The input power can be controlled through a linear millimeter wave waveguide attenuator of DORADO VPS-12. The simulated and measured results of output detected power versus input power at 61 *GHz* is shown in Fig. 6.20. It can be concluded that the proposed power detector shows a measured dynamic range of more than 50 *dB* with a good linearity and high sensitivity with minimum detectable input power level of -55 *dBm*.

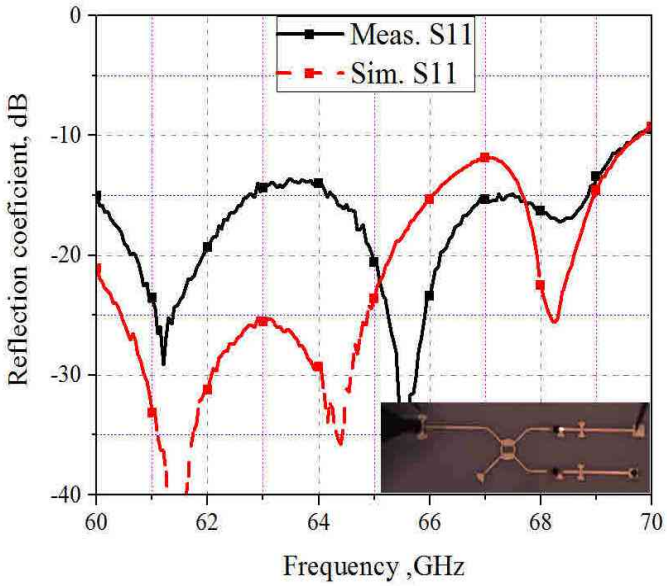

Figure 6.18 – Measured and simulated reflection coefficient of the MHMIC power detector.

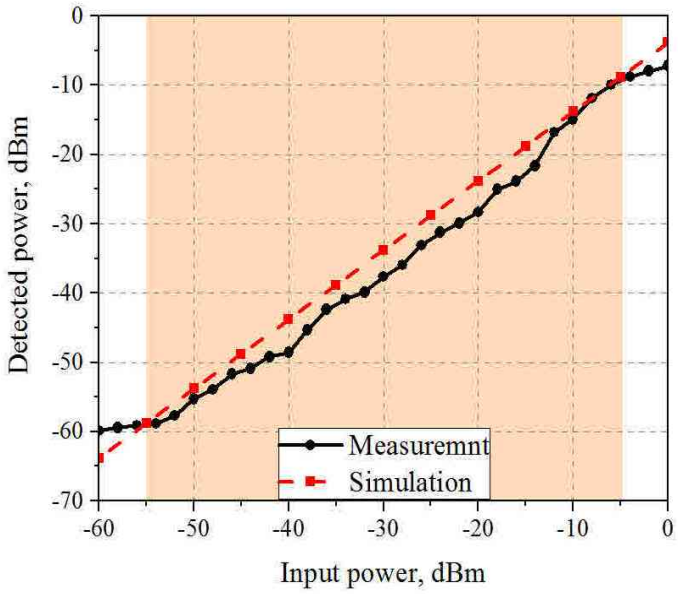

Figure 6.19 – Measured and simulated detected power versus input power at 61 *GHz*.

6.2.4 Transition Microstrip-line to WR12 Design

To facilitate measurements of the proposed receiver with our available lab equipment, a microstrip-line (MSL) to a standard WR12 waveguide transition is designed for the local oscillator port on a piece of ceramic substrate with $\epsilon_r = 9.9$ and $H_1 = 0.254\,mm$ as shown in Fig. 6.20 [33]. This transition consists of two parts, a transition between MSL to substrate-integrated-waveguide (SIW) section and a transition between SIW to WR12. In the first part, a linearly tapered MSL with the length of L_5 and width of W_3 is used to transfer a quasi-TEM mode of microstrip line to the TE10 mode of SIW line. The second transition is accomplished by a quarter wave transformers wave guide with length of L_2 and width of W_1 (same width as standard size of WR12). In addition, to improve the performance of the transition, a tapered metalized tip with length of L_4 is added to the structure. The whole proposed transition is simulated with HFSS and its results is depicted in Fig. 6.21. The results show an insertion loss of less than 0.2 *dB* and reflection coefficient of better than -20 *dB* over frequency range of 55-70 *GHz* for the designed transition.

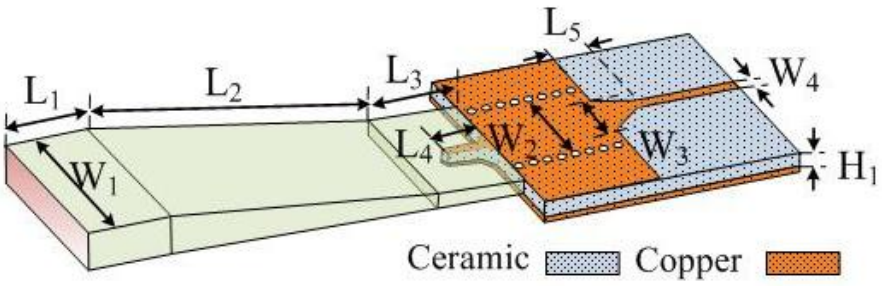

Figure 6.20 – Configuration of the proposed MSL to WR12 waveguide transition. W_1**=3.09,** W_2**=1.61,** W_3**=0.457,** W_4**=0.254,** L_1**=3.8,** L_2**=12.7,** L_3**=1.9,** L_4**=1,** L_5**=0.55, and** H_1**=0.254 (all units are in** mm**).**

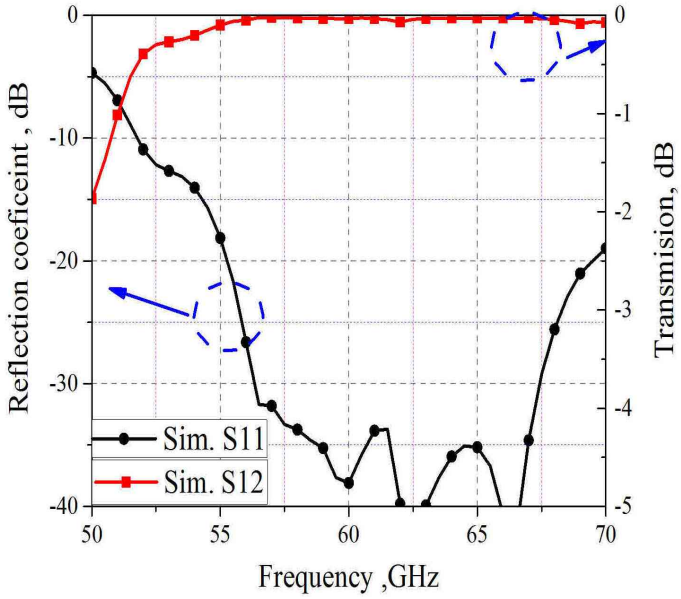

Figure 6.21 – Simulated reflection coefficient and transmission responses of the proposed MSL to WR12 waveguide transition.

6.3 Integration of Receiver Components and Measurement Results

The proposed receiver board and its aluminum base support is shown in Fig. 6.22. The antenna array feed and the six-port structure are placed on a metallic basement to increase the mechanical strength of the RF-circuit board and facilitate the measurements. The RF signal received by the antenna array feed is amplified by the TGA4600 LNA from TriQuint Semiconductor with 13 dB active gain and 4 dB noise figure. A quarter-wave impedance transformer of 70.7Ω to 50Ω is utilized at port 6 of six-port structure to match the LNA output port. To embed the LNA chip into the RF-circuitry on the PCB board, wire-bond interconnection technique is used. In general, due to inductive loading effect of the bonding wire at millimeter frequencies, it imposes significant insertion loss on the received RF signal, especially when long-length wire is used. To compensate the inductive effect of wire bonds by introducing a parallel capacitance, multiple bonds or ribbon type bond are usually used [25]. In this prototype, a low-height and short-length bonding method is used to integrate LNA with other parts of the receiver by devising a rectangular metallic step in the metallic base as shown in Fig. 6.22a. In addition, to realize a short wire-bond length, the minimum possible distance of D_1=3 mil between chip and dielectric substrates is chosen. Based on the LNA datasheet, V_d an V_g are connected to the chip through two 100 pF capacitors as illustrated in Fig. 6.22b. The whole structure of receiver with SMA connectors at output ports of 1 to 4 and WR12 waveguide at input port 5 is shown in Fig. 6.22c.

A transmit-receive measurement setup, as schematically depicted in Fig. 6.23, is used to characterize the system performance of proposed integrated six-port receiver shown in Fig. 6.1. In the transmission side of this setup, the HP 8360 Series Synthesized Sweeper output with the power of 6 dB and frequency of 20.6 GHz is utilized as a carrier signal f_{LO}. Then, it is connected to a commercial K-Band power amplifier with a gain of 10 dB and is multiplied by a mm-wave frequency multiplier model of SFP-123KF-S1 (×3). The Agilent E4438C Vector Signal Generator provides PSK/QAM modulated IF signals (600 MHz) with a 2-10 dBm power level. The modulated signal is up converted to a 60 GHz band signal by a mixer. The RF signal is then fed into a standard horn antenna (operating in 60-90 GHz band with a gain of 22 dBi) for transmission.

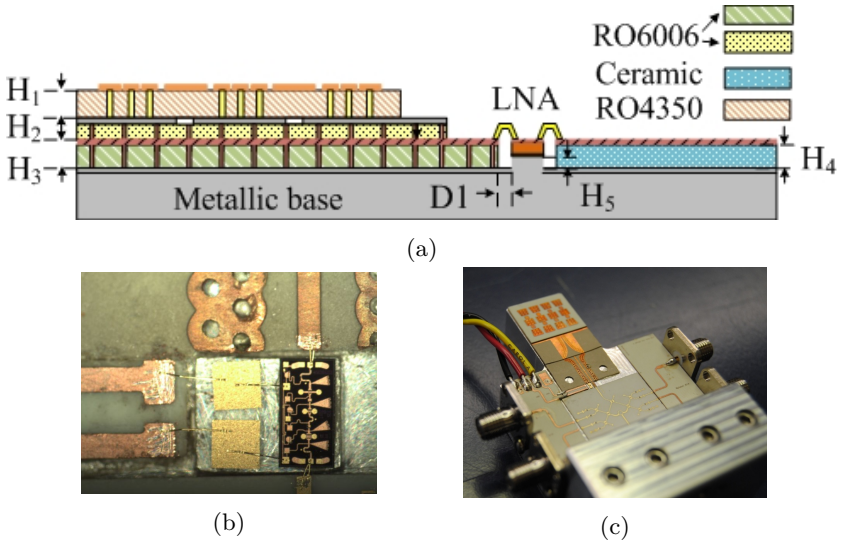

Figure 6.22 – Photos of a) cross section view of the overall receiver circuit with $H_1 = H_3 = H_4 = 0.254\,mm$, $H_2 = 0.127\,mm$, $H_5 = 0.1\,mm$, and $D_1 = 3\,mill$, b) the packaged LNA integrated with the antenna array feed and six-port structure, c) the proposed antenna system integrated with six-port.

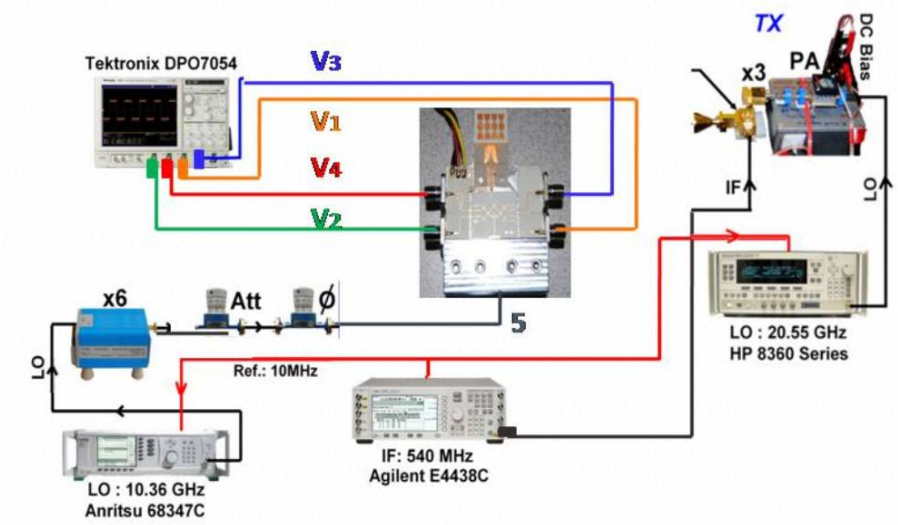

Figure 6.23 – System test setup for the V-band six-port receiver.

In the receive side, the antenna array integrated with six-port receiver is fixed in the focal point of TA by using the devised dielectric fixture. The signal is received by our proposed high gain TA antenna with a gain of about 31 *dBi*. Thereafter, the received RF signal is down converted to an IF signal using our proposed V-band six-port receiver. A carrier signal f_{LO} is provided by a signal generator (Anritsu 68347C with the frequency of 10.1725 *GHz* and a power level around 10 *dBm*) that is multiplied by 6 with a OML multiplier model S12MS. Its output power is accurately controlled through a linear millimeter-wave waveguide attenuator of DORADO. The four detected

powers are sent to a Tektronix DPO7054 oscilloscope to measure the transceiver system parameters. The photograph of our system set up for line-of-sight (LOS) is shown in Fig. 6.24. The system measurement is carried out for QPSK and PSK modulating schemes and various d, the distance between the transmitter and receiver. The measured constellation diagrams of QPSK and 8PSK for $d = 50\,cm$ and symbol rate of $R_s = 100KS/s$ for the receiver without and with the proposed TA structure is shown in Fig. 6.25.

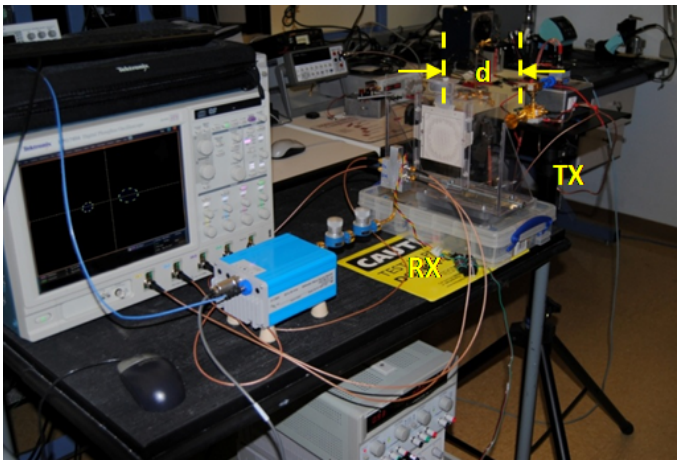

Figure 6.24 – Photo of our system test setup (d is the distance between the transmitter and receiver).

It can be observed that stable and clear output constellations are achieved. Furthermore, by using TA in front of the feed, the amplitude of the constellation is considerably increased. Because of the dependency of the location of the symbol points to the relative phase error between RF and LO signals, they are spread out around their ideal locations and constellation diagram looks somewhat fuzzy. They are related to millimeter-wave oscillator synchronization because of use of several multipliers on our particular set-up.

Well confirming the expected performance for larger distances between receiver and transmitter, the constellation diagrams for different values of d are shown in Fig. 6.26 for QPSK and in Fig.6.27 for 8PSK modulation schemes. It can be demonstrated that by utilizing a high gain antenna in the receiver structure, the capability of receiver to detect signal in higher range is considerably improved

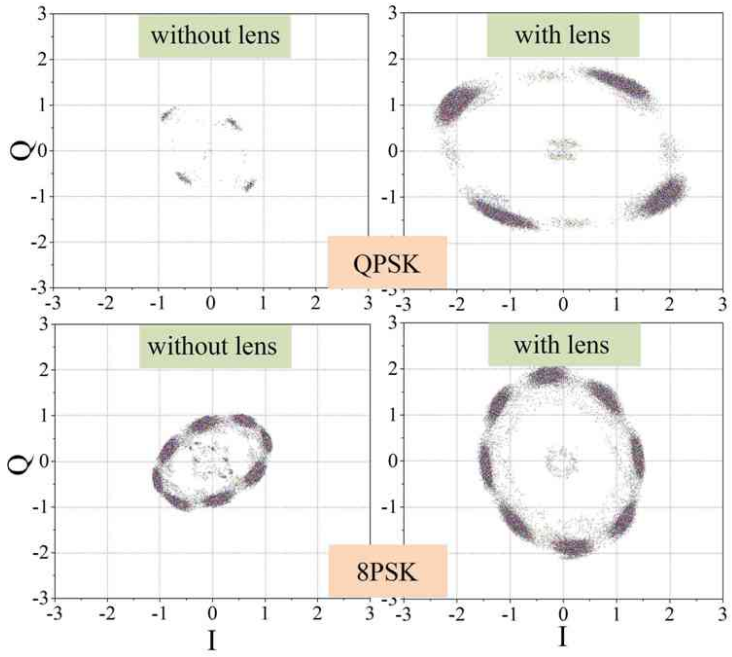

Figure 6.25 – Measured constellation diagrams for QPSK and 8PSK modulations without and with the proposed TA.

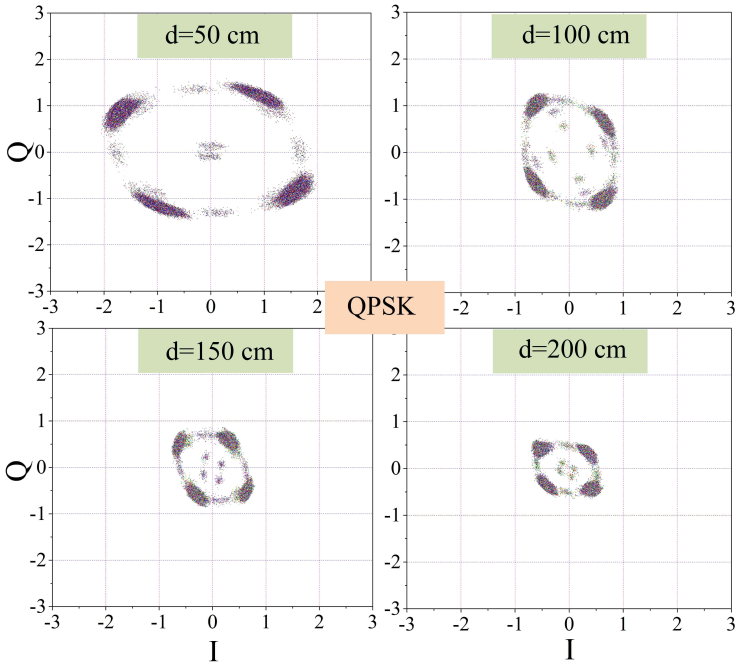

Figure 6.26 – Measured constellation diagrams of QPSK for various values of d (d is the distance between the transmitter and receiver).

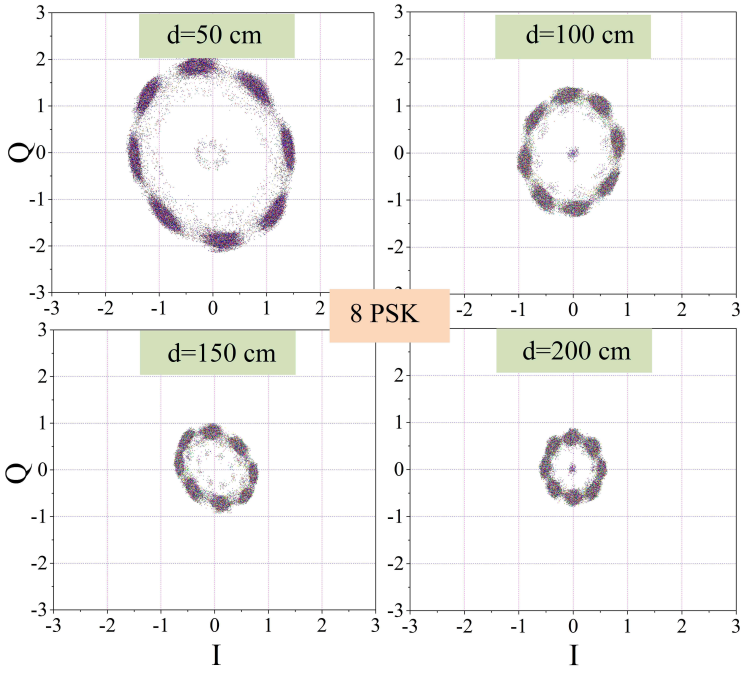

Figure 6.27 – Measured constellation diagrams of 8PSK for various values of d (d is the distance between the transmitter and receiver).

6.4 Conclusion

This paper presents detail design of an integrated high gain antenna with six-port receiver at 60 *GHz*. A planar TA fed with a new array antenna is designed to achieve -1 *dB* gain bandwidth 8.2%, efficiency of 38.35%, and peak gain of 30.92 *dB*. This performance is achieved by appropriately designing both the TA and its array feed. It is shown that by fully exploiting the potentials of soft-surface-structure, the array structure can be considerably simplified and its performance is improved in terms of bandwidth (impedance and gain), pattern shape, and side lobe level. Furthermore, it is demonstrated that a low-cost broadband six-port received with MHMIC technology can be implemented by precisely characterizing its constructing components and integrating them with wire-bond interconnecting methodology. The achieved results show that the down converter is well matched and it has at least -20 *dB* isolation between its input/output ports. Furthermore, its output ports have equal amplitude and 90 ° phase shift with respect to each other. It is also shown that by using only some diodes, a low-cost balanced power detector can be realized to address the mismatch problem. Finally, a radio link is implemented for different modulations and distances, proving the potentials of integrated high gain antenna for the next generation of cellular system.

Bibliographie

[1] T. S. Rappaport, S. Sun, R. Mayzus,Z. Hang, Y. Azar, K. Wang, G. N. Wong, J. K. Schulz, M. Samimi, and F. Gutierrez, "Millimeter Wave Mobile Communications for 5G Cellular: It Will Work!," *IEEE Access*, vol. 1, pp. 335-349, 2013.

[2] C. Dehos, J. L. Gonzalez, A. Domenico, D. Ktenas, and L. Dussopt, "Millimeter-wave Access and Backhauling: The Solution to the Exponential Data Traffic Increase in 5G Mobile Communications Systems?," *IEEE Commun. Mag.*, vol. 52, no. 9, pp. 88-95, Sept. 2014.

[3] W. Roh, J. Y. Seol, P. JeongHo, B. Lee, J. Lee, Y. Kim, J. Cho, K. Cheun, and F. Aryanfar, "Millimeter-wave Beamforming as an Enabling Technology for 5G Cellular Communications: Theoretical Feasibility and Prototype Results," *IEEE Commun. Mag.*, vol.52, no. 2, pp. 106-113, Feb. 2014.

[4] T. Potelon, M. Ettorre, L. Le Coq, T. Bateman, J. Francey, D. Lelaidier, E. Seguenot, F. Devillers, and R. Sauleau, "A Low-Profile Broadband 32-Slot Continuous Transverse Stub Array for Backhaul Applications in E-Band," *IEEE Trans. Antennas Propag.*, vol. 65, no. 12, pp. 6307-6316, Dec. 2017.

[5] E. Levine, G. Malamud, S. Shtrikman, and D. Treves, “A study of microstrip array antenna with the feed network,” *IEEE Trans. Antennas Propag.*, vol. 37, no. 4, pp. 426–434, Apr. 1989.

[6] J. L. Gomez-Tornero, F. Quesada-Pereira, and A. Alvarez-Melcon, "Analysis and Design of Periodic Leaky-wave Antennas for the Millimeter Waveband in Hybrid Waveguide-planar Technology," *IEEE Trans. Antennas Propag.*, vol. 53, no. 9, pp. 2834-2842, Sept. 2005.

[7] R. Sauleau, P. Coquet, T. Matsui, and J. Daniel, "A New Concept of Focusing Antennas Using Plane-Parallel Fabry-Perot Cavities with Nonuniform Mirrors," *IEEE Trans. Antennas Propag.*, vol. 51, no. 11, pp. 3171-3175, Nov. 2003.

[8] A. Bisognin, N. Nachabe, C. Luxey, F. Gianesello, D. Gloria, Y. Alvarez, A. Arboleya-Arboleya, N. Dolatsha, M. Sawaby, and A. Arbabian, "Ball Grid Array Module with Integrated Shaped Lens for 5G Backhaul/ Fronthaul Communications in F-Band," *IEEE Trans. Antennas Propag.*, vol. 65, no. 12, pp. 6380-6394, Dec. 2017.

[9] J. Ala-Laurinaho, J. Aurinsalo, A. Karttunen, M. Kaunisto, A. Lamminen, J. Nurmiharju, A. Räisänen, J. Säily, and P. Wainio "2-D Beam-Steerable Integrated Lens Antenna System for 5G E-Band Access and Backhaul," *IEEE Trans. Microw. Theory Techn.*, vol. 64, no. 7, pp. 2244-2255, July 2016.

[10] M. Abbasi, S. E. Gunnarsson, N. Wadefalk, R. Kozhuharov, J. Svedin, S. Cherednichenko, I. Angelov, I. Kallfass, A. Leuther, and H.Zirath, "Single-Chip 220-GHz Active Heterodyne Receiver and Transmitter MMICs With On-Chip Integrated Antenna," *IEEE Trans. Microw. Theory Techn.*, vol. 59, no. 2, pp. 466-478, Feb. 2011.

[11] M. Imbert, J. Romeu, M. Baquero-Escudero, M. T. Martinez-Ingles, J. M. Molina-Garcia-Pardo, and L. Jofre, "Assessment of LTCC-Based Dielectric Flat Lens Antennas and Switched-Beam Arrays for Future 5G Millimeter-Wave Communication Systems," *IEEE Trans. Antennas Propag.*, vol. 65, no. 12, pp. 6453-6473, Dec. 2017.

[12] D. Pozar, S. Targonski, and H. Syrigos, "Design of Millimeter Wave Microstrip Reflectarrays," IEEE Trans. Antennas Propag., vol.45, no.2, pp.287-296, Feb. 1997.

[13] C. Ryan, M. R. Chaharmir, J. Shaker, J. Bray, Y. Antar, and A. Ittipiboon, "A Wideband Transmitarray Using Dual-Resonant Double Square Rings," *IEEE Trans. Antennas Propag.*, vol.58, no.5, pp.1486-1493, May 2010.

[14] H. Nematollahi, J. J. Laurin, M. Barba, and J. A. Encinar, "Realization of Focused Beam and Shaped Beam Transmitarrays Based on Broadband Unit Cells," *IEEE Trans. Antennas Propag.*, vol. 65, no. 8, pp. 4368-4373, Aug. 2017.

[15] M. Niroo Jazi, M. R. Chaharmir, J. Shaker, and A. R. Sebak, "Broadband Transmitarray Antenna Design Using Polarization-Insensitive Frequency Selective Surfaces," *IEEE Trans. Antennas Propag.*, vol. 64, no. 1, pp. 99-108, Jan. 2016.

[16] A. Abbaspour-Tamijani, K. Sarabandi, and G. Rebeiz, "Antenna-Filter-Antenna Arrays as a Class of Bandpass Frequency-Selective Surfaces," *IEEE Trans. Microw. Theory Techn.*, vol. 52, no. 8, pp. 1781-1789, Aug. 2004.

[17] H. Kaouach, L. Dussopt, J. Lanteri, T. Koleck, and R. Sauleau,Wideband Low-Loss Linear and Circular Polarization Transmitarrays in V-Band, *IEEE Trans. Antennas Propag.*, vol. 59, no. 7, pp. 2513-2523, July 2011.

[18] C. Jouanlanne, A. Clemente, M. Huchard, J. Keignart, C. Barbier, T. Le Nadan, and L. Petit, "Wideband Linearly Polarized Transmitarray Antenna for 60 GHz Backhauling," *IEEE Trans. Antennas Propag.*, vol. 65, no. 3, pp. 1440-1445, March 2017.

[19] C. C. Cheng and A. Abbaspour-Tamijani, "Study of 2-bit Antenna–Filter–Antenna Elements for Reconfigurable Millimeter-Wave Lens Arrays," *IEEE Trans. Microw. Theory Techn.*, vol. 54, no. 12, pp. 4498-4506, Dec. 2006..

[20] J. Lin, "Chip-package codesign for high-frequency circuits and systems," *IEEE Micro.*, vol. 18, no. 4, pp. 24-32, Jul/Aug 1998.

[21] U. R. Pfeiffer, J. Grzyb, D. Liu, B. Gaucher, T. Beukema, B. A. Floyd, and S. K. Reynolds "A chip-scale packaging technology for 60-GHz wireless chipsets," *IEEE Trans. Microw. Theory Techn.*, vol. 54, no. 8, pp. 3387-3397, Aug. 2006.

[22] Y. P. Zhang and D. Liu, "Antenna-on-Chip and Antenna-in-Package Solutions to Highly Integrated Millimeter-Wave Devices for Wireless Communications," *IEEE Trans. Antennas Propag.*, vol. 57, no. 10, pp. 2830-2841, Oct. 2009.

[23] D. Liu and Y. P. Zhang, "Integration of Array Antennas in Chip Package for 60-GHz Radios," *in Proc. IEEE*, vol. 100, no. 7, pp. 2364-2371, July 2012.

[24] B. Zhang, H. Gulan, T. Zwick, Y. Li, U. Oderfält, F. Carlsson, and H. Zirath, "Integration of a 140 GHz Packaged LTCC Grid Array Antenna with an InP Detector," *IEEE Trans. Compon. Packag. Manuf. Technol.*, vol. 5, no. 8, pp. 1060-1068, Aug. 2015.

[25] M. Sun, Y. P. Zhang, K. M. Chua, L. L. Wai, D. Liu, and B. P. Gaucher, "Integration of Yagi Antenna in LTCC Package for Differential 60-GHz Radio," *IEEE Trans. Antennas Propag.*, vol. 56, no. 8, pp. 2780-2783, Aug. 2008.

[26] S. O. Tatu, E. Moldovan, K. Wu, and R. G. Bosisio, "A new direct millimeter-wave six-port receiver," *IEEE Trans. Microw. Theory Techn.*, vol. 49, no. 12, pp. 2517-2522, Dec 2001.

[27] T. Hentschel, "The six-port as a communications receiver," *IEEE Trans. Microw. Theory Techn.*, vol. 53, no. 3, pp. 1039-1047, March 2005.

[28] J. Osthet, A. Serban, M. Karlsson, S. Gong, J. Hartsen, and P. Karlsson "Six-Port Gigabit Demodulator," *IEEE Trans. Microw. Theory Techn.*, vol. 59, no. 1, pp. 125-131, Jan. 2011.

[29] W. L. Stutzman and G. L. Thiele, Antennas Theory and Design, *USA, Hoboken, New Jersey*, John Wiley and Sons, Inc., 3rd ed, pp. 101-103, 2012.

[30] M. Niroo-Jazi, T. A. Denidni, M. R. Chaharmir, and A. R. Sebak, "A hybrid isolator to reduce electromagnetic interactions between Tx/Rx antennas," *IEEE Antennas Wireless Propag. Lett.*, Vol. 13, pp. 75-78, Dec. 2014.

[31] C. Hannachi, B. Zouggari, R. Cojocaru, T. Djerafi, and S. O. Tatu, "A V-band high dynamic range planar integrated power detector: Design and characterization process," *Microw. Opt. Techn. Lett.*, vol. 59, no. 11, pp. 1098-2760, 2017.

[32] K. Haddadi and T. Lasri, "Formulation for Complete and Accurate Calibration of Six-Port Reflectometer," *IEEE Trans. Microw. Theory Techn.*, vol. 60, no. 3, pp. 574-581, March 2012.

[33] D. Hammou, M. Nedil, N. Kandil, Y. Coulibaly, E. Moldovan, and S. O. Tatu, "Microstrip to waveguide transition dedicated to wireless millimeter-wave applications," *Proc. IEEE Int. Symp. Antennas Propag.*, Chicago, IL, 2012.

Article 7

A 60 *GHz* Multi-Beam Antenna Array Design by Using MHMICs Technology

E. Erfani, E. Moldovan, and S. O. Tatu

Journal on optical technology letter (MOTL), vol. 58, no. 8, pp. 1844-1847, August 2016.

Abstract

Dans ce chapitre, on a conçu une antenne miniaturisée, à faisceaux commutés, à faible coût, à l'aide d'une matrice de Butler en ondes millimétriques et on en a fait une démonstration expérimentale. La matrice de Butler comprend des composants passifs, tels que les coupleurs, fabriqués sur un substrat céramique mince en technologie MHMIC. Quatre antennes « patch » avec connexion à ouverture couplée sont connectées à la sortie de la matrice de Butler, qui assure le retard de phase requis pour chaque élément de rayonnement. Les résultats montrent un bon accord entre les simulations et les mesures: une adaptation supérieure à -10 *dB* sur toute la bande de fréquence de 58-64 *GHz* et un diagramme de rayonnement multifaisceaux qui peut être focalisé à 45 °, 15 °, -15 °, et à -45 °.

Abstract

In this paper, a low-cost, miniaturized switched beam antenna using a millimeter wave Butler-matrix is designed and experimentally demonstrated. The Butler matrix consisting of passive components such as coupler and crossover is implemented on thin ceramic substrate through Miniaturized Hybrid Microwave Integrated Circuit (MHMIC) technology. Four aperture coupled patch antennas are connected to the output of Butler matrix which provides the required phase delay for each radiating element. Comparison of simulations and measurements shows good results: return loss better than -10 dB across the frequency band of 58-64 GHz and a multi beam radiation pattern which can be focused in 45 °, 15 °, -15 °, -45 ° directions.

7.1 Introduction

Recently, the use of unlicensed 60 GHz band has drawn attention due to increasing demand of ultra high data rate communication over 1 $Gbit/s$ for the wireless local area network (WLAN) and short range multimedia download. Different kinds of millimeter wave antennas have been proposed for such application so far [1]-[5]. These works have developed high gain antennas to overcome the propagation path loss of this frequency band and improve the system signal-to-noise ratio. Besides, employing an array antenna with beam forming property is also required to achieve the directive radiation beam in the desired spatial direction. Beam forming can be realized by using a Butler matrix network, which provides appropriate phases and amplitudes as excitations of array elements. This feeding network is usually implemented with planar technologies which cost-effectively facilitating its integration with other passive and active components especially in millimeter wave applications [6]-[9]. In addition, working with thin, light substrates that have excellent high frequency characteristics is desired where reduced featured sizes become critical. In [9], on organic liquid crystal polymer (LCP) platform has been utilized to incorporate a 60 GHz butler matrix with Yagi antenna array and GaAs low noise amplifier. In this perspective, the Miniaturized Hybrid Microwave Integrated Circuit (MHMIC) etched on thin ceramic substrate with low radiation loss has demonstrated to be a promising technology for small-scale elements [10]. In this work, circuit characterization of MHMIC passive components such as coupler and Wilkinson power divider have been comprehensively investigated.

In this paper, a two layer 60 *GHz* multi-beam antenna is developed by using a Butler matrix network fabricated with MHMIC technology. This feeding network excites microstrip aperture coupled patch antenna array. Depend on which input port is excited, this structure provides four radiation pattern directed at -45 °, -15 °, 15 °, 45 °. Furthermore, this circuit with the compact size of 9.2 $mm\times$ 15 mm is more compatible with the usual 100 μm thick MMIC active components in some way the MMIC chip can be placed in rectangular cuts on the ceramics and easy wire bonding with MMHIC components. A prototype of designed antenna was fabricated and the achieved results are presented in this paper.

7.2 Design of BUTLER Martix and Antenna

The proposed 60 *GHz* switched beam antenna consists of a Butler matrix and an aperture coupled patch antenna array is illustrated in Fig. 7.1. To have multi beam radiation pattern, the Butler matrix has been used to provide required phase delays and uniformly feed linear array. It is composed of four hybrid couplers, two crossovers, two phase shifter, and phase adjusting microstrip line. In this structure, to avoid the spurious influence of the feeding network on the antenna radiation pattern, the butler matrix and antenna array are implemented in different substrates, ceramic substrate with ϵ_r=9.9 and thickness of 5 *mill* and the RT/duroid 5880 substrate with ϵ_r=2.2 and 10 *mill* thickness, respectively.

The first step of designing butler matrix is related to the design of basic circuits, such as couplers and crossover through using Advanced Design System (ADS). To obtain the better S parameter performance, the shape of the circuits are rounded by considering the fabrication limitations. The microstrip line widths are 241 μm for the 50 Ω microstrip line, 119 μm for 50 Ω quarter wave line of coupler. The simulated performance of amplitudes and phases of scattering parameters of the hybrid coupler for exciting port of 1 is illustrated in Fig. 7.2. It can be seen that the return losses and the isolation are better than -20 *dB* in the frequency range of 58-64 *GHz*. In addition, the transmitted power is well divided between two out pot ports of 2 and 3, while the phase difference between these ports is around 90 °(89 °$\pm$1 °), especially around the central frequency allowed for V-band communication (60.5 *GHz*).

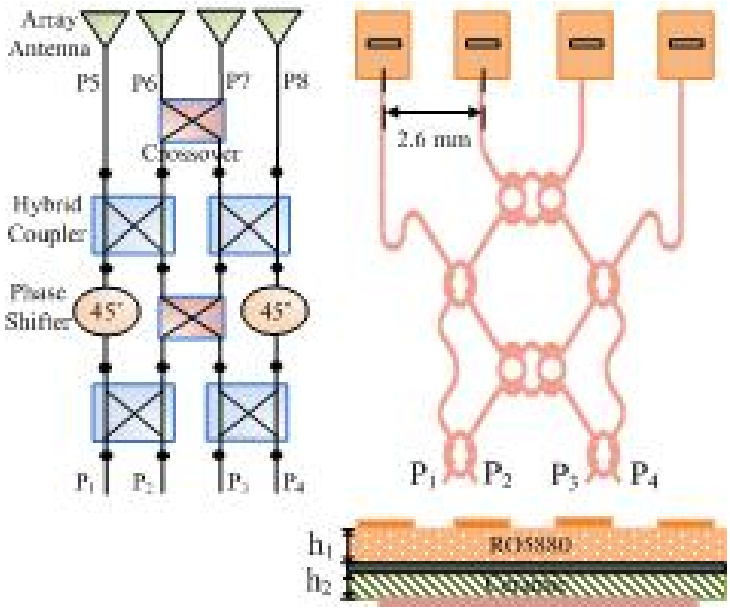

Figure 7.1 – Configuration of the developed switched-beam antenna with Butler matrix network.

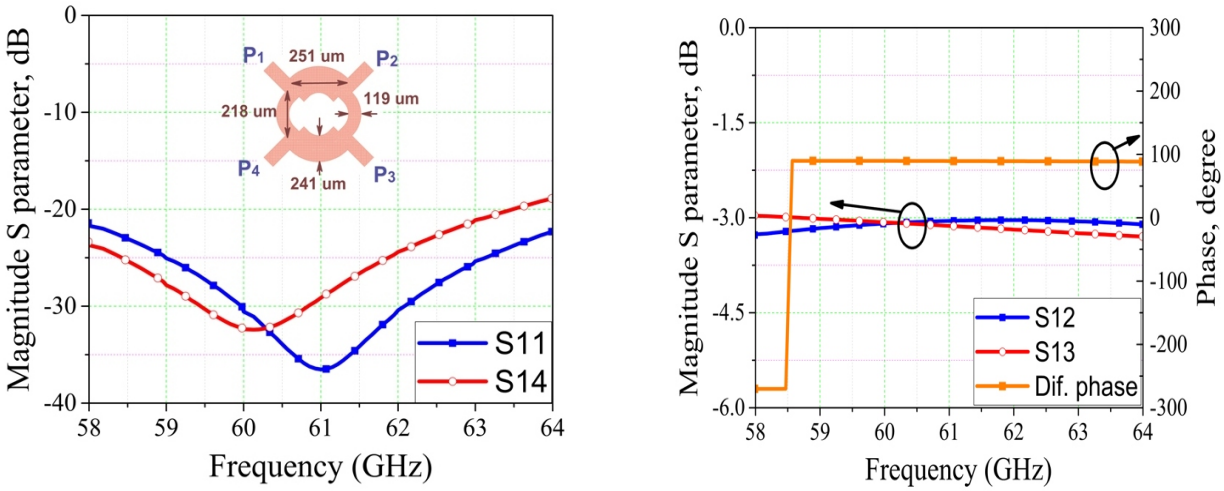

Figure 7.2 – a). simulated return loss and isolation of hybrid coupler. (b). simulated transmission S parameter magnitude / phase of hybrid coupler.

The crossover structure is realized by two serried hybrid couplers. The simulated scattering parameters of this component are shown in Fig. 7.3 demonstrating good performances in terms of isolation, return loss and insertion loss.

By integrating these circuit through two meander phase shifter of 45 °, the butler matrix can be designed. The transmission coefficient and return loss of the proposed feeding network are simulated by ADS and shown in Fig. 7.4a. From Figs. 7.4b and 7.4c, it can be found that the maximum

dispersion in the transmission magnitude is less than 1 *dB*, with an average value of 6.5 *dB* in the desired frequency range. Also as shown in Fig. 7.4d, a good phase shift was achieved at 60 *GHz* but it varies across the frequency band result in deviation on the antenna radiation pattern. This issue can be alleviated by using wide band Schiffman phase shifter. The beam forming network delivers input signals at its output ports with equal magnitudes and phases of -45 °, 135 °, -135 °, or 45 °depending on which input port is excited.

A 1.4 *mm*×1.4 *mm* patch antenna fed by aperture slot with the size of 0.8 *mm*×0.1 mm has been used as 1×4 array element. The distance between the centers of two adjacent patch antennas is 2.6 *mm* (around 0.52λ at 60 *GHz*), ensuring a good isolation and avoiding to have grating lobe in radiation pattern.

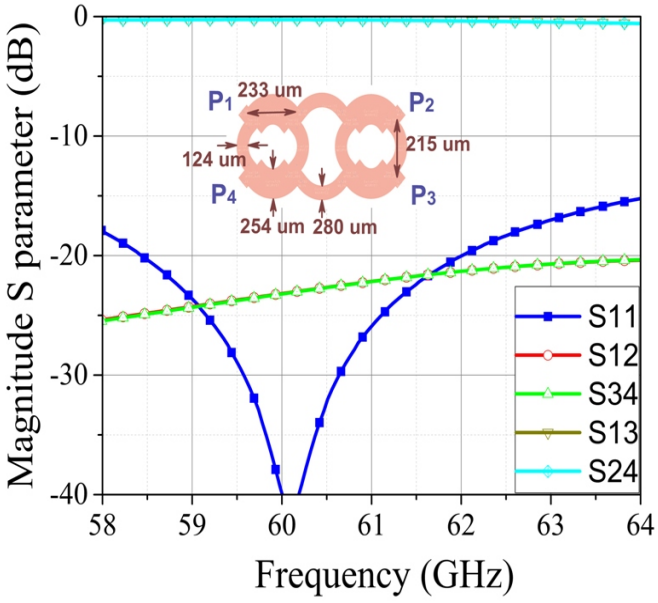

Figure 7.3 – Simulated performance of the proposed crossover.

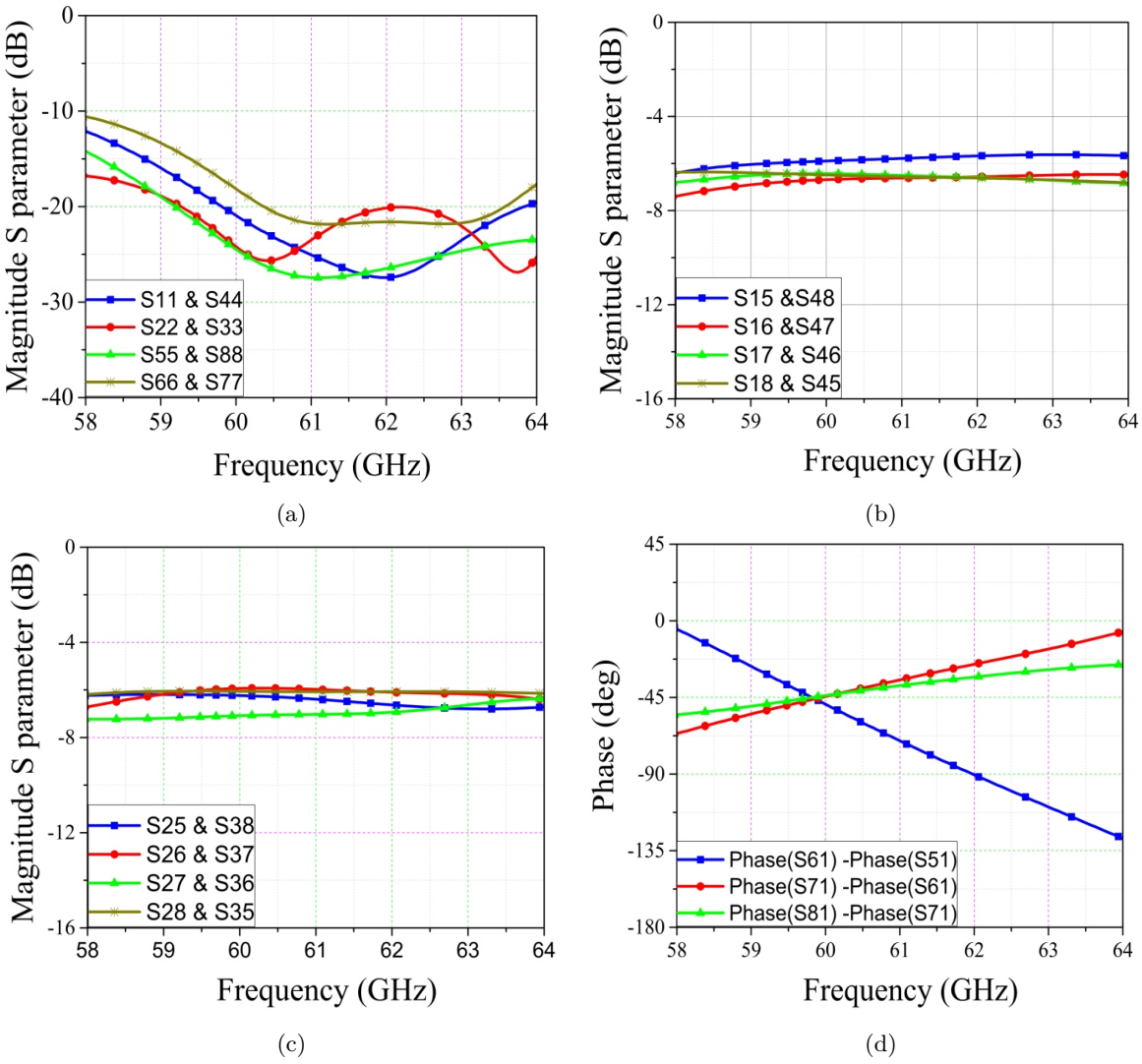

Figure 7.4 – Simulated performance of the proposed crossover.

7.3 Experimental Results

In order to validate our design, the proposed MHMICs Butler matrix is fabricated on the 15 *mill* thick ceramic substrate with the size of 2.54 cm $\times$2.54 cm size and 1 um m thick of gold as conductive layer. The array patch is mounted on the RO5880 substrate, then two layers are stacked through two prepared align holes. Because of the symmetrical nature of the Butler matrix, only two samples with different excitation port are fabricated to characterize it. Fig. 7.5 shows a photograph of the fabricated switched-beam antenna. The unused ports are matched to grounded 50Ω loads. This load is fabricated using an integrated resistor of 50Ω, fabricated on 100Ω per square titanium 20

nm thin resistor layer. Two identical resistor test kits of 50Ω were utilized to verify the titanium layer thickness on opposite points of the ceramic. Furthermore, in our designs, mm-wave RF short circuits are implemented with quarter wavelength sectors to avoid via holes. The End Launch connector with 1 *dB* loss is used to measure the performance of antenna. This connector is modeled in our simulations. The measurements of scattering parameters were carried out by Vector Network Analyser and they are compared with the simulated ones in Fig. 7.6 for exciting ports 1 and 2. The obtained results confirm a good matching performance for the frequency range of 58 to 64 *GHz*. There is a slightly difference between measured and simulated results is related to the fabrication tolerances realized in the alignment process and the effect of glue for stacking two substrate.

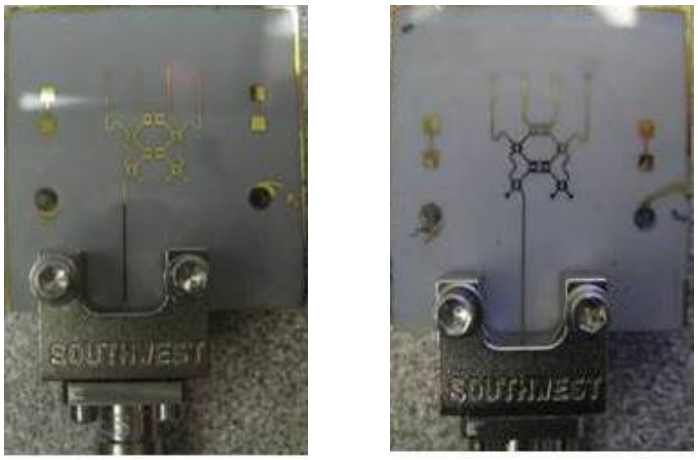

(a) (b)

Figure 7.5 – Simulated performance of the proposed crossover.

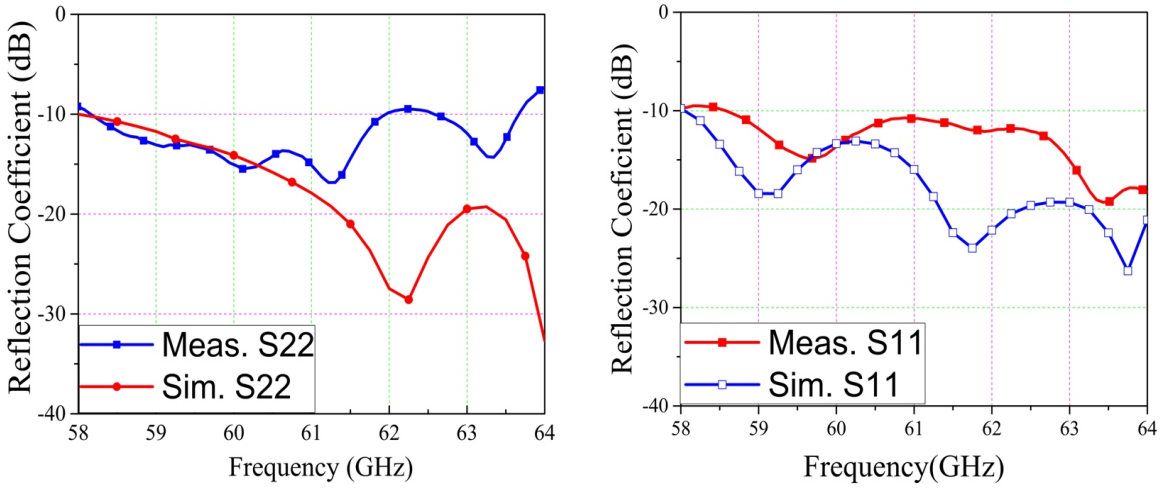

(a) (b)

Figure 7.6 – Simulated performance of the proposed crossover.

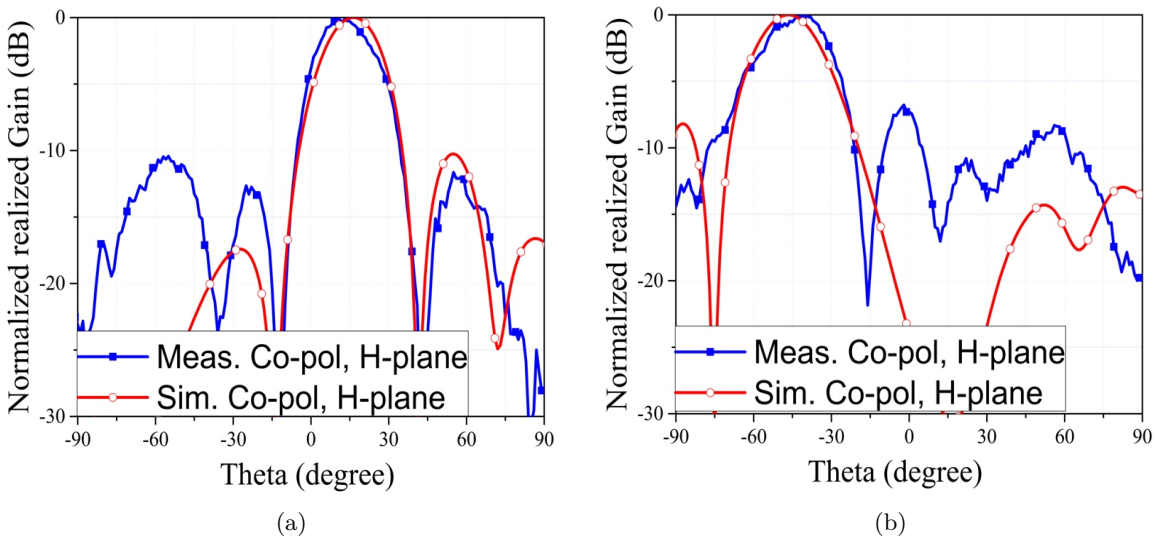

Figure 7.7 – Measured and simulated radiation pattern in XZ plane(H-plane), (a) port 1, and (b). port 2.

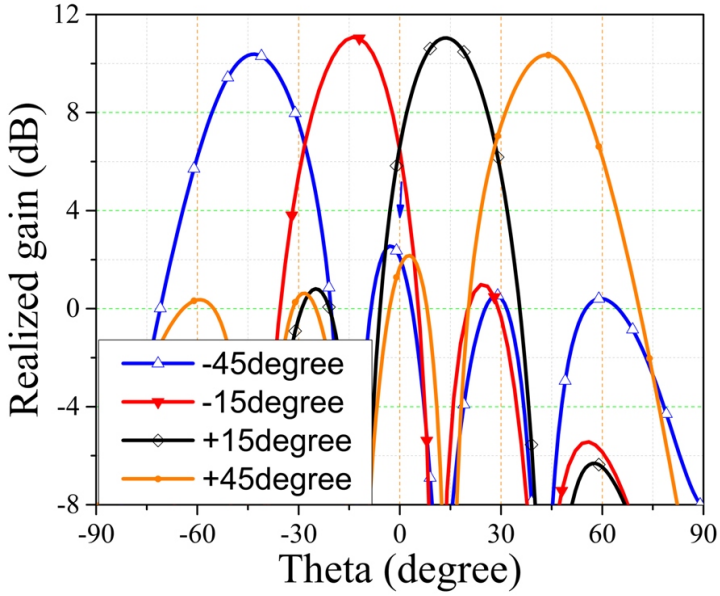

Figure 7.8 – Simulated radiation patterns in XZ plane for all excited ports.

To demonstrate the multiple beam property of the proposed structure, the antenna radiation patterns were measured for two fabricated antennas excited at port 1 and port 2. The achieved results are compared to the simulated ones as shown in Fig. 7.7 and Fig. 7.8. These figures indicate that the antenna beam is directed at θ=13° when port 1 is fed and it is at θ=-43° when port 2 is exited. In Fig. 7.7 and Fig. 7.8, a little shift noticed in the main beam may be caused by the phase error realized in the beam forming network. In addition, the measured cross polarization is less than

-15 *dB*. The simulated H-plane radiation patterns of four excited ports are depicted in Fig. 7.8. The maximum gain of 11 *dB* can be achieved for beam in direction of $theta$=15 °.

7.4 Conclusion

A 60 *GHz* multi beam antenna with MHMICs Butler- matrix is developed for millimeter wave wireless application. Required passive elements of Butler matrix such as coupler and crossover have been designed to work in wide frequency range. By integrating such a beam forming network with array of aperture coupled patch antenna, a multi beam directed at 45 °, 15 °, -15 °, -45 °can be achieved. Two structures with different excited port have been fabricated and the performances of them in terms of reflection coefficient and radiation pattern have been investigated to verify our design.

Bibliographie

[1] W. M. Abdel-Wahab, D. Busuioc, S. Safavi-Naeini, "Millimeter-Wave High Radiation Efficiency Planar Waveguide Series-Fed Dielectric Resonator Antenna (DRA) Array: Analysis, Design, and Measurements," *IEEE Trans. Antennas Propag.*, vol. 59, no. 8, pp. 2834,2843, Aug. 2011.

[2] G. R. DeJean, M. M. Tentzeris, "A New High-Gain Microstrip Yagi Array Antenna With a High (F/B) Ratio for WLAN and MM-Wave Applications," *IEEE Trans. Antennas Propag.*, vol. 55, no. 2, pp. 298-304, Feb. 2007.

[3] A. perron, T. A. Denidni, A. Sebak, "High-Gain Hybrid Dielectric Resonator Antenna for Millimeter-Wave Applications," *IEEE Trans. Antennas Propag.*, vol. 57, no. 10, pp. 2882-2892, Oct. 2009.

[4] S. W. Qu and K. B. Ng, "Wideband and Millimeter-wave Cavity-backed Bowtie," *Progress In Electromagnetics Research,* vol. 133, 477493, 2013.

[5] O. M. Haraz, "Electromagnetically-coupled Millimeter-wave Non-uniform Distribution for 60 GHz ISM Applications, " *Progress In Electromagnetics Research Lett.*, vol. 53, 71–76, 2015.

[6] B. Kilani, M. Nedil, N. Kandil, M. C. E. Yagoub, and T. A. Denidni, "Novel Wideband Multilayer Butler Matrix Using CB-CPW, " *Progress In Electromagnetics Research* , vol. 31, 116, 2012.

[7] C. Tseng, C. Chen, T. Chu, "A Low-Cost 60-GHz Switched-Beam Patch Antenna Array With Butler Matrix Network," *IEEE Antennas Wireless Propag. Lett.*, vol. 7, pp. 432-435, 2008.

[8] C. Kuo, H. Lu, P. Lin, C. Tai, Y. H. Wang, "A Fully SiP Integrated V-Band Butler Matrix End-Fire Beam-Switching Transmitter Using Flip-Chip Assembled CMOS Chips on LTCC," *IEEE Trans. Microw.* vol. 60, no. 5, pp. 1424-1436, May, 2012.

[9] [9]. C. E. Patterson, W.T. Khan, G. E. Ponchak, G. S. May, J. Papapolymerou, "A 60-GHz Active Receiving Switched-Beam Antenna Array With Integrated Butler Matrix and GaAs Amplifiers," *IEEE Trans. Microw.*, vol. 60, no. 11, pp. 3599-3607, Nov. 2012.

[10] C. Hannachi, D. Hammou, T. Djerafi, S. Tatu, "Compact Characterization of Novel MHMICs for V-band Communication Systems, " *Journal of Electrical and Computer Engineering*, Hindawi, p. 686708, 2013.

Chapitre 8

Conclusion et travaux futurs

Dans cette thèse, on a effectué des travaux de recherche pour développer une architecture d'un frontal (front-end) d'un récepteur, en utilisant des composants discrets, pour les futurs réseaux cellulaires en ondes millimétriques. Les principales contributions et les défis les plus importants sont liés à la conception du système d'antennes et à son intégration à d'autres composants RF. On a fait une démonstration du prototype fabriqué pour une liaison de communication point à point, en laboratoire. Toutefois, d'autres investigations intéressantes feront l'objet de travaux futurs, n'étant pas entièrement couvertes dans ce programme de recherche limité, comme indiqué dans les paragraphes suivants. Selon les travauxde recherche interdisciplinaires réalisés dans cette dissertation, on peut prévoir trois futurs thèmes de recherche différents.

La première porte sur la conception du système d'antennes, afin de répondre pleinement aux exigences des réseaux cellulaires en ondes millimétriques. Même si on n'a démontré ici que l'architecture de faisceaux fixes, l'utilisation d'un réseau sélectionnable d'éléments (à un commutateur multi-port) ou d'une antenne réseau à commande de phase comme alimentation pour une telle PDL, pourrait être un thème intéressant pour la réalisation d'un système d'antennes à multifaisceaux. La conception d'un réseau de commutation à faible perte et d'une antenne à large bande, ayant un large volume de balayage et de hautes performances en bande V sont les principaux défis à relever. Le deuxième travail futur suggéré porte sur d'autres architectures RF possibles, basées sur les modules réseaux à commande de phase.

Un autre sujet intéressant, qui fait l'objet d'une attention considérable ce dernier temps, pourrait être l'étude des structures extensibles (scalable) de circuit intégré, ayant la capacité de contrôler les amplitudes/phases des émetteurs-récepteurs. Il ressort des derniers travaux sur les réseaux à commande de phase à ondes millimétriques que, par le choix contrôle de plusieurs modules réseaux à commande de phase, une antenne à faisceau balayé électroniquement à un gain dans la plage de 20-30 dB est réalisable, avec au moins 256 éléments rayonnants.

Outre la conception de matériel, la propagation et la modélisation des canaux, ainsi que le développement d'un système MIMO peuvent être d'autres sujets intéressants dans le domaine des réseaux cellulaires à ondes millimétriques. Puisque les principes de propagation d'ondes radio dans le spectre des ondes millimétriques sont différents des technologies actuelles, pour une réalisation précise du budget de liaison pour la planification des sites, on a besoin de modèles appropriés pour les communications intérieures et extérieures. Ces modèles doivent se conformer aux différents schémas de modulation pour la plupart des scénarios pratiques. Lorsque la technologie MIMO émergente entrera en jeu avec un large volume de systèmes d'antennes, ce processus de planification des sites en sera un facteur-clé. Vraiment, par l'utilisation du modèle développé et des caractéristiques électriques du front-end proposé, on peut optimiser de manière analytique les liaisons, pour obtenir le meilleur rendement en termes de débit de données et pour proposer ensuite la meilleure architecture du réseau.

Journals

Elham Erfani and Serioja Tatu, "A V-Band High Gain Antenna System Integrated with a Six-Port Receiver," under review in IEEE Transaction on Antenna and Propagation, under revision Sep. 2018.

Elham Erfani, Safieddin Safavi-Naeeni, and Serioja Tatu, "Desin and Analysis of a Millimeter-Wave High Gain Antenna," Accepted in IET Microwave, Antenna, and Propagation, accepted on Nov. 2018.

Elham Erfani, and Serioja Tatu, "An Improved Performance of MM-wave Antenna Array by Using Arteficial Material," under review in IET Microwave, Antenna, and Propagation, submitted on July 2018.

Elham Erfani, Mahmoud Niroo Jazi, and Serioja Tatu, "A High Gain Broad Band Gradient Index Metamaterial Lens Antenna," in IEEE Transaction on Antenna and Propagation, vol. 64, no. 5, pp. 1968-1973, May 2016.

Elham Erfani, Emilia Moldovan, and Serioja Tatu, "A 60-GHz Multi-Beam Antenna Array Design by Using MHMICs Technology," in Microwave and Optical Technology Letter, vol. 58, n. 8, pp. 1844-47, August 2016.

Elham Erfani, Mahmoud Niroo-jazi, Tayeb Denidni, and Serioja Tatu, "A Hybrid Dielectric Resonator Antenna for Spectrum Sensing and Ultra-wide band Applications" in Microwave and Optical Technology Letter, vol. 58, n. 11, pp. 2609-11, November 2016.

Conferences

Elham Erfani, Mahmoud Niroo Jazi, Serioja Tatu, and Safieddin Safavi-Naeeni, "A Millimetre–Wave Transmitarray Antenna," in IEEE 17th International Symposium on Antenna Technology and Applied Electromagnetics (ANTEM) Montreal, QC, pp. 1-2, July 2016.

Elham Erfani, Mahmoud Niroo Jazi, Tayeb Denidni, and Serioja Tatu, "A Broadband and High Gain Millimeter-wave Hybrid Dielectric Resonator Antenna," in IEEE 17th International

Symposium on Antenna Technology and Applied Electromagnetics (ANTEM) Montreal, QC, pp. 1-2, July 2016.

Elham Erfani, Mahmoud Niroo-Jazi, Tayeb Denidni, and Serioja Tatu, "A High-Gain Lens Antenna Based on Gradient-Index Metamaterial" in IEEE Antenna and Propagation International Symposium, Vancouver, Canada, 2015.

Elham Erfani, Mahmoud Niroo-Jazi, Serioja Tatu, and Tayeb Denidni, "Harmonic Suppressed Compacted Reconfigurable Slot Antenna," in IEEE Antenna and Propagation International Symposium, Florida, USA, July 2013.

Awards

PhD-NSERC Alexander Graham Bell Scholarship

PhD-NSERC Postgraduate Scholarship

PhD-Fonds de Recherche du Quebec Nature et Technologies-FRQNT